Magnesium sensing via LFA-1 regulates CD8$^+$ T cell effector function

Jonas Lötscher[1], Adrià-Arnau Martí i Líndez[1,2,3,19], Nicole Kirchhammer[4,19], Elisabetta Cribioli[5,6,20], Greta Giordano[5,6,20], Marcel P. Trefny[4,20], Markus Lenz[7], Sacha I. Rothschild[8,9], Paolo Strati[10], Marco Künzli[11], Claudia Lotter[12], Susanne H. Schenk[12], Philippe Dehio[1], Jordan Löliger[1], Ludivine Litzler[11], David Schreiner[11], Victoria Koch[4], Nicolas Page[13], Dahye Lee[1], Jasmin Grählert[1], Dmitry Kuzmin[14,15], Anne-Valérie Burgener[1], Doron Merkler[13], Miklos Pless[9,16], Maria L. Balmer[1,17,18], Walter Reith[2], Jörg Huwyler[12], Melita Irving[5,6], Carolyn G. King[11], Alfred Zippelius[4,8], Christoph Hess[1,3,21,*]

[1] Department of Biomedicine, Immunobiology, University of Basel and University Hospital of Basel, 4031 Basel, Switzerland

[2] Department of Pathology and Immunology, Faculty of Medicine, University of Geneva, 1211 Geneva, Switzerland

[3] Department of Medicine, CITIID, Jeffrey Cheah Biomedical Centre, University of Cambridge, Cambridge CB2 0AW, United Kingdom

[4] Department of Biomedicine, Cancer Immunology, University of Basel and University Hospital of Basel, 4031 Basel, Switzerland

[5] Ludwig Institute for Cancer Research, University of Lausanne, 1066 Epalinges, Switzerland

[6] Department of Oncology, University Hospital of Lausanne, 1011 Lausanne, Switzerland

[7] University of Applied Science Northwestern Switzerland, Institute for Ecopreneurship, 4132 Muttenz, Switzerland

[8] Division of Medical Oncology and Comprehensive Cancer Center, University Hospital Basel, 4031 Basel, Switzerland

[9] Swiss Group for Clinical Cancer Research, 3008 Bern, Switzerland

[10] Department of Lymphoma and Myeloma, University of Texas MD Anderson Cancer Center, 77030 Houston, TX, USA

[11] Department of Biomedicine, Immune Cell Biology, University and University Hospital of Basel, 4031 Basel, Switzerland

[12] Department of Pharmaceutical Sciences, Pharmaceutical Technology, University of Basel, 4056 Basel, Switzerland

[13] Department of Pathology and Immunology, University of Geneva, Geneva, Switzerland

[14] Hornet Therapeutics Ltd, London SW1Y 5ES, UK

[15] Department of Medical Oncology, Yale School of Medicine, 06510 New Haven, CT, USA

[16] Department of Oncology, Cantonal Hospital Winterthur, 8400 Winterthur, Switzerland

[17] Department for Biomedical Research (DBMR), University Clinic for Diabetes, Endocrinology, Clinical Nutrition and Metabolism, Inselspital, University of Bern, 3008 Bern, Switzerland

[18] Diabetes Center Berne (DCB), 3010 Bern, Switzerland

[19] These authors contributed equally

[20] These authors contributed equally

[21] Lead contact

[*] Correspondence: chess@uhbs.ch

SUMMARY

The relevance of extracellular magnesium in cellular immunity remains largely unknown. Here, we show that the co-stimulatory cell-surface molecule LFA-1 requires magnesium to adopt its active conformation on $CD8^+$ T cells, thereby augmenting calcium flux, signal transduction, metabolic reprogramming, immune syn- apse formation, and, as a consequence, specific cytotoxicity. Accordingly, magnesium-sufficiency sensed via LFA-1 translated to the superior performance of pathogen- and tumor-specific T cells, enhanced effec- tiveness of bi-specific T cell engaging antibodies, and improved CAR T cell function. Clinically, low serum magnesium levels were associated with more rapid disease progression and shorter overall survival in CAR T cell and immune checkpoint antibody-treated patients. LFA-1 thus directly incorporates information on the composition of the microenvironment as a determinant of outside-in signaling activity. These findings conceptually link co-stimulation and nutrient sensing and point to the magnesium-LFA-1 axis as a therapeu- tically amenable biologic system.

GRAPHICAL ABSTRACT

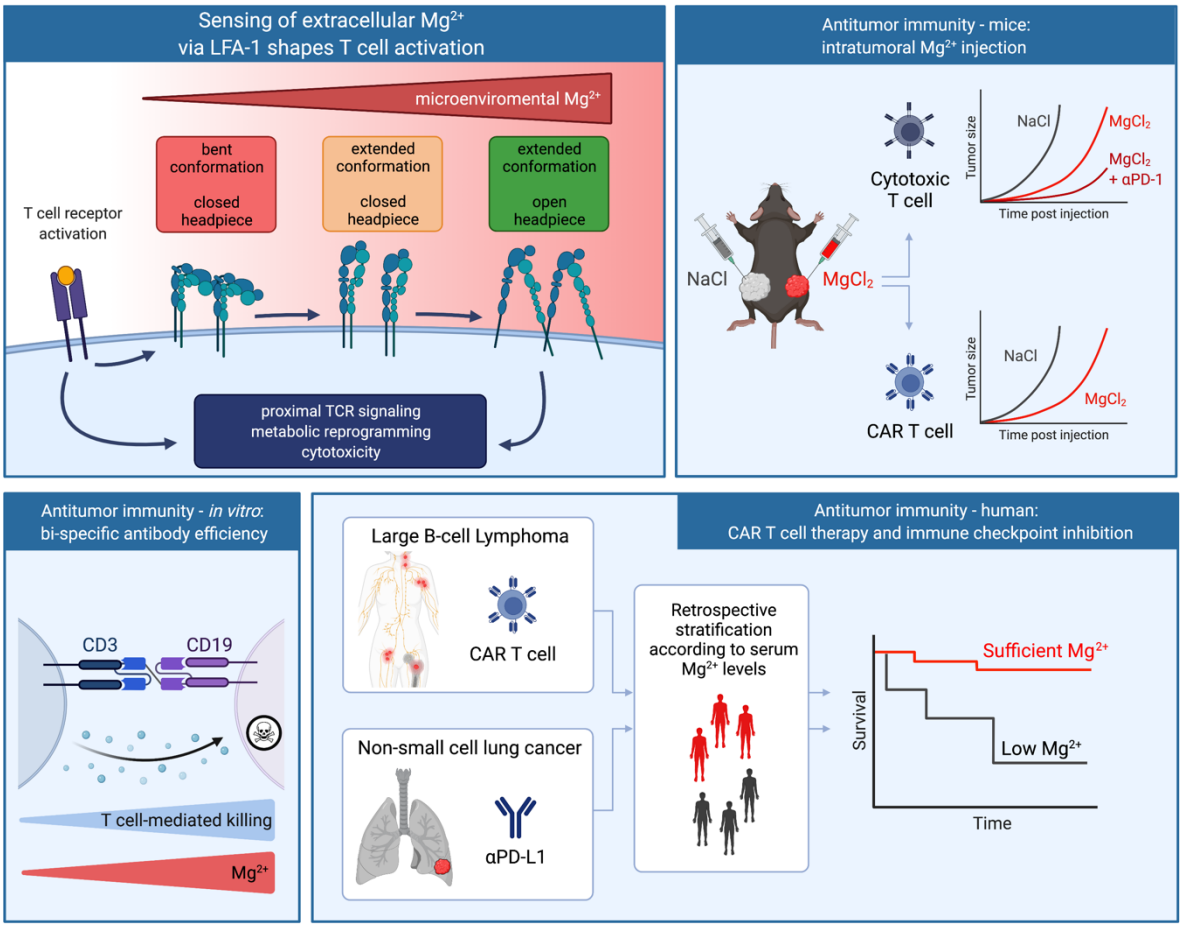

INTRODUCTION

Low dietary Mg^{2+} intake and hypomagnesemia have been implicated in the pathophysiology of various diseases, including infection and cancer (Costello and Nielsen, 2017; Larsson et al., 2012; Qu et al., 2013; Ravell et al., 2018; Sakaguchi et al., 2014; Saris et al., 2000; Schulze et al., 2007; Sojka and Weaver, 1995). Only limited experimental data are available exploring how organismal Mg^{2+} abundance may affect the immune system. It has been reported, however, that in mice fed a Mg^{2+}-deficient diet, (1) metastatic spread of carcinoma cells was accelerated (Nasulewicz et al., 2004), and (2) immune responses against influenza were impaired due to insufficient inducible T cell kinase (ITK) activity (Kanellopoulou et al., 2019). Whether in these models an effect of extracellular Mg^{2+} was contributing to shaping adaptive immune responses has not been assessed.

$CD8^+$ T cells are a key component of the adaptive immune system, playing a critical role in recognizing and eliminating infected or malignantly transformed cells. Immune surveillance of peripheral tissues by effector-memory (EM) $CD8^+$ T cells is a challenging task, requiring adaptation to constantly changing microenvironments with highly variable nutrient and oxygen content (Bantug et al., 2018; Lötscher and Balmer, 2019). Whether and, if so, how Mg^{2+} availability in tissues is sensed and integrated functionally by $CD8^+$ T cells has not been investigated.

RESULTS

First, we explored how Mg^{2+} affected memory $CD8^+$ T cell function *in vitro*, using complete media containing 1.2 mM Mg^{2+} versus no Mg^{2+} as the only difference. Analysis of metabolic flux profiles revealed that rapid induction of glycolysis of human EM $CD8^+$ T cells (defined as CD45RA and CD62L) activated by injection of soluble anti-CD3 and anti-28 monoclonal antibodies (mAb) was blunted in the absence of Mg^{2+}. This deficit was reverted when adding back Mg^{2+} just prior to activation (Figure S1A). By contrast, Mg^{2+} did not affect activation-induced upregulation of glycolysis in naive $CD8^+$ T cells (defined as $CD45RA^+$ and $CD62L^+$; Figure S1B). Next, we assessed the dose effect of Mg^{2+} in EM $CD8^+$ T cells upon stimulation with anti-CD3 and CD28 mAb, staining for markers of early and late activation (CD69 and CD25, respectively), metabolic adaptation (CD71, CD98), and degranulation (CD107a). These experiments demonstrated a strict Mg^{2+} dose response, plateauing at 0.6– 1.2 mM, that is, in the physiologic range of plasma concentrations reported for Mg^{2+} (Figure S1C) (Akizawa et al., 2008; Costello et al., 2016; Lowenstein and Stanton, 1986; Zhan et al., 2014). The difference in the capacity of memory $CD8^+$ T cells to upregulate these phenotypic markers in the presence versus absence of Mg^{2+} is summarized in Figure S1D, *left panel*. Cytokine release followed the same pattern, with decreased production under Mg^{2+}-depleted conditions in EM cells (Figure S1D, *middle panel*). EM $CD8^+$ T cell viability was not affected by the lack of Mg^{2+} in the culture media (Figure S1D, *right panel*). Analogous to induction of glycolysis, no Mg^{2+}-related effect was observed for naive $CD8^+$ T cells for each of these measures (Figure S1E, *left and middle panels*), and also, in naive cells, viability was not affected by the lack of Mg^{2+} in culture media (Figure S1E, *right panel*). The immediacy with which Mg^{2+} affected reactivity of EM $CD8^+$ T cells (Figure S1A) suggested the possibility that a Mg^{2+}-sensitive target (or targets) expressed on the cell surface could (co-)affect T cell function. Clustering of activated T cell blasts was also reduced in the absence of Mg^{2+}, lending further support to the idea that Mg^{2+} was impacting a target (or targets) on the cell surface (Figure S1F). This notion was also supported by the lack of

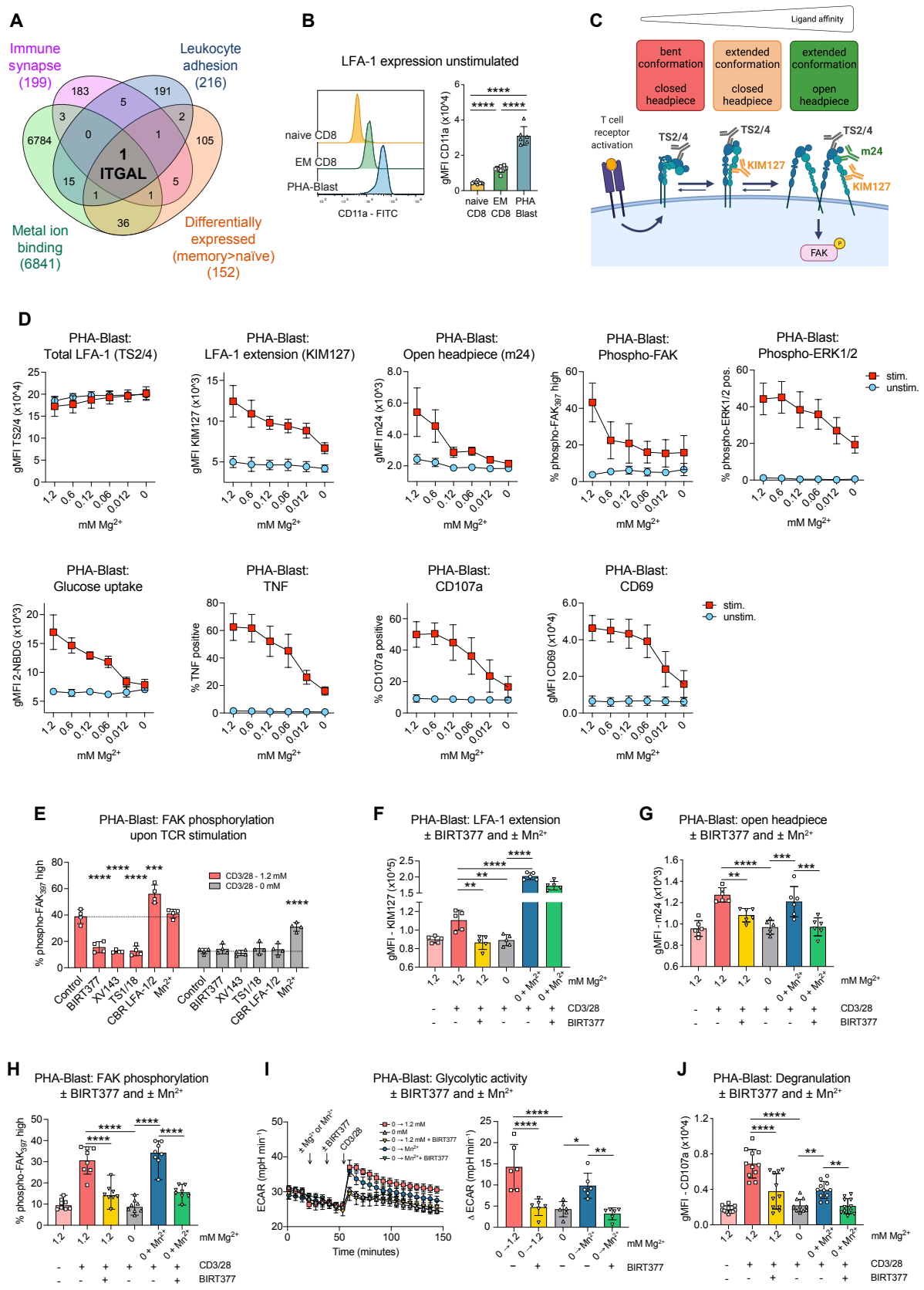
A
Immune synapse (199)
Leukocyte adhesion (216)
Metal ion binding (6841)
Differentially expressed (memory>naïve) (152)
183
191
3
5
2
6784
0
1
105
1
ITGAL
15
5
1
1
36
B
LFA-1 expression unstimulated
naive CD8
EM CD8
PHA-Blast
CD11a - FITC
gMFI CD11a (x10^4)
naive CD8
EM CD8
PHA Blast
C
Ligand affinity
bent conformation
closed headpiece
extended conformation
closed headpiece
extended conformation
open headpiece
T cell receptor activation
TS2/4
KIM127
m24
FAK
D
PHA-Blast: Total LFA-1 (TS2/4)
gMFI TS2/4 (x10^4)
PHA-Blast: LFA-1 extension (KIM127)
gMFI KIM127 (x10^3)
PHA-Blast: Open headpiece (m24)
gMFI m24 (x10^3)
PHA-Blast: Phospho-FAK
% phospho-FAK397 high
PHA-Blast: Phospho-ERK1/2
% phospho-ERK1/2 pos.
stim.
unstim.
mM Mg2+
PHA-Blast: Glucose uptake
gMFI 2-NBDG (x10^3)
PHA-Blast: TNF
% TNF positive
PHA-Blast: CD107a
% CD107a positive
PHA-Blast: CD69
gMFI CD69 (x10^4)
E
PHA-Blast: FAK phosphorylation upon TCR stimulation
% phospho-FAK397 high
CD3/28 - 1.2 mM
CD3/28 - 0 mM
Control
BIRT377
XV143
TS1/18
CBR LFA-1/2
Mn2+
F
PHA-Blast: LFA-1 extension ± BIRT377 and ± Mn2+
gMFI - KIM127 (x10^5)
mM Mg2+
CD3/28
BIRT377
G
PHA-Blast: open headpiece ± BIRT377 and ± Mn2+
gMFI - m24 (x10^3)
H
PHA-Blast: FAK phosphorylation ± BIRT377 and ± Mn2+
I
PHA-Blast: Glycolytic activity ± BIRT377 and ± Mn2+
ECAR (mpH min-1)
Time (minutes)
Δ ECAR (mpH min-1)
J
PHA-Blast: Degranulation ± BIRT377 and ± Mn2+
gMFI - CD107a (x10^4)

Figure 1

Figure 1. Sensing of extracellular magnesium through LFA-1 shapes T cell activation

(A) Venn diagram of GO-term lists and differentially expressed proteins between $CD8^+$ T cell subsets (memory > naive).

(B) Representative CD11a expression profile on human naive and EM $CD8^+$ T cells as well as human PHA blasts as determined by flow cytometry (left panel) and a summary bar graph (right panel).

(C) Schematic of LFA-1 conformational states and antibodies used to probe them.

(D) Flow cytometric analysis of human PHA blasts ± TCR stimulation at indicated Mg^{2+} concentrations, detecting LFA-1 expression independent of conformational state (TS2/4 binding: *first panel, upper row*); extended LFA-1 (KIM127 binding: *second panel, upper row*); LFA-1 open headpiece conformation (m24 binding: *third panel, upper row*); phosphorylation of FAK (*fourth panel, upper row*); phosphorylation of ERK1/2 (*fifth panel, upper row*); uptake of 2-NBDG, indicating glucose/nutrient uptake (*first panel, lower row*); TNF production (*second panel, lower row*); degranulation as indicated by upregulation of CD107a (*third panel, lower row*); and expression of the activation marker CD69 (*forth panel, lower row*). PHA blasts established from n = 5–7 healthy donors were used.

(E) FAK phosphorylation in PHA blasts after activation in medium ± Mg^{2+} using BIRT377 (a I allosteric antagonist), XVA143 (a/b I-like allosteric antagonist), TS1/18 (blocking antibody-binding b_2 chain), CBR-LFA1/2 (activating antibody-binding b_2 chain), or Mn^{2+}. The mean signal of each condition was compared with the mean control signal of 1.2 or 0 mM Mg^{2+}, respectively.

(F–J) Assessment of human PHA blasts in medium ± Mg^{2+}; ± Mn^{2+}; ± BIRT377, as indicated, with regard to activation-induced LFA-1 extension (KIM127 binding) (F); headpiece opening (m24 binding) (G); FAK phosphorylation (H); glycolytic activity—metabolic flux traces from a representative experiment (*left panel*), summary (*right panel*) (I), and degranulation (J). Each symbol represents an individual healthy donor. Data are presented as mean ± SD, except *left panel* of (I), where symbols indicate mean ± SEM. Statistical significance was assessed by one-way ANOVA with Sidak's multiple comparison test (B and E–J). *$p < 0.05$, **$p < 0.01$, ***$p < 0.001$, ****$p < 0.0001$.

evidence for rapid Mg^{2+} flux into Mg^{2+}-deprived $CD8^+$ T cells, which was in contrast to Ca^{2+} flux tested in the same setting (Figure S1G). Guided by these phenotypic and functional data, we overlaid genes from gene ontology (GO) lists in a Venn diagram, inputting the following terms: *metal ion binding* (parent term of *Mg^{2+} binding*), *immune synapse* (CD3/28 activation), and *leukocyte adhesion* (clustering experiments), together with a published list of proteins preferentially expressed by EM over naive $CD8^+$ T cells (differential impact of Mg^{2+}) (van Aalderen et al., 2017). This approach identified *ITGAL* (the gene encoding the integrin subunit alpha L chain, CD11a) as a candidate gene plausibly linked to the input criteria (Figure 1A). CD11a combines with CD18 to form the leukocyte function-associated antigen 1 (LFA-1). LFA-1 is an integrin that is involved in T cell activation via immune synapse formation as well as in leukocyte trafficking and extravasation (Hogg et al., 2011). Upon TCR stimulation, inside-out signaling mediates LFA-1 conformational changes, which regulate LFA-1 ligand-binding affinity and the molecule's capacity for outside-in signaling. Binding of Mg^{2+} to metal-ion-dependent adhesion sites (MIDAS), one each on CD18 and CD11a, impacts these conformational changes. Specifically, MIDAS binding of Mg^{2+} modulates the interchain allosteric relay (stalk extension) and external ligand affinity (headpiece conformation) (Schürpf and Springer, 2011; Zhang and Chen, 2012). The overall expression of LFA-1, which can be assessed using mAb TS2/4, was lowest on naive $CD8^+$ T cells, higher on EM $CD8^+$ T cells, and highest on T cell blasts (Figure 1B). Memory cell-selective Mg^{2+} dependency of metabolic reprogramming and activation and Mg^{2+} dependency of clustering of T cell blasts thus aligned with the selection of *ITGAL* in our GO-term integration approach. The molecular conformation of LFA-1 can be probed by staining conformational epitopes. Specifically, KIM127 recognizes extended LFA-1, whereas m24 binds LFA1 when the headpiece is in its open position (Figure 1C). These probing antibodies were used to assess how LFA-1 extension and headpiece opening related to activation (i.e., inside-out signaling) across a range of Mg^{2+} concentrations in T cell blasts. Cell-surface expression of LFA-1, irrespective of conformation (i.e., mAb TS2/4 staining), was similar in nonactivated and activated cells and independent of Mg^{2+} availability (Figure 1D, *first panel, upper row*). LFA-1 extension (KIM127 binding) was detected on activated cells only and regulated by Mg^{2+} (Figure 1D, *second panel, upper row*). LFA-1 headpiece opening (m24 binding) was likewise detected on activated cells only and also modulated by Mg^{2+} (Figure 1D, *third pane, upper row*). The effect of Mg^{2+} on LFA-1 headpiece opening was also observed in primary human $CD8^+$ T cells (Figure S1H). In a Mg^{2+}-modulated manner, T cell activation further induced proximal and distal signaling activity (focal adhesion kinase (FAK) and extracellular signal-regulated protein kinase 1/2 (ERK1/2) phosphorylation, respectively) (Giannoni et al., 2003; Schaller et al., 1994), nutrient (2-NBDG) uptake, TNF production, and expression of CD107a and CD69 (Figure 1D, *fourth and fifth panels, upper row and lower row*). We then aimed to differentiate whether extension or headpiece opening was the critical event enabling LFA-1 outside-in signaling. To that end, effects of LFA-1 inhibitors (XVA143, BIRT377, and TS1/18) and LFA-1 activators (CBR LFA-1/2 and Mn^{2+}) were tested regarding proximal LFA1 outside-in signaling (FAK phosphorylation) in activated T cell blasts, both in the presence and absence of Mg^{2+}. In the presence of Mg^{2+}, XVA143 (allosteric antagonist inhibiting the ligand-binding I domain while stabilizing extended conformation), BIRT377 (allosteric inhibitor stabilizing bent conformation), and the mAb TS1/18 (allosteric inhibitor stabilizing the closed headpiece) all suppressed activation-induced FAK phosphorylation to levels that were observed when Mg^{2+} was lacking (Figure 1E). Extending LFA-1 with the activating mAb CBR LFA-1/2 in the presence of Mg^{2+} increased FAK

phosphorylation above the level observed in the presence of Mg^{2+} alone, and yet, extension in the absence of Mg^{2+} did not increase LFA-1 outside-in signaling (Figure 1E). Mn^{2+}, which binds both MIDAS, functions as a universal activator of integrins (Dransfield et al., 1992b; San Sebastian et al., 2006; Vorup-Jensen et al., 2007), was largely compensating for the absence of Mg^{2+} in terms of FAK phosphorylation (Figure 1E). Of note, Mn^{2+} did not affect the cell-intrinsic glycolytic or mitochondrial functional capacity of T cell blasts - core metabolic activities that were also similar in presence versus absence of Mg^{2+} in the culture media (Figures S1I and S1J). From these experiments, we concluded that extension was required but not sufficient to trigger FAK phosphorylation, and that headpiece opening - which was fully dependent on Mg^{2+} (Figure 1D) - was necessary for FAK phosphorylation to occur. Birt377 stabilizes LFA-1 in its bent state by eliminating the basal interaction between CD11a and CD18 (Moore et al., 2018; Salas et al., 2004). Therefore, adding Mn^{2+}, which binds to the beta I-MIDAS with high affinity, is expected to extend LFA-1 even in the presence of Birt377 while keeping the headpiece closed - which is indeed what we observed (Figures 1F and 1G). In this scenario, the extension of LFA-1 did not drive FAK phosphorylation, corroborating the notion that headpiece opening was a requirement for FAK phosphorylation to be initiated, while extension alone was not sufficient (Figure 1H). The same applied to downstream events regulated by LFA-1, namely activation-induced glycolysis and degranulation (Figures 1I and 1J). Intercellular adhesion molecules (ICAMs) are the ligands of LFA-1, and high-affinity LFA-1-ICAM interactions promote immune synapse formation. LFA-1 can also interact with ICAMs in *cis* (Fan et al., 2016), as well in homotypic cell-cell interactions (Fan et al., 1993; Sabatos et al., 2008). To define how ICAM binding contributed to LFA-1 outside-in signaling in the presence or absence of Mg^{2+} in our *in vitro* system, we assessed the surface expression of ICAMs on T cells. On T cell blasts, expression of ICAM-3 was highest, followed by that of ICAM-1 and ICAM-2 (Figure S1K). Primary human naive $CD8^+$ T cells expressed less ICAM-3 than EM $CD8^+$ T cells; expression of ICAM-3 on EM $CD8^+$ T cells and T cell blasts was similar (Figure S1L). We then used blocking antibodies to prevent ICAMs from interacting with LFA-1, both in the presence and absence of Mg^{2+}. Blocking of ICAM-3 moderately reduced LFA-1 headpiece opening upon activation of T cell blasts (Figure S1M) and decreased the interlinked upregulation of CD69 (Figure S1N).

These experiments established Mg^{2+} as an important regulator of EM $CD8^+$ T cell function. Mg^{2+} was further identified to impact both extension and headpiece opening of LFA-1 on activated T cells, with headpiece opening being critical to outside-in signaling and downstream T cell activation.

Immune synapse formation of expanded tumor-specific T cells is regulated via the Mg^{2+}-LFA-1 axis

Next, we generated NY-ESO-1-specific T cells using a rapid expansion protocol (REP T cells) (Dudley et al., 2002; Thomas et al., 2018). LFA-1 surface expression on human NY-ESO-1specific REP T cells was as high as on T cell blasts (PHA blasts) (Figure 2A). REP T cell killing activity was augmented by Mg^{2+} across a spectrum of target peptide (9c) concentrations used for pulsing tumor target cells - most efficiently so at low 9c concentrations (Figure S2A). Also in this antigen-specific setting, Mg^{2+} was required for LFA-1 headpiece opening, and extension of LFA-1 in the absence of headpiece opening was insufficient to initiate FAK phosphorylation, degranulation, and target cell killing (Figure 2B), as well as ERK1/2 as well as c-Jun activity (Figures S2B and S2C). Engagement of ERK1/2 and c-Jun through the LFA-1-Mg^{2+} regulatory axis was confirmed by immunoblot analyses in both

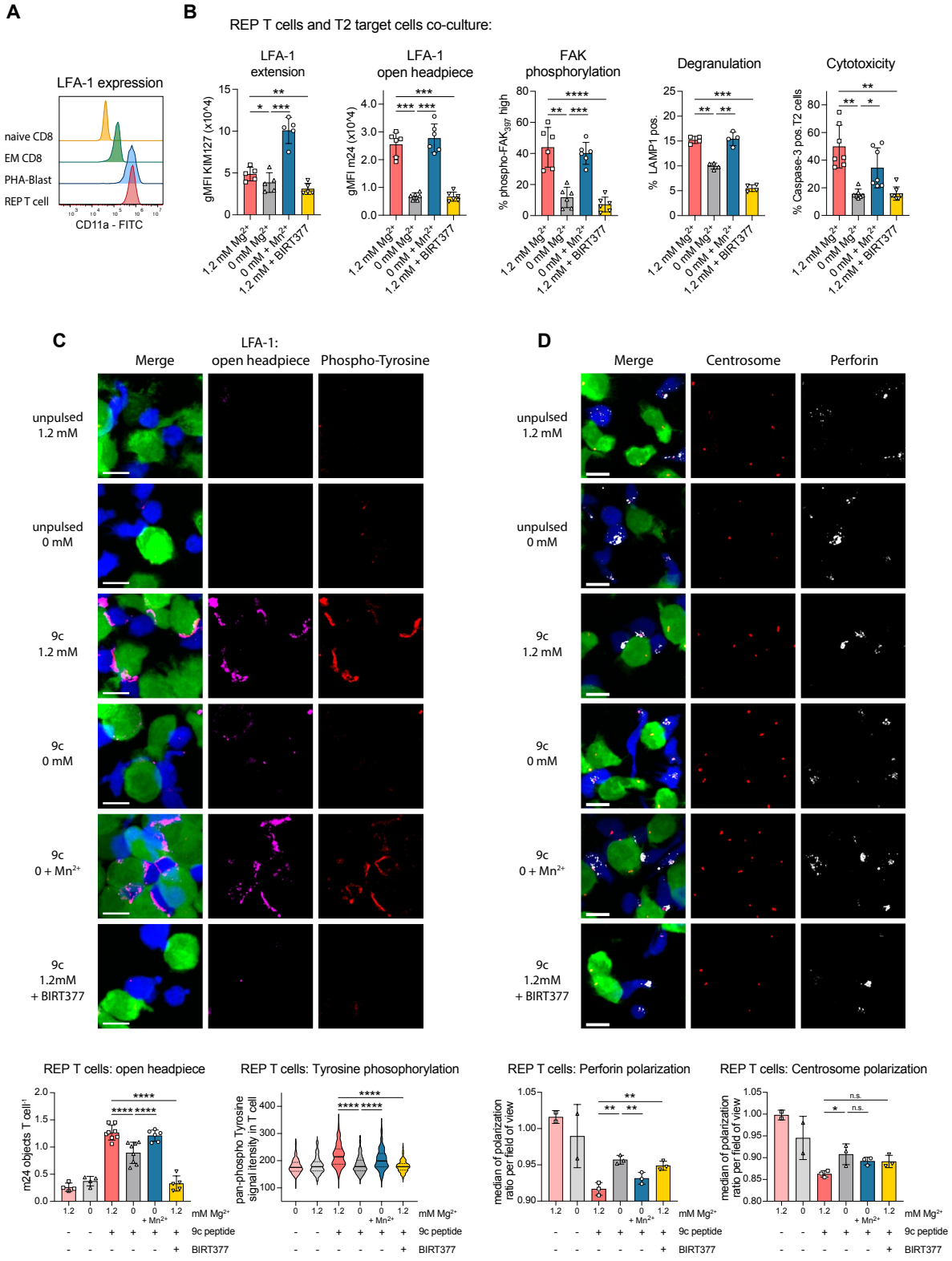
A
LFA-1 expression
naive CD8
EM CD8
PHA-Blast
REP T cell
CD11a - FITC
B
REP T cells and T2 target cells co-culture:
LFA-1 extension
gMFI KIM127 (x10^4)
LFA-1 open headpiece
gMFI m24 (x10^4)
FAK phosphorylation
% phospho-FAK397 high
Degranulation
% LAMP1 pos.
Cytotoxicity
% Caspase-3 pos.T2 cells
1.2 mM Mg2+
0 mM Mg2+
0 mM + Mn2+
1.2 mM + BIRT377
C
LFA-1:
Merge
open headpiece
Phospho-Tyrosine
unpulsed 1.2 mM
unpulsed 0 mM
9c 1.2 mM
9c 0 mM
9c 0 + Mn2+
9c 1.2mM + BIRT377
D
Merge
Centrosome
Perforin
REP T cells: open headpiece
m24 objects T cell-1
REP T cells: Tyrosine phosophorylation
pan-phospho Tyrosine signal itensity in T cell
REP T cells: Perforin polarization
median of polarization ratio per field of view
REP T cells: Centrosome polarization
mM Mg2+
+ Mn2+
9c peptide
BIRT377

Figure 2

Figure 2. The magnesium-LFA-1 axis regulates immune synapse formation of tumor-specific human T cells

(A) Representative histogram of CD11a expression on human naive and EM $CD8^+$ T cells, PHA blasts and NY-ESO-1-specific REP T cells.

(B) Flow cytometric assessment of REP T cells after incubation with T2 target cells that were pulsed with cognate peptide. REP T cells were analyzed with regard to LFA-1 extension (*first panel*), LFA-1 headpiece opening (*second panel*), FAK phosphorylation (*third panel*), and degranulation (*fourth panel*). In the *fifth panel*, co-culture-induced caspase-3 activity in T2 target cells (i.e., apoptosis) is shown. Representative of n = 2 independent experiments with n = 5–7 healthy donors; *fourth panel* n = 1 healthy donor and 4 technical replicates.

(C) *Upper panel*, representative confocal projections of REP T cells co-cultured with T2 target cells, labeled for headpiece-open LFA-1, and pan-tyrosine phosphorylation. Scale bars indicate 10 mm. *Lower left panel*, quantitation of headpiece-open LFA-1 within confocal 3D stacks (symbol represents an individual field of view). *Lower right panel*, quantitation of median fluorescence intensity of tyrosine phosphorylation in REP T cells (n = 203–344 cells per condition, pooled from n = 1–2 field of views).

(D) *Upper panel*, representative confocal projections of REP T cells co-cultured with T2 target cells. Cells were labeled for g-tubulin (centrosome) and perforin. *Lower left panel*, quantitation of perforin, *lower right panel*, quantitation of centrosome polarization (symbol represents an individual field of view). Data are presented as mean ± SD, except for the *lower right panel* of (C), where data are presented as median ± IQR. Statistical significance was assessed by repeated- measures one-way ANOVA with Sidak's multiple comparison test (B), one-way ANOVA with Sidak's multiple comparison test for the *lower left panel* of (C and D), and *lower right panel* of (D). Kruskal-Wallis test with Dunn's multiple comparison test was used for the *lower right panel* of (C). *$p < 0.05$, **$p < 0.01$, ***$p < 0.001$, ****$p < 0.0001$, n.s., nonsignificant.

human T cell blasts (Figures S2D and S2E), as well as primary human EM $CD8^+$ T cells (Figure S2F). We then visually explored immune synapse formation between NY-ESO-1-specific T cells and tumor cells. These experiments identified early antigen-specific LFA-1 headpiece opening at sites of close physical interaction between REP T cells and tumor targets, which was Mg^{2+} dependent, Mn^{2+} rescuable, and Birt377 sensitive (Figure 2C). Phospho-tyrosine signal intensity at REP T cell-target cell interaction sites also mirrored LFA-1 headpiece opening across all conditions (Figure 2C). Maturation of the immune synapse is characterized by centrosome polarization and focused delivery of cytolytic granules, two events that the Mg^{2+}-LFA-1 axis also contributed to (Figure 2D, imaging performed after 35–45 min of REP T cells target cell co-incubation).

LFA-1 is essential for Mg^{2+} to shape cytotoxic T cell activity and immune synapse formation, in vitro

To genetically probe the suggested Mg^{2+}-LFA-1 regulatory axis, experiments using LFA-1 deficient (LFA-$1^{-/-}$) cytotoxic T cells (CTLs) and LFA-$1^{-/-}$ Jurkat T cells were performed (validation of k.o.; Figure S3A). First, we repeated metabolic flux analyses using LFA-$1^{-/-}$ CTLs. These experiments confirmed LFA-1 as the mediator through which Mg^{2+} exerted its effect on glycolysis (Figure 3A). 2-NBDG (glucose/nutrient) uptake assays - which were complemented with Mn^{2+} and BIRT377 - also aligned with the metabolic flux studies (Figure S3B). TCR stimulation mediates influx of Ca^{2+} into the cytosol, where it functions as a second messenger (Trebak and Kinet, 2019). Depletion of extracellular Mg^{2+} blunted early (white bar) as well as sustained (black bar) influx of Ca^{2+} in wild-type (WT) OT-I CTLs, a finding phenocopied independently of extracellular Mg^{2+} in LFA-$1^{-/-}$ OT-I CTLs (Figure 3B). The same requirement for LFA-1 for both early and late Ca^{2+} flux was also observed in WT versus LFA-$1^{-/-}$ Jurkat cells (Figure S3C). As a proxy for early immune synapse-initiated signaling, we further analyzed TCR ligation-induced tyrosine phosphorylation, 2 min postactivation using confocal microscopy. In LFA-$1^{-/-}$ Jurkat T cells, TCR-induced tyrosine phosphorylation was markedly reduced, independently of extracellular Mg^{2+} (Figure S3D). In WT Jurkat T cells, Mg^{2+} restriction had the same effect (Figure S3D). Aligning with these genetic data, in anti-CD3 mAb activated T cell blasts, phospho-tyrosine signaling was augmented by Mg^{2+} in a BIRT377-sensitive manner, and the absence of Mg^{2+} was partially rescued by Mn^{2+} (Figure S3E). LFA-1 further recruits and amplifies TCRmediated ERK1/2 signaling at the immune synapse (Li et al., 2009) and Mg^{2+} and partially Mn^{2+} increased also ERK1/2 activity in CTLs in an LFA-1-dependent manner (Figure 3C). Of note, Mg^{2+} and Mn^{2+} *per se* did not induce p-ERK1/2 in unstimulated T cells, nor did genetic deletion or LFA-1 negatively affect pERK1/2 signaling upon supra-physiologic activation with PMA and ionomycin (Figure S3F). We then investigated the impact that the Mg^{2+}-LFA-1 system had on more downstream events in activated CTLs. CD69 and degranulation were similarly induced in activated LFA-1 competent and LFA-$1^{-/-}$ CTL cells; yet, as expected, only in LFA-1 competent cells they were modulated by Mg^{2+}, and partially also by Mn^{2+} (Figures 3D and 3E). Specific cytotoxic activity in contrast - which is a highly coordinated process requiring timed and polarized release of cytotoxic granules - was severely blunted in LFA-$1^{-/-}$ CTLs, while regulated via LFA-1 in a Mg^{2+} dependent, partially Mn^{2+} rescuable, and Birt377-sensitive manner in LFA-1 competent counterparts (Figure 3F). This suggested that both high-affinity binding of Mn^{2+} to the LFA-1 MIDAS and lack of LFA-1 were associated with dysregulated immune cell function, plausibly due to uncoordinated immune synapse formation in both scenarios. Using OVA variant peptides (affinity for OT-I: G4 < H7 < R7), the importance of the Mg^{2+}-LFA-1 system in regulating proximal LFA-1-driven

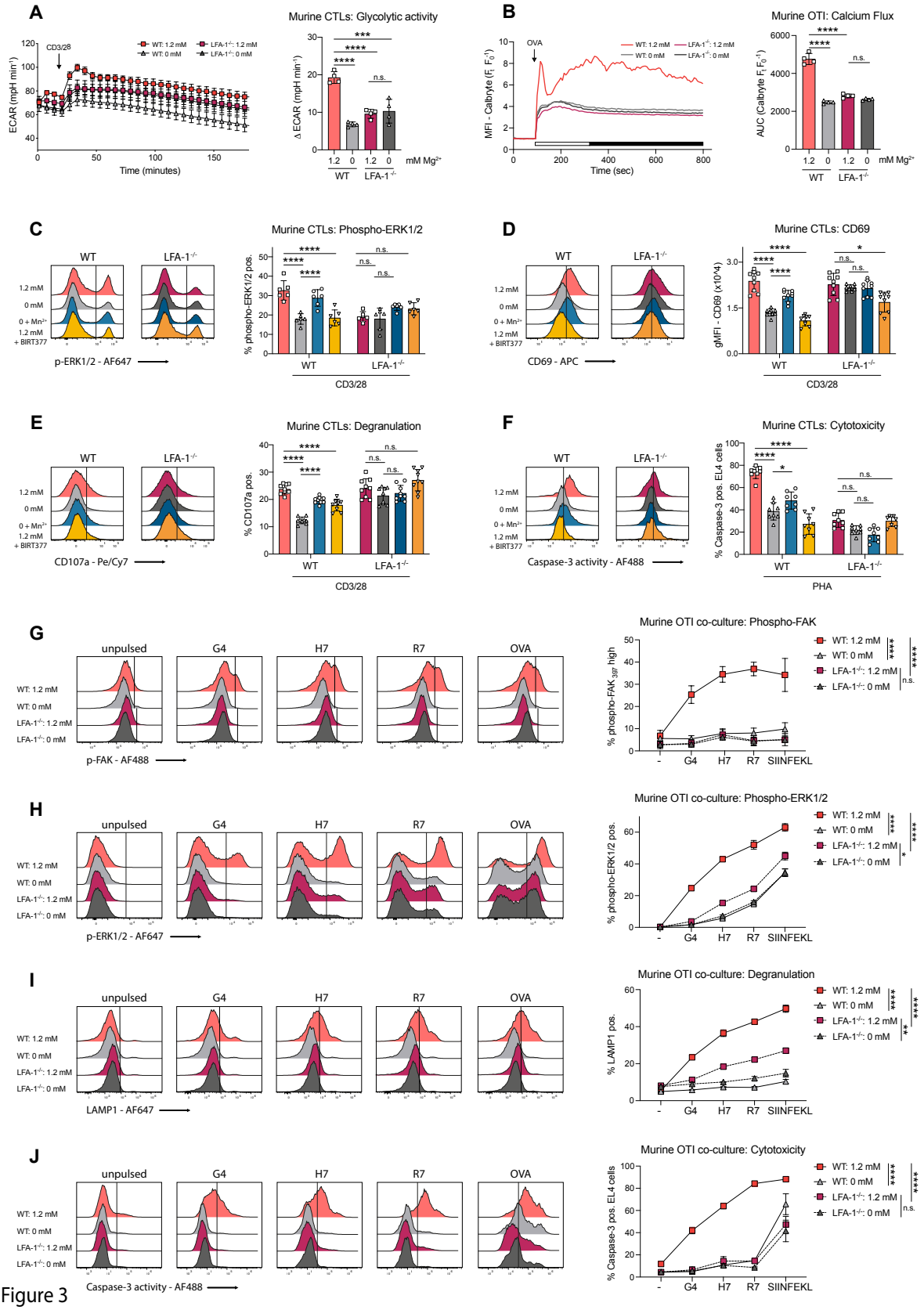
A
Murine CTLs: Glycolytic activity
ECAR (mpH min⁻¹)
Time (minutes)
CD3/28
WT: 1.2 mM
WT: 0 mM
LFA-1⁻/⁻: 1.2 mM
LFA-1⁻/⁻: 0 mM
Δ ECAR (mpH min⁻¹)
mM Mg²⁺
WT
LFA-1⁻/⁻
B
Murine OTI: Calcium Flux
OVA
MFI - Calbryte (F1 F0⁻¹)
AUC (Calbryte F1 F0⁻¹)
Time (sec)
C
Murine CTLs: Phospho-ERK1/2
p-ERK1/2 - AF647
% phospho-ERK1/2 pos.
CD3/28
D
Murine CTLs: CD69
CD69 - APC
gMFI - CD69 (x10⁻⁴)
E
Murine CTLs: Degranulation
CD107a - Pe/Cy7
% CD107a pos.
F
Murine CTLs: Cytotoxicity
Caspase-3 activity - AF488
% Caspase-3 pos. EL4 cells
PHA
G
Murine OTI co-culture: Phospho-FAK
p-FAK - AF488
% phospho-FAK 397 high
unpulsed
G4
H7
R7
OVA
SIINFEKL
H
Murine OTI co-culture: Phospho-ERK1/2
p-ERK1/2 - AF647
% phospho-ERK1/2 pos.
I
Murine OTI co-culture: Degranulation
LAMP1 - AF647
% LAMP1 pos.
J
Murine OTI co-culture: Cytotoxicity
Caspase-3 activity - AF488
% Caspase-3 pos. EL4 cells

Figure 3

Figure 3. LFA-1 is required to regulate T cell activation and cytotoxicity, in vitro

(A) Glycolytic activity upon activation of murine WT and LFA-$1^{-/-}$ CTLs. Representative experiment (*left panel*), summary of DECAR (basal versus max.) (*right panel*) from n = 4 mice.

(B) TCR stimulation induced calcium flux in WT and LFA-$1^{-/-}$ OT-I CTLs. Representative trace (*left panel*), and quantification of area under the curve (AUC) of individual wells (*right panel*). Representative of n = 3 independent experiments.

(C–E) Representative histograms (*left panels*) and quantified results from n = 3 mice with three technical replicates each (*right panels*): (C) Phosphorylation of ERK1/2; (D) surface expression of CD69, and (E) surface expression of CD107a on murine WT and LFA-$1^{-/-}$ CTLs.

(F) Caspase-3 activity in EL4 target cells after co-culture with murine WT and LFA-$1^{-/-}$ CTLs. The representative histogram shows caspase-3 activity in EL4 cells assessed by flow cytometry (*left panel*), results are quantified from n = 3 mice, with two to three technical replicates each (*right panel*).

(G–J) Representative histograms (*left panels*) and quantified results with n = 4 (technical replicates) (*right panels*). (G) Phosphorylation of FAK; (H) phosphorylation of ERK1/2; (I) surface expression of CD107a, on murine WT and LFA-$1^{-/-}$ OT-I CTLs. (J) Cytotoxicity assay using WT and LFA-$1^{-/-}$ OT-I CTLs, co-cultured with cognate antigen-pulsed EL4 target cells. Representative histogram shows caspase-3 activity in EL4 cells assessed by flow cytometry (*left panel*), the *right panel* depicts quantified results from n = 4 technical replicates. Results are representative of n = 2 independent experiments. Data are presented as mean ± SD *right panel* of (A–J). In the representative metabolic flux traces, *left panel* of (A), symbols indicate mean ± SEM. Statistical significance was assessed by one-way ANOVA with Sidak's multiple comparison test (A–F), and ordinary two-way ANOVA with main effects only and Tukey's multiple comparison test (G–J). *$p < 0.05$, **$p < 0.01$, ***$p < 0.001$, **** $p < 0.0001$, n.s., nonsignificant

signaling (FAK activity), distal LFA-1-impacted signaling (ERK1/2 activity), degranulation, and specific target cell lysis was confirmed across a spectrum of TCR affinities (Figures 3G–3J). Notably, only OVA, with its very high affinity for OT-I, triggered limited lysis independently of Mg^{2+} and LFA-1 (Figure 3J).

LFA-1 is essential for Mg^{2+} to shape T cell activation and effector function, in vivo

Our goal was then to test how genetic deletion of LFA-1 affected T cell function in relation to Mg^{2+} abundance *in vivo*. First, we established a dietary Mg^{2+} depletion model. Organismal extracellular magnesium abundance was mapped both during steady state and after 2 weeks of dietary magnesium restriction (Figure S4A). Intriguingly, in mice fed a normal diet, extracellular magnesium distribution was heterogeneous between anatomic sites - with serum, lymph nodes, and muscle being magnesium rich, while, relatively speaking, spleen, liver, and, even more pronounced so, subcutaneous fatty tissues were naturally magnesium low (Figure 4A). Mg^{2+} depletion was readily induced through dietary restriction (Figure 4A), and short-term Mg^{2+} low diet did not affect the general health status of mice (data not shown), and the body weight was comparable between cohorts (Figure S4B). Complete blood counts revealed only small changes in platelet and erythrocyte numbers (Figure S4C, *left panel*), as well as in hemoglobin levels and erythrocyte volumes (Figure S4C, *middle panel*). Differential white blood cell counts showed no alterations in Mg^{2+} depleted animals (Figure S4C, *right panel*). Further flow cytometric analyses indicated that Mg^{2+} depletion also had no relevant impact on $CD8^+$ T cell frequency, distribution of phenotypic subpopulations, and steady-state expression of the activation marker CD69 (Figures S4D–S4F). The percentage distribution of other lymphocyte subpopulations was likewise unaffected (Figure S4G). Using this model, LFA-1 WT and LFA-$1^{-/-}$ mice were then placed on normal diet versus magnesium low diet for 2 weeks and injected with anti-CD3ε F(ab0)2 fragments to polyclonally activate $CD8^+$ T cells (Figure 4B). In a strictly LFA-1-dependent manner, mice with normal organismal Mg^{2+} abundance increased expression of the activation marker CD69 on $CD8^+$ T cells. By contrast, only modest upregulation of CD69 was detected on $CD8^+$ T cells from LFA-$1^{-/-}$ mice, irrespective of diet (Figure 4C). Next, the impact of Mg^{2+} on WT and LFA-$1^{-/-}$ OT-I T cells was tested in an MC38-OVA (murine colon cancer cell line) model (Figure 4D). On day 9 after tumor implantation, that is, when tumors became palpable, WT or LFA-$1^{-/-}$ OT-I CTLs were adoptively transferred, and tumors were injected every second or third day with either 3 mM $MgCl_2$ or 3 mM NaCl (Figure 4D). Intratumoral (i.t.) Mg^{2+} application efficiently increased local Mg^{2+} abundance (Figure S4H, *left panel*). By contrast, Mg^{2+} concentrations in draining lymph nodes were variably affected and serum Mg^{2+} concentration remained unchanged (Figure S4H, *middle and right panels*). In this setting, the most efficient control of cancer growth was observed in mice transferred with WT OT-I T cells and supplemented with Mg^{2+} i.t. Tumor growth in mice transferred with LFA-$1^{-/-}$ OT-I T cells was insensitive to i.t. Mg^{2+} application and largely identical to the growth seen in mice transferred WT OT-I T cells but injected with NaCl i.t. (Figure 4E).

In vivo magnesium availability impacts infection control In order to directly monitor the effect of organismal magnesium abundance on the antigen-specific development of cytotoxic activity of memory $CD8^+$ T cells, *in vivo* killing assays were performed (Figure 5A). Antigen-specific clearance of target cells was lower in Mg^{2+}-depleted hosts, with cytotoxicity partially rescued by co-injecting magnesium together with target cells (Figure 5B). To explore the effect of magnesium on memory $CD8^+$ T cells fighting intracellular infection, a *Listeria*

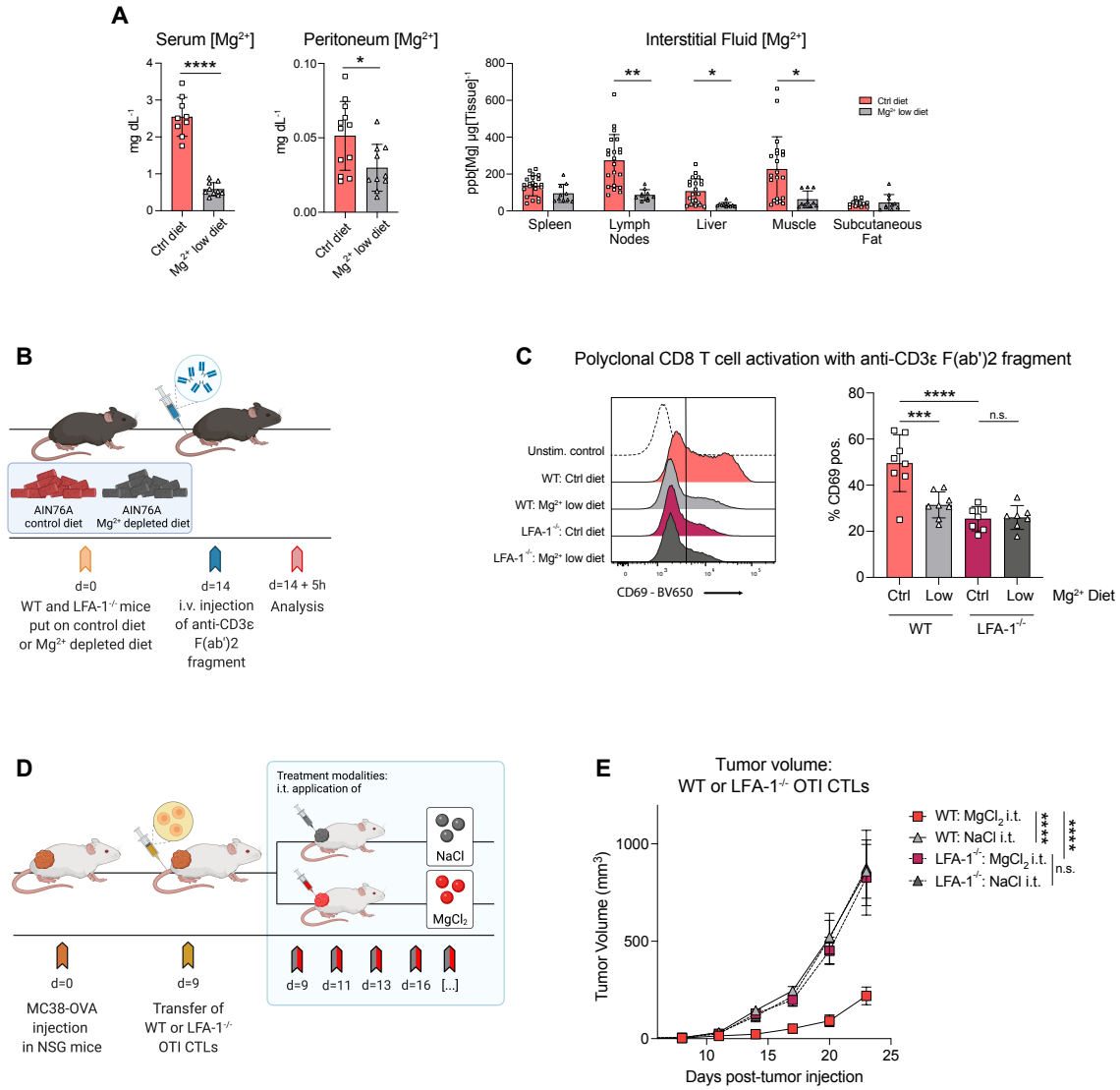
A
Serum [Mg2+]
Peritoneum [Mg2+]
Interstitial Fluid [Mg2+]
mg dL-1
ppb[Mg] µg[Tissue]-1
Ctrl diet
Mg2+ low diet
Spleen
Lymph Nodes
Liver
Muscle
Subcutaneous Fat
B
AIN76A control diet
AIN76A Mg2+ depleted diet
d=0
WT and LFA-1-/- mice put on control diet or Mg2+ depleted diet
d=14
i.v. injection of anti-CD3ε F(ab')2 fragment
d=14 + 5h
Analysis
C
Polyclonal CD8 T cell activation with anti-CD3ε F(ab')2 fragment
Unstim. control
WT: Ctrl diet
WT: Mg2+ low diet
LFA-1-/-: Ctrl diet
LFA-1-/-: Mg2+ low diet
CD69 - BV650
% CD69 pos.
n.s.
Ctrl
Low
Mg2+ Diet
WT
LFA-1-/-
D
Treatment modalities:
i.t. application of
NaCl
MgCl2
d=0
MC38-OVA injection in NSG mice
d=9
Transfer of WT or LFA-1-/- OTI CTLs
d=9
d=11
d=13
d=16
[...]
E
Tumor volume:
WT or LFA-1-/- OTI CTLs
WT: MgCl2 i.t.
WT: NaCl i.t.
LFA-1-/-: MgCl2 i.t.
LFA-1-/-: NaCl i.t.
Tumor Volume (mm3)
Days post-tumor injection

Figure 4

Figure 4. LFA-1 is required to regulate $CD8^+$ T cell activation and cytotoxicity in vivo

(A) Magnesium levels in serum (*left panel*), peritoneal lavage (*middle panel*), and interstitial fluids (*right panel*) from mice placed on Mg^{2+} reduced or matching control diet for 2 weeks. Results were pooled from two to three independent experiments, with n = 4–7 mice each. ppb, parts per billion.

(B) Schematic of experimental design.

(C) CD69 expression on $CD8^+$ T cells from the spleen of LFA-$1^{-/-}$ or WT mice. Representative flow histogram (*left panel*) and pooled data (*right panel*). Representative results from n = 2 independent experiments.

(D) Schematic of experimental design.

(E) Tumor growth curves with n = 6–7 mice per group. Each symbol represents an individual mouse (A and C), and data are presented as mean ± SD (A,C), and mean ± SEM (E). Statistical significance was assessed by unpaired two-tailed Student's t test in the *left* and *middle panel* of (A), unpaired two-tailed Student's t test with Holm-Sidak corrected multiple comparison test (A, *right panel*), one-way ANOVA with Sidak's corrected multiple comparison test (C), and two-way ANOVA with Bonferroni correction for multiple analysis (E). *p < 0.05, **p < 0.01, ***p < 0.001, ****p < 0.0001.

monocytogenes-OVA (LmOVA) intraperitoneal (i.p.) infection model was used (Figure 5C). Dietary depletion of Mg^{2+} reduced the efficiency of memory $CD8^+$ T cell effector function also in this system, with spiking the i.p. bacterial inoculum with Mg^{2+} immediately improving bacterial clearance (Figure 5D). Of note, no impact of Mg^{2+} per se on bacterial viability or growth was observed (Figure S5A). In line with these immune control data, the peritoneal abundance of Granzyme B was lower in Mg^{2+}depleted hosts and significantly rescued in mice receiving a Mg^{2+}-spiked bacterial inoculum (Figure 5E). Notably, the innate cytokine IL-6 followed an inverse pattern, with markedly increased peritoneal and serum concentrations in mice less able to control infection (Figures 5F and S5B) - plausibly reflecting increased innate inflammation due to a higher bacterial burden. Aligning with better immune control, expression of CD107a and CD69 was higher on OVA-specific $CD8^+$ T cells from Mg^{2+} competent than from Mg^{2+}-depleted mice (Figures 5G and 5H). Spiking the bacterial inoculum with Mg^{2+} rescued $CD8^+$ T cell reactivity also in this readout by trend (Figures 5G and 5H). The proportion of antigen-specific memory $CD8^+$ T cells in the peritoneal cavity was comparable between cohorts, indicating that recruitment of antigen-specific cells to the site of infection was intact in mice fed a Mg^{2+}-depleted diet (Figures S5C and S5D).

Intratumoral magnesium delivery improves memory $CD8^+$ T cell-mediated anti-tumor immunity

Adoptive transfer experiments in NSG mice demonstrated that Mg^{2+} improved cancer-directed effector activity of CTLs in an LFA-1-dependent manner (Figure 4E). In immunocompetent mice harboring OVA-specific memory $CD8^+$ T cells (i.e., immunized with OVA), injection of Mg^{2+} i.t. likewise improved local control of MC38 tumor growth. Injection of Mg^{2+} i.t. in OVA-naive mice did not affect tumor growth, and neither did contralateral i.t. injection of NaCl (Figures 6A and 6B). Of note, no clinical signs or symptoms of autoimmunity were observed in Mg^{2+} treated mice (data not shown), and anti-nuclear antibodies (ANAs) screening assays returned negative results across cohorts (Figure S6A). OVA immunization induces OVA-specific memory T cells, including memory $CD8^+$ T cells that play a key role in tumor rejection (Enamorado et al., 2017; Han et al., 2020), and depletion experiments established that Mg^{2+} exerts its effect via $CD8^+$ T cells (Figure 6C). Using flow cytometry, we then enumerated and phenotyped tumor-infiltrating immune cells. Notably, the number of tumor-infiltrating $CD8^+$ T cells was increased in the Mg^{2+}-treated group (Figure 6D), whereas the abundance of other immune cell subsets was not affected significantly (Figures S6B–S6I).

Aligning with their increased number, more Mg^{2+}-treated $CD8^+$ T cells expressed Ki67 (Figure 6E, left panel). In addition, more Mg^{2+} exposed $CD8^+$ T cells contained Granzyme B and expressed the activation marker CD25 (Figure 6E, middle and right panels). Further reflecting increased activation, PD-1 and TIM-3 were also significantly more often (co-)expressed on Mg^{2+}-treated $CD8^+$ T cells (Figure 6F). Of note, in vitro re-stimulation experiments at day 3 and day 6 post-initiation of i.t. Mg^{2+} injections did not find evidence of dysfunction (exhaustion) of $CD8^+$ T cells (data not shown). Since expression of PD-1 was higher on $CD8^+$ T cells isolated from $MgCl_2$-treated as compared with NaCl-treated tumors, we next assessed how combining $MgCl_2$ injection with PD-1 blockade was impacting tumor-directed memory $CD8^+$ T cell function (Figure 6G). Tumor control in mice receiving both intratumoral $MgCl_2$ as well as PD-1 blockade was superior compared with all other treatment regimens, with $MgCl_2$ alone again improving immune control significantly (Figure 6H). Aligning with these tumor

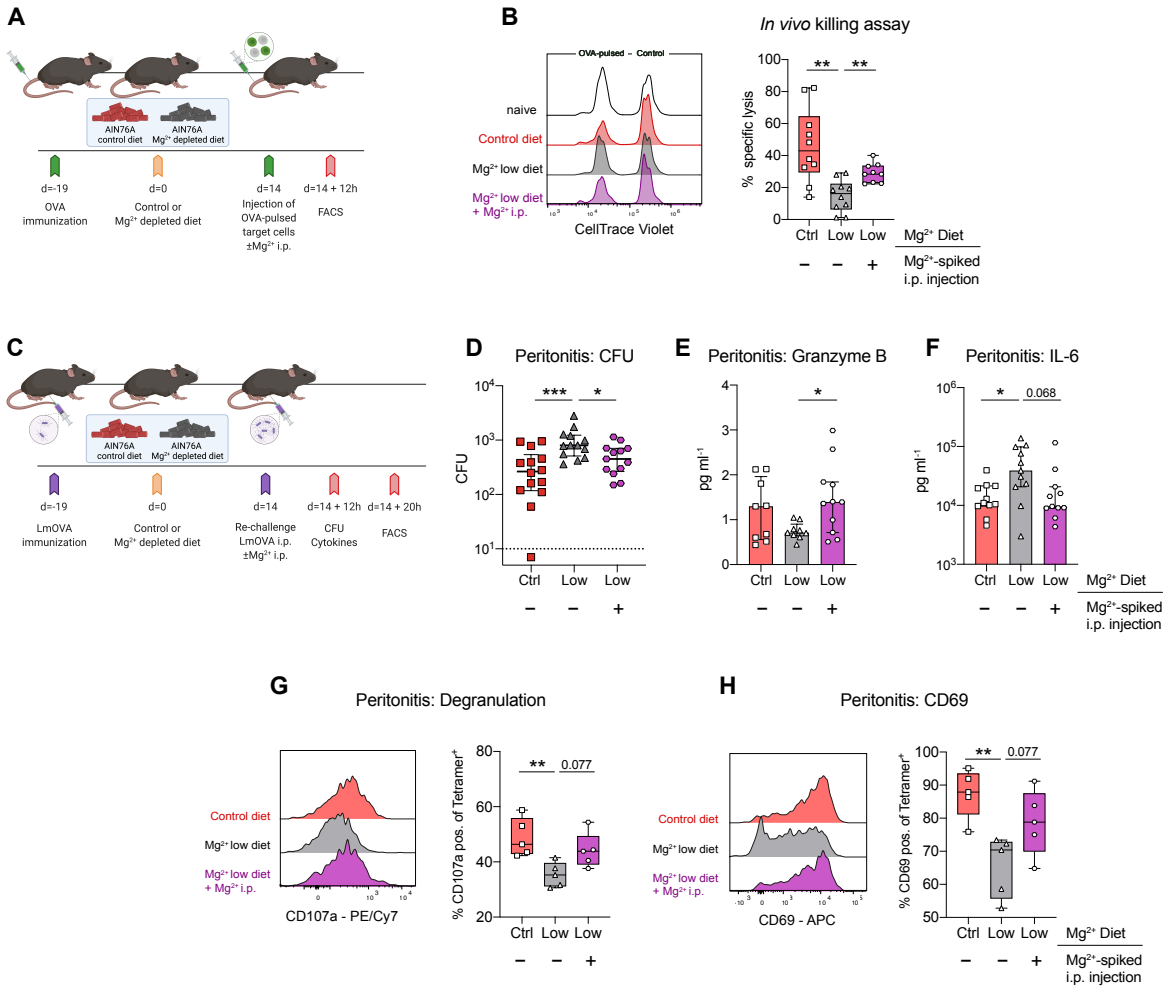
A
AIN76A control diet
AIN76A Mg2+ depleted diet
d=-19
OVA immunization
d=0
Control or Mg2+ depleted diet
d=14
Injection of OVA-pulsed target cells ±Mg2+ i.p.
d=14 + 12h
FACS
B
OVA-pulsed - Control
naive
Control diet
Mg2+ low diet
Mg2+ low diet + Mg2+ i.p.
CellTrace Violet
In vivo killing assay
% specific lysis
Ctrl Low Low
Mg2+ Diet
Mg2+-spiked i.p. injection
C
d=-19
LmOVA immunization
d=0
Control or Mg2+ depleted diet
d=14
Re-challenge LmOVA i.p. ±Mg2+ i.p.
d=14 + 12h
CFU Cytokines
d=14 + 20h
FACS
D
Peritonitis: CFU
CFU
E
Peritonitis: Granzyme B
pg ml-1
F
Peritonitis: IL-6
pg ml-1
0.068
G
Peritonitis: Degranulation
CD107a - PE/Cy7
% CD107a pos. of Tetramer+
0.077
H
Peritonitis: CD69
CD69 - APC
% CD69 pos. of Tetramer+
0.077

Figure 5

Figure 5. Organismal magnesium depletion via dietary restriction impairs memory $CD8^+$ T cell-mediated cytotoxicity

(A) Schematic of experimental design.

(B) Target cell clearance was evaluated in the spleen. Representative flow histogram (*left panel*), and summarized data from n = 2 independent experiments, with n = 4–9 mice each (*right*).

(C) Schematic of experimental design.

(D) Graph depicts bacterial burden in peritoneal lavage, data summarized from n = 3 independent experiments with n = 2–6 mice each. Abundance of Granzyme B (E) and IL-6 (F) in corresponding peritoneal fluids.

(G and H) Expression of the degranulation marker CD107a (G), and the activation marker CD69 (H) on tetramer-positive memory CD8+ T cells retrieved from the peritoneal cavity. Representative flow histogram (*left panels*), and summary data (*right panels*), from n = 5 mice each. Representative of n = 2 independent experiments. Each symbol represents an individual mouse, data are represented as median ± IQR (B and D–H) dashed line in (D) indicates detection limit. Statistical significance was assessed by unpaired two-tailed Student's t test (B), and one-way ANOVA with Sidak's corrected multiple comparison test (D–H). *p < 0.05, **p < 0.01, ***p < 0.001, ****p < 0.0001

growth data, survival of animals injected with $MgCl_2$ up to day 26 was significantly improved compared with the NaCl-injected control group, both as a sole intervention and when combined with PD-1 blockade (Figure 6I). Liposomal packaging might be a translational strategy to deliver Mg^{2+} into tumors since liposomes accumulate at sites with leaky vasculature beds (Franco et al., 2021; Nakamura et al., 2016), and i.t. application of $MgCl_2$-packed liposomes did replicate the effects induced by solute injections (Figures 6J–6L).

Encouraged by these data, we tested the effect of i.p. applied liposomes on tumor growth. Specifically, we compared NaCl-loaded versus $MgCl_2$-loaded liposomes coupled to PD1 mAb. The concentration of Mg^{2+} applied i.p. with liposomal Mg^{2+} packaging was controlled for and confirmed to be in a physiologic range (Figure S6J). I.p. administration of Mg^{2+}-loaded liposomes enhanced tumor control in a manner additive to PD-1 blockade alone (Figures 6M–6O).

Mg^{2+} has translational potential across a spectrum of emerging treatment modalities in oncology

Blinatumomab has improved the clinical outcome of select B cell malignancies (Franquiz and Short, 2020). Notably, hypomagnesemia occurs in 12%-22% of patients treated with Blinatumomab (Coyle et al., 2020; Kiyoi et al., 2020; Topp et al., 2015). Blinatumomab-mediated cytotoxicity, when used in its reported therapeutic range (230-620 pg mL1) (Topp et al., 2015), was strongly, and in a dose-dependent manner, dependent on the availability of Mg^{2+} (Figure 7A). Aligning with the cytotoxicity data, the effect of Blinatumomab on cell clustering (Figure 7B), activation-induced LFA-1 headpiece opening (Figure S7A), as well as FAK phosphorylation (Figure S7B) was likewise Mg^{2+} sensitive. Stabilizing the headpiece of LFA-1 in its closed position, using the mAb TS1/18, almost completely abrogated Blinatumomab-mediated cytotoxicity, irrespective of Mg^{2+} availability (Figure 7C). Inversely, combining Blinatumomab with the LFA-1 extending mAb CBR LFA-1/2 increased target cell killing both in the presence and absence of Mg^{2+} (Figure 7C).

To explore the relevance of Mg^{2+} in the context of CAR T cell therapy, human CD19 or prostate-specific membrane antigen (PSMA) targeting CAR T cells were used (Neelapu et al., 2017; Santoro et al., 2015). Introducing a CAR did not alter LFA-1 expression (Figure 7D) or dependency of these cells on Mg^{2+} both with respect to glycolytic reprogramming and phenotypic changes upon conventional activation via ligation of CD3 and CD28 (Figures S7C and S7D). We then went on to assess the Mg^{2+} dependency of CAR-driven cytotoxicity. In line with our previous findings with REP T cells, the Mg^{2+}-LFA-1 regulatory system reproduced in CD19 CAR T cells (Figure 7E), and timelapse killing assays demonstrated that Mg^{2+} restriction severely blunted PSMA CAR-specific killing of target cells (Figure 7F). Concomitantly, the release of IFN-g by anti-PSMA CAR T cells was reduced in Mg^{2+}-deplete conditions (Figure 7G). Tumor rejection and survival were also improved in a model where CAR T cells were adoptively transferred into mice harboring established tumors that were then Mg^{2+} enriched by i.t. injections (Figures 7H and 7I). We then wanted to test whether dietary Mg^{2+} restriction, thus reducing systemic and intratumoral Mg^{2+} abundance (Figures S7E and S7F), affects CAR T cell-mediated cytotoxicity (Figure 7J). Indeed, dietary Mg^{2+} restriction was sufficient to negatively impact CAR T cell-mediated tumor rejection (Figure 7K). Food intake was comparable between the cohorts, and yet, tumor-bearing mice fed a Mg^{2+}-depleted diet had a lower body weight by day 25 of the experiment (Figures S7G and S7H), suggestive of a more catabolic state. While the impact of (mild) intratumoral Mg^{2+} depletion through dietary restriction was

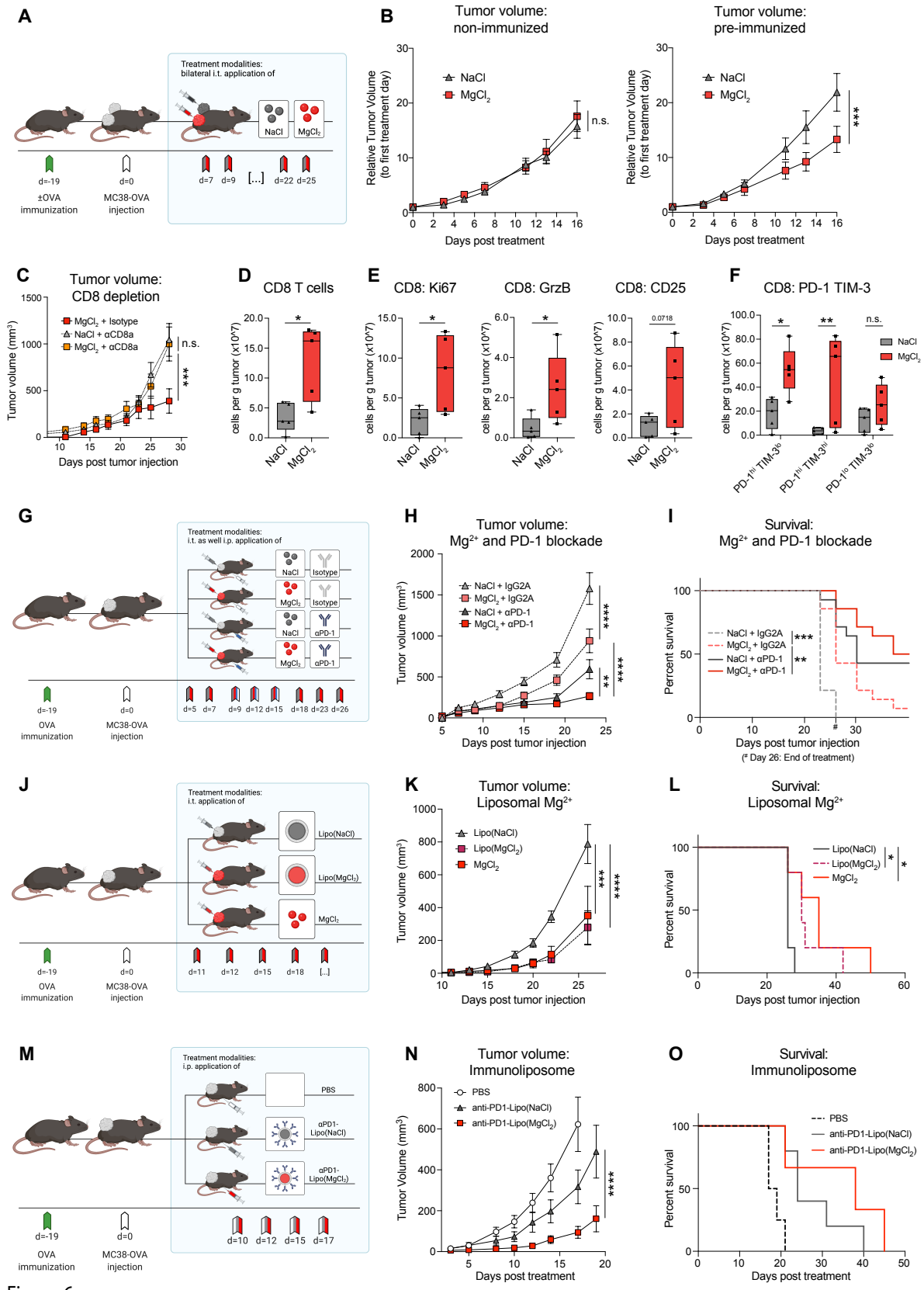
A
Treatment modalities:
bilateral i.t. application of
NaCl
MgCl2
d=-19
±OVA
immunization
d=0
MC38-OVA
injection
d=7 d=9 [...] d=22 d=25
B
Tumor volume:
non-immunized
Relative Tumor Volume
(to first treatment day)
NaCl
MgCl2
n.s.
Days post treatment
Tumor volume:
pre-immunized
***
C
Tumor volume:
CD8 depletion
Tumor volume (mm3)
MgCl2 + Isotype
NaCl + αCD8a
MgCl2 + αCD8a
n.s.
***
Days post tumor injection
D
CD8 T cells
cells per g tumor (x10^7)
E
CD8: Ki67
CD8: GrzB
CD8: CD25
0.0718
F
CD8: PD-1 TIM-3
PD-1hi TIM-3hi
PD-1hi TIM-3lo
PD-1lo TIM-3lo
G
Treatment modalities:
i.t. as well i.p. application of
Isotype
αPD-1
d=-19
OVA
immunization
d=0
MC38-OVA
injection
d=5 d=7 d=9 d=12 d=15 d=18 d=23 d=26
H
Tumor volume:
Mg2+ and PD-1 blockade
NaCl + IgG2A
MgCl2 + IgG2A
NaCl + αPD-1
MgCl2 + αPD-1
****
**
Days post tumor injection
I
Survival:
Mg2+ and PD-1 blockade
Percent survival
***
**
#
(# Day 26: End of treatment)
J
Treatment modalities:
i.t. application of
Lipo(NaCl)
Lipo(MgCl2)
MgCl2
d=11 d=12 d=15 d=18 [..]
K
Tumor volume:
Liposomal Mg2+
L
Survival:
Liposomal Mg2+
M
Treatment modalities:
i.p. application of
PBS
αPD1-
Lipo(NaCl)
αPD1-
Lipo(MgCl2)
d=10 d=12 d=15 d=17
N
Tumor volume:
Immunoliposome
anti-PD1-Lipo(NaCl)
anti-PD1-Lipo(MgCl2)
Days post treatment
O
Survival:
Immunoliposome

Figure 6

Figure 6. Intratumoral magnesium administration improves memory $CD8^+$ T cell-mediated anti-tumor immunity

(A) Schematic of experimental design.

(B) Tumor growth curves in non-immunized mice (n = 20) (*left panel*), and immunized mice (n = 19) (*right panel*). Results were pooled from two independent experiments, with n = 9–10 mice each.

(C) Tumor growth curves in ± CD8-depleted mice (n = 9–11). Results were pooled from two independent experiments, with n = 4–6 mice each. (D) Absolute numbers of tumor-infiltrating $CD8^+$ T cells.

(E) Number of tumor-infiltrating $CD8^+$ T cells positive for Ki67 (*left panel*), Granzyme B (*middle panel*), and CD25 (*right panel*).

(F) Cell number of tumor-infiltrating $CD8^+$ T cells expressing PD-1 and TIM-3.

(G) Schematic of experimental design.

(H and I) (H) Tumor growth curves (n = 13-14 mice), and (I) survival (n = 13–14 mice). Results were pooled from two independent experiments, with n = 6-7 mice each (H and I).

(J) Schematic of experimental design.

(K and L) (K) Tumor growth curves (n = 5–6 mice), and (L) survival (n = 5–6 mice).

(M) Schematic of experimental design.

(N) Tumor growth curves (n = 11–13). Results were pooled from two independent experiments.

(O) Survival. Representative of n = 2 independent experiments with n = 5–7 mice per group.

Of note, experiments (B, H, and I) and (C–F and K–O) were conducted at different animal facilities to probe for robustness.

Data are presented as mean ± SEM (B, C, and H), median ± IQR with each symbol representing one mouse (D, E, and F).

Statistical significance was assessed by two-way ANOVA with Bonferroni correction (B, C, H, K, and N), unpaired two-tailed Student's t test (D and E), two-way ANOVA with Sidak corrected multiple comparison test (F), and log-rank Mantel-Cox test (I, L, and O). *$p < 0.05$, **$p < 0.01$, ***$p < 0.001$, ****$p < 0.0001$, n.s., nonsignificant.

less pronounced than in the opposite experiment where Mg^{2+} was injected into the tumors (Figures 4E, 6B, 6C, 6H, 6K, and 7I), the effect was still clear. This prompted us to retrospectively assess the relationship between serum Mg^{2+} levels and clinical outcomes in a CAR T cell trial and in an immune checkpoint inhibitor study. The CAR trial included a cohort of 100 patients with refractory B cell lymphoma treated with CD19directed CAR T cells (Axicabtagene Ciloleucel), of which four had to be excluded from the retrospective analysis due to incomplete Mg^{2+}-serum testing (Figure S7I, *Study Diagram*). Patients were classified into two strata according to the mean Mg^{2+} level between days 5 and $^{+}$3 of treatment (n = 5 measurements available for each patient). An arbitrary cut-off was set at 1.7 mg dl^{-1} for assigning patients into normoversus hypomagnesemia groups (Figure 7L, *left panel*, and Figure S7K). Baseline characteristics of these retrospectively assigned study populations were similar, including age, ECOG performance status, and disease stage (Figure S7J). Although the number of patients with a mean Mg^{2+} level of <1.7 mg dl^{-1} was low, overall survival and median progression-free survival for these patients were reduced as compared with patients with normal serum Mg^{2+} levels (Figure 7L, *right panel*, and Figure S7L). We next explored how organismal Mg^{2+} abundance was associated with outcome in a cohort of non-small cell lung cancer (NSCLC) patients enrolled in an immune checkpoint inhibitor trial (SAKK16/14) (Rothschild et al., 2021). From a total of 67 initially enrolled patients, two had to be excluded, leaving 65 that were treated with an anti-PD-L1 mAb (Durvalumab) in addition to neoadjuvant chemotherapy (Figure S7M, *study diagram*). Any detection of hypomagnesemia during the course of the trial (n = 2-23 measurements/study participant) assigned an individual to the hypomagnesemia group. This stratification strategy well discriminated the mean Mg^{2+} levels across all available measurements (Figure 7M, *left* panel). Also in this clinical trial, baseline characteristics were similar between the two retrospectively assigned groups (Figure S7N). Pathological complete response and overall survival (Figure 7M, *middle and right panels*), as well as radiographic esponse and event-free survival (Figures S7O and S7P), were all reduced in patients with hypomagnesemia. While these retrospective analyses have many limitations, in the context of our experimental data, the findings aligned with the concept that Mg^{2+}, by increasing LFA-1 outside-in signaling activity, may contribute to the clinical efficacy of CAR T cells and endogenous cancer-directed T cells in human patients.

DISCUSSION

LFA-1 inside-out signaling, or activation, has previously been shown to modulate T cell function by modifying the molecule co-stimulation activity (i.e., outside-in signaling) (Gérard et al., 2021; Wang et al., 2009). Our experiments now demonstrate that, upon activation of LFA-1, extracellular Mg^{2+} increases LFA-1 outside-in signaling in a dose-dependent manner by contributing to extension and headpiece opening. Mg^{2+} exerts its effects on the conformation of LFA-1 both by binding to the beta I- and the alpha I-MIDAS, with the precise contribution of the respective interactions yet to be resolved (Schürpf and Springer, 2011; Sen et al., 2018; Shimaoka et al., 2003). Through this activity, extracellular Mg^{2+} defines the outcome of memory $CD8^{+}$ T cell-dependent immunity. Unsurprisingly, also in light of our data, complete pharmacological inhibition of LFA-1 causes severe immunosuppression (Goodman and Picard, 2012). However, it is interesting to note that, when using a mAb that stabilizes extended LFA-1 or when transferring T cells expressing constitutively extended LFA-1, T cell responses are severely impaired both *in vitro* and *in vivo* (Dransfield et al., 1992a; Semmrich et al., 2005).

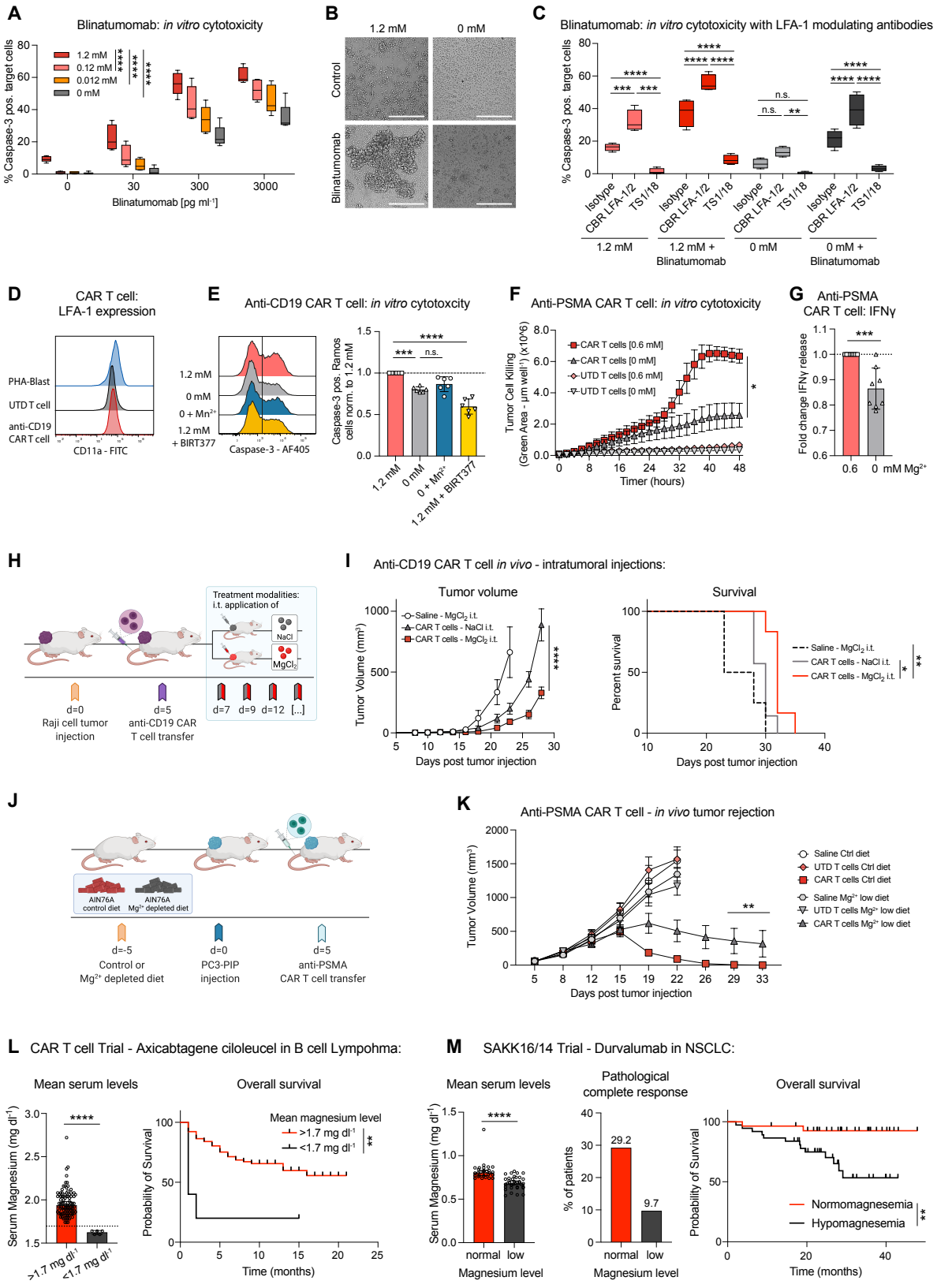
A
Blinatumomab: in vitro cytotoxicity
% Caspase-3 pos. target cells
1.2 mM
0.12 mM
0.012 mM
0 mM
Blinatumomab [pg ml-1]
B
1.2 mM
0 mM
Control
Blinatumomab
C
Blinatumomab: in vitro cytotoxicity with LFA-1 modulating antibodies
% Caspase-3 pos. target cells
Isotype
CBR LFA-1/2
TS1/18
1.2 mM
1.2 mM + Blinatumomab
0 mM
0 mM + Blinatumomab
D
CAR T cell: LFA-1 expression
PHA-Blast
UTD T cell
anti-CD19 CAR T cell
CD11a - FITC
E
Anti-CD19 CAR T cell: in vitro cytotoxcity
1.2 mM
0 mM
0 + Mn2+
1.2 mM + BIRT377
Caspase-3 - AF405
Caspase-3 pos. Ramos cells norm. to 1.2 mM
F
Anti-PSMA CAR T cell: in vitro cytotoxicity
CAR T cells [0.6 mM]
CAR T cells [0 mM]
UTD T cells [0.6 mM]
UTD T cells [0 mM]
Tumor Cell Killing (Green Area - µm well-1) (x10^6)
Timer (hours)
G
Anti-PSMA CAR T cell: IFNγ
Fold change IFNγ release
0.6
0 mM Mg2+
H
Treatment modalities: i.t. application of
NaCl
MgCl2
d=0
Raji cell tumor injection
d=5
anti-CD19 CAR T cell transfer
d=7 d=9 d=12 [...]
I
Anti-CD19 CAR T cell in vivo - intratumoral injections:
Tumor volume
Saline - MgCl2 i.t.
CAR T cells - NaCl i.t.
CAR T cells - MgCl2 i.t.
Tumor Volume (mm3)
Days post tumor injection
Survival
Percent survival
Days post tumor injection
J
AIN76A control diet
AIN76A Mg2+ depleted diet
d=-5
Control or Mg2+ depleted diet
d=0
PC3-PIP injection
d=5
anti-PSMA CAR T cell transfer
K
Anti-PSMA CAR T cell - in vivo tumor rejection
Tumor Volume (mm3)
Days post tumor injection
Saline Ctrl diet
UTD T cells Ctrl diet
CAR T cells Ctrl diet
Saline Mg2+ low diet
UTD T cells Mg2+ low diet
CAR T cells Mg2+ low diet
L
CAR T cell Trial - Axicabtagene ciloleucel in B cell Lymphoma:
Mean serum levels
Serum Magnesium (mg dl-1)
>1.7 mg dl-1
<1.7 mg dl-1
Overall survival
Mean magnesium level
>1.7 mg dl-1
<1.7 mg dl-1
Probability of Survival
Time (months)
M
SAKK16/14 Trial - Durvalumab in NSCLC:
Mean serum levels
Serum Magnesium (mg dl-1)
normal
low
Magnesium level
Pathological complete response
% of patients
29.2
9.7
normal
low
Magnesium level
Overall survival
Probability of Survival
Normomagnesemia
Hypomagnesemia
Time (months)

Figure 7

Figure 7. Extracellular magnesium impacts functionality of immunotherapeutic modalities in vitro and in vivo

(A) Box plots representing flow cytometric assessment of caspase-3 activity in Ramos target cells after co-culture with PHA blasts, n = 5 healthy donors at Mg^{2+} and Blinatumomab concentrations as indicated.

(B) Representative brightfield images of Blinatumomab-induced cell aggregation between PHA blasts and Ramos target cells in dependence of Mg^{2+}. Scale bars indicate 250 mm.

(C) Caspase-3 activity in LCL target cells after co-culture with PHA blasts ± Blinatumomab (300 pg mL^{1}), in dependence of Mg^{2+} plus CBR LFA-1/2, TS1/18, or isotype control mAb, as indicated (n = 4 healthy donors).

(D) Representative histograms of CD11a expression on PHA blasts, untransduced T cells, and anti-CD19 CAR T cells.

(E) Representative histograms (*left panel*), and results quantified from n = 2 healthy donor with three technical replicates (*right panel*) of caspase-3 activity in Ramos target cells, after co-culturing with anti-CD19 CAR T cells, ± Mg^{2+}, ± Mn^{2+}, and ± BIRT377, as indicated.

(F) Cytotoxicity assay with anti-PSMA CAR T cells and UTD T cells co-cultured with $PSMA^{+}$ PC3-PIP cell line. Pooled results using cells generated from n = 6 healthy donors and from n = 2 independent experiments are shown.

(G) Abundance of IFNg in cell culture supernatants corresponding to conditions depicted in (F) (n = 8, 3 independent experiments).

(H) Schematic of experimental design.

(I) Tumor growth curves (*left panel*) and survival (*right panel*) from n = 6–7 mice per group.

(J) Schematic of experimental design.

(K) Tumor growth curves. Representative of n = 2 independent experiments with n = 6 mice per group.

(L) Stratification of patients according to mean serum magnesium levels > 1.7 mg dl^{1} versus <1.7 mg dl^{1} between day 5 and day +3 of adoptive cell therapy, n = 5 measurements per patient (*left panel*). Each symbol represents one individual. Overall survival of patients stratified according to normal and low Mg^{2+} levels (*right panel*).

(M) Comparison of mean serum magnesium levels after stratification according to occurrence of R1 hypomagnesemia-measurement during the trial (n = 2–23 measurements per patient) (*left panel*). Complete pathological response (*middle panel*), and overall survival (*right panel*) according to this stratification. NSCLC, non-small cell lung cancer. Data are presented as median ± IQR (A and C), mean ± SD *right panel* of (E), (G), mean ± SEM (F and K) and *left panel* of (I), or median ± 95% CI *left panel* of (L and M). Statistical significance was assessed by two-way ANOVA with Dunnett corrected multiple comparison test (A), two-way ANOVA with Tukey's multiple comparison test (C), one-way ANOVA with Sidak's multiple comparison test *right panel* (E), repeated-measures two-way ANOVA with Tukey's multiple comparison test (F), unpaired Student's t test (G) and *left panel* of (L and M), two-way analysis of variance (ANOVA) with Bonferroni correction *left panel* of (I) as well (K), and log-rank Mantel-Cox test in *right panels* of (I, L, and M). *p < 0.05, **p < 0.01, ***p < 0.001, **** p < 0.0001, n.s., nonsignificant.

This underscores the complex interconnection between LFA-1's structural conformation, its outside-in signaling activity, and the function of T cells - a system tuned, as we show here, by Mg^{2+} in the extracellular space. In an intricate manner, extracellular Ca^{2+} and Mn^{2+} coordinate with Mg^{2+} in stabilizing beta integrin heterodimer complexes as well as in regulating conformational changes. Specifically, Ca^{2+} at physiologic concentrations has an inhibitory effect on integrin-ligand binding, while low Ca^{2+} abundance functions synergistically with Mg^{2+} in mediating cell adhesion (Dransfield et al., 1992b; Labadia et al., 1998; Onley et al., 2000). Ca^{2+} exerts these modulatory effects by binding to two adjacent metal coordination sites flanking the beta I MIDAS, termed Ligand-induced metal-binding site (LIMBS) and adjacent to MIDAS (ADMIDAS) (Chen et al., 2003; Mould et al., 2003). The potent integrin activator Mn^{2+}, in contrast, operates by binding MIDAS motifs and by competing with Ca^{2+} for LIMBS and ADMIDAS binding (Chen et al., 2003; Valdramidou et al., 2008). While our data demonstrate that modifying Mg^{2+} in the extracellular space is sufficient to impact T cell effector maturation *in vivo*, it will be interesting to study how Mg^{2+} integrates its function with other divalent cations across physiologic and pathologic concentrations.

The compartmentalized distribution of Mg^{2+} in healthy mice plausibly creates tissue-specific differences in the TCR signal strength required to activate memory $CD8^+$ T cells that are engaged in immune surveillance of Mg^{2+} high versus Mg^{2+} low tissues. It will be of value to explore whether compartment-specific effects on the $CD8^+$ T cell activation threshold not only affect infection control and cancer immune control but also affect the occurrence of autoimmunity.

Improving conventional cancer therapy by manipulating nutrient availability through dietary intervention is a field of growing interest (Kanarek et al., 2020). For example, experimental data suggest beneficial effects of repetitive fasting cycles in mice, the rationale being to target the high metabolic requirements of cancer cells (Lee et al., 2012). When aiming to translate such deprivation strategies to clinical medicine, they need, however, to be carefully balanced against the danger of imposing nutrient deficiencies that may negatively impact on host immunity. Indeed, only 2 weeks of dietary depletion of Mg^{2+} was sufficient to affect both tumor and infection immune control in mice, and low serum Mg^{2+} levels were associated with an unfavorable outcome both in CAR T cell and anti-PDL1 mAb-treated human cancer patients. Of note, hypomagnesemia is present in up to a fifth of Blinatumomab-treated individuals (Kiyoi et al., 2020), a quarter of CAR T cell recipients (Abramson et al., 2020; Locke et al., 2019; Siddiqi et al., 2019), and in up to 90% of patients receiving platin-based chemotherapy (Lajer and Daugaard, 1999; Liu et al., 2019; Oronsky et al., 2017). Inversely, a recent study in patients with acute myeloid leukemia showed that higher serum magnesium levels after allogeneic stem cell transplantation were associated with a decreased incidence of relapse but with a higher risk of acute graft-versus-host disease (Angenendt et al., 2021).

In conclusion, our data identify extracellular Mg^{2+} as an immune modulator, regulating T cell activation via LFA-1 MIDAS binding. LFA-1 thus senses Mg^{2+} and integrates its abundance in its co-stimulatory function. Through this axis, Mg^{2+} defines the threshold of T cell activation in a subset selective manner.

LIMITATIONS OF THE STUDY

Autochthonous tumors are more heterogeneous in architecture, immune cell landscape, perfusion, etc., than the cancer models used in this study, and our findings, therefore, cannot be generalized. We also have not analyzed the long-term consequences of enhancing LFA-1 outside-in signaling, which will require slow growth, i.e., more chronic cancer models. Furthermore, how organismal depletion of Mg^{2+} affects the efficiency of CAR T cells to attack established solid tumors remains to be defined. It is notable, however, that stratifying human cancer patients according to serum Mg^{2+} abundance was discriminating study participants with regard to relevant endpoints in both a CAR T celland an immune checkpoint trial. Yet, the retrospective nature of these analyses limits the significance of the associations detected. Therefore, as instructed by our findings, prospective controlled trials will need to clarify the clinical relevance of Mg^{2+} as an immunomodulatory agent in cancer medicine.

ACKNOWLEDGMENTS

J. Loet. was supported by SNSF grant 323530_171148 as well grants from the Freiwillige Akademische Gesellschaft Basel and Nikolaus und Bertha Burckhardt-Bu¨rgin-Stiftung; P.D. by SNSF grant 183980; M.L.B. by SNSF grant PMPDP3_171261/1, PCEFP3_194618 / 1, and a Novartis Foundation grant 17C141; A.Z. by SNSF grant 320030_188576; M.I. by SNSF grant 310030_204326; and C.H. by SNSF grants 31003A_172848, FZEB-0180487, and 310030_192677. We thank Ricardo Mancuso for helpful discussion and scientific input; Klaus Ley and Markus Sperandio for providing reagents; Veronica Richina for help with the hematology analyzer; and Priska Grünig, Tobias Öttl, and Michael Mayr for organizational help during the revision.

AUTHOR CONTRIBUTIONS

J. Lötscher designed, performed, and analyzed most experiments and wrote the manuscript; A.M.L., N.K., G.G., E.C., M.T., M.L., M.K., P.D., J. Löliger, L.L., C.L., S.H.S., N.P., D.S., V.K., D.L., J.G., and A.-V.B. performed and analyzed experiments; S.I.R., P.S., and M.P. provided clinical data; D.K., M.L.B., D.M., J.H., M.I., W.R., C.G.K., and A.Z. supervised and coordinated experiments; C.H. designed, supervised, and coordinated the study and wrote the manuscript. All authors reviewed the manuscript and approved its final version.

DECLARATION OF INTERESTS

J. Lötscher and C.H. are inventors on a patent relating to this study filed by the University of Basel (EP20/191392.8), which is being developed by a start-up company (Hornet Therapeutics Ltd - Scientific Founder: C.H.). J.G. is an employee of Hornet Therapeutics. The authors declare no other competing financial interests.

REFERENCES

Abramson, J.S., Palomba, M.L., Gordon, L.I., Lunning, M.A., Wang, M., Arnason, J., Mehta, A., Purev, E., Maloney, D.G., Andreadis, C., et al. (2020). Lisocabtagene maraleucel for patients with relapsed or refractory large B-cell lymphomas (transcend NHL 001): a multicentre seamless design study. Lancet *396*, 839–852.

Akizawa, Y., Koizumi, S., Itokawa, Y., Ojima, T., Nakamura, Y., Tamura, T., and Kusaka, Y. (2008). Daily magnesium intake and serum magnesium concentration among Japanese people. J. Epidemiol. *18*, 151–159.

Angenendt, L., Hilgefort, I., Mikesch, J.H., Schlüter, B., Berdel, W.E., Lenz, G., Stelljes, M., and Schliemann, C. (2021). Magnesium levels and outcome after allogeneic hematopoietic stem cell transplantation in acute myeloid leukemia. Ann. Hematol. *100*, 1871–1878.

Article

Bantug, G.R., Galluzzi, L., Kroemer, G., and Hess, C. (2018). The spectrum of T cell metabolism in health and disease. Nat. Rev. Immunol. *18*, 19–34.

Chen, J., Salas, A., and Springer, T.A. (2003). Bistable regulation of integrin adhesiveness by a bipolar metal ion cluster. Nat. Struct. Biol. *10*, 995–1001.

Costello, R.B., Elin, R.J., Rosanoff, A., Wallace, T.C., Guerrero-Romero, F., Hruby, A., Lutsey, P.L., Nielsen, F.H., Rodriguez-Moran, M., Song, Y., and Van Horn, L.V. (2016). Perspective: the case for an evidence-based reference interval for serum magnesium: the time has come. Adv. Nutr. *7*, 977–993.

Costello, R.B., and Nielsen, F. (2017). Interpreting magnesium status to enhance clinical care: Key indicators. Curr. Opin. Clin. Nutr. Metab. Care *20*, 504–511.

Coyle, L., Morley, N.J., Rambaldi, A., Mason, K.D., Verhoef, G., Furness, C.L., Zhang, A., Jung, A.S., Cohan, D., and Franklin, J.L. (2020). Open-label, phase 2 study of Blinatumomab as second salvage therapy in adults with relapsed/refractory aggressive B-cell non-Hodgkin lymphoma. Leuk *61*, 2103–2112, Lymphoma.

Dransfield, I., Cabañas, C., Barrett, J., and Hogg, N. (1992a). Interaction of leukocyte integrins with ligand is necessary but not sufficient for function. J. Cell Biol. *116*, 1527–1535.

Dransfield, I., Cabañas, C., Craig, A., and Hogg, N. (1992b). Divalent cation regulation of the function of the leukocyte integrin LFA-1. J. Cell Biol. *116*, 219–226.

Dudley, M.E., Wunderlich, J.R., Robbins, P.F., Yang, J.C., Hwu, P., Schwartzentruber, D.J., Topalian, S.L., Sherry, R., Restifo, N.P., Hubicki, A.M., et al. (2002). Cancer regression and autoimmunity in patients after clonal repopulation with antitumor lymphocytes. Science *298*, 850–854.

Enamorado, M., Iborra, S., Priego, E., Cueto, F.J., Quintana, J.A., Martínez-Cano, S., Mejías-Peérez, E., Esteban, M., Melero, I., Hidalgo, A., and Sancho, D. (2017). Enhanced anti-tumour immunity requires the interplay between resident and circulating memory CD8+ T cells. Nat. Commun. *8*, 16073.

Fan, S.T., Brian, A.A., Lollo, B.A., Mackman, N., Shen, N.L., and Edgington, T.S. (1993). CD11a/CD18 (LFA-1) integrin engagement enhances biosynthesis of early cytokines by activated T cells. Cell. Immunol *148*, 48–59.

Fan, Z., McArdle, S., Marki, A., Mikulski, Z., Gutierrez, E., Engelhardt, B., Deutsch, U., Ginsberg, M., Groisman, A., and Ley, K. (2016). Neutrophil recruitment limited by high-affinity bent b2 integrin binding ligand in cis. Nat. Commun. *7*, 12658.

Franco, M.S., Gomes, E.R., Roque, M.C., and Oliveira, M.C. (2021). Triggered drug release from liposomes: Exploiting the outer and inner tumor environment. Front. Oncol. *11*, 623760.

Franquiz, M.J., and Short, N.J. (2020). Blinatumomab for the treatment of adult B-cell acute lymphoblastic leukemia: toward a new era of targeted immunotherapy. Biologics *14*, 23–34.

Gérard, A., Cope, A.P., Kemper, C., Alon, R., and Köchl, R. (2021). LFA-1 in T cell priming, differentiation, and effector functions. Trends Immunol *42*, 706–722.

Giannoni, E., Chiarugi, P., Cozzi, G., Magnelli, L., Taddei, M.L., Fiaschi, T., Buricchi, F., Raugei, G., and Ramponi, G. (2003). Lymphocyte function-associated antigen-1-mediated T cell adhesion is impaired by low molecular weight phosphotyrosine phosphatase-dependent inhibition of FAK activity. J. Biol. Chem. *278*, 36763–36776.

Goodman, S.L., and Picard, M. (2012). Integrins as therapeutic targets. Trends Pharmacol. Sci. *33*, 405–412.

Han, J., Khatwani, N., Searles, T.G., Turk, M.J., and Angeles, C.V. (2020). Memory CD8+ T cell responses to cancer. Semin. Immunol. *49*, 101435.

Hebeisen, M., Oberle, S.G., Presotto, D., Speiser, D.E., Zehn, D., and Rufer, N. (2013). Molecular insights for optimizing T cell receptor specificity against cancer. Front. Immunol. *4*, 154.

Heberle, H., Meirelles, G.V., da Silva, F.R., Telles, G.P., and Minghim, R. (2015). InteractiVenn: A web-based tool for the analysis of sets through Venn diagrams. BMC Bioinformatics *16*, 169.

Hogg, N., Patzak, I., and Willenbrock, F. (2011). The insider's guide to leukocyte integrin signalling and function. Nat. Rev. Immunol. *11*, 416–426.

Huwyler, J., Yang, J., and Pardridge, W.M. (1997). Receptor mediated delivery of daunomycin using immunoliposomes: Pharmacokinetics and tissue distribution in the rat. J. Pharmacol. Exp. Ther. *282*, 1541–1546.

Kanarek, N., Petrova, B., and Sabatini, D.M. (2020). Dietary modifications for enhanced cancer therapy. Nature *579*, 507–517.

Kanellopoulou, C., George, A.B., Masutani, E., Cannons, J.L., Ravell, J.C., Yamamoto, T.N., Smelkinson, M.G., Jiang, P.D., Matsuda-Lennikov, M., Reilley, J., et al. (2019). Mg2+ regulation of kinase signaling and immune function. J. Exp. Med. *216*, 1828–1842.

Kiyoi, H., Morris, J.D., Oh, I., Maeda, Y., Minami, H., Miyamoto, T., Sakura, T., Iida, H., Tuglus, C.A., Chen, Y., et al. (2020). Phase 1b/2 study of Blinatumomab in Japanese adults with relapsed/refractory acute lymphoblastic leukemia. Cancer Sci *111*, 1314–1323.

Krutzik, P.O., and Nolan, G.P. (2003). Intracellular phospho-protein staining techniques for flow cytometry: Monitoring single cell signaling events. Cytometry A *55*, 61–70.

Labadia, M.E., Jeanfavre, D.D., Caviness, G.O., and Morelock, M.M. (1998). Molecular regulation of the interaction between leukocyte function-associated antigen-1 and soluble ICAM-1 by divalent metal cations. J. Immunol. *161*, 836–842.

Lajer, H., and Daugaard, G. (1999). Cisplatin and hypomagnesemia. Cancer Treat. Rev. *25*, 47–58.

Larsson, S.C., Orsini, N., and Wolk, A. (2012). Dietary magnesium intake and risk of stroke: A meta-analysis of prospective studies. Am. J. Clin. Nutr. *95*, 362–366.

Lee, C., Raffaghello, L., Brandhorst, S., Safdie, F.M., Bianchi, G., Martin-Montalvo, A., Pistoia, V., Wei, M., Hwang, S., Merlino, A., et al. (2012). Fasting cycles retard growth of tumors and sensitize a range of cancer cell types to chemotherapy. Sci. Transl. Med. *4*, 124ra27.

Li, D., Molldrem, J.J., and Ma, Q. (2009). LFA-1 regulates CD8+T cell activation via T cell receptor-mediated and LFA-1-mediated ERK1/2 signal pathways. J. Biol. Chem. *284*, 21001–21010.

Liu, W., Qdaisat, A., Soliman, P.T., Ramondetta, L., Lopez, G., Narayanan, S., Zhou, S., Cohen, L., Bruera, E., and Yeung, S.J. (2019). Hypomagnesemia and survival in patients with ovarian cancer who received chemotherapy with carboplatin. Oncologist *24*, e312–e317.

Locke, F.L., Ghobadi, A., Jacobson, C.A., Miklos, D.B., Lekakis, L.J., Oluwole, O.O., Lin, Y., Braunschweig, I., Hill, B.T., Timmerman, J.M., et al. (2019). Longterm safety and activity of axicabtagene ciloleucel in refractory large B-cell lymphoma (ZUMA-1): a single-arm, multicentre, phase 1-2 trial. Lancet Oncol *20*, 31–42.

Lötscher, J., and Balmer, M.L. (2019). Sensing between reactions how the metabolic microenvironment shapes immunity. Clin. Exp. Immunol. *197*, 161–169.

Lowenstein, F.W., and Stanton, M.F. (1986). Serum magnesium levels in the United States, 1971–1974. J. Am. Coll. Nutr. *5*, 399–414.

Moore, T.I., Aaron, J., Chew, T.L., and Springer, T.A. (2018). Measuring integrin conformational change on the cell surface with super-resolution microscopy. Cell Rep *22*, 1903–1912.

Mould, A.P., Barton, S.J., Askari, J.A., Craig, S.E., and Humphries, M.J. (2003). Role of ADMIDAS cation-binding site in ligand recognition by integrin alpha 5 beta 1. J. Biol. Chem. *278*, 51622–51629.

Nakamura, Y., Mochida, A., Choyke, P.L., and Kobayashi, H. (2016). Nanodrug delivery: Is the enhanced permeability and retention effect sufficient for curing cancer? Bioconjug. Chem. *27*, 2225–2238.

Nasulewicz, A., Wietrzyk, J., Wolf, F.I., Dzimira, S., Madej, J., Maier, J.A., Rayssiguier, Y., Mazur, A., and Opolski, A. (2004). Magnesium deficiency inhibits primary tumor growth but favors metastasis in mice. Biochim. Biophys. Acta *1739*, 26–32.

Neelapu, S.S., Locke, F.L., Bartlett, N.L., Lekakis, L.J., Miklos, D.B., Jacobson, C.A., Braunschweig, I., Oluwole, O.O., Siddiqi, T., Lin, Y., et al. (2017). Axicabtagene Ciloleucel CAR T-cell therapy in refractory large B-cell lymphoma. N. Engl. J. Med. *377*, 2531–2544.

Onley, D.J., Knight, C.G., Tuckwell, D.S., Barnes, M.J., and Farndale, R.W. (2000). Micromolar Ca2+ concentrations are essential for Mg2+-dependent binding of collagen by the integrin alpha 2beta 1 in human platelets. J. Biol. Chem. *275*, 24560–24564.

Oronsky, B., Caroen, S., Oronsky, A., Dobalian, V.E., Oronsky, N., Lybeck, M., Reid, T.R., and Carter, C.A. (2017). Electrolyte disorders with platinum-based chemotherapy: mechanisms, manifestations and management. Cancer Chemother. Pharmacol. *80*, 895–907.

Qu, X., Jin, F., Hao, Y., Li, H., Tang, T., Wang, H., Yan, W., and Dai, K. (2013). Magnesium and the risk of cardiovascular events: A meta-analysis of prospective cohort studies. PLoS One *8*, e57720.

Ravell, J., Otim, I., Nabalende, H., Legason, I.D., Reynolds, S.J., Ogwang, M.D., Ndugwa, C.M., Marshall, V., Whitby, D., Goedert, J.J., et al. (2018). Plasma magnesium is inversely associated with Epstein-Barr virus load in peripheral blood and Burkitt lymphoma in Uganda. Cancer Epidemiol *52*, 70–74.

Rothschild, S.I., Zippelius, A., Eboulet, E.I., Savic Prince, S., Betticher, D., Bettini, A., Früh, M., Joerger, M., Lardinois, D., Gelpke, H., et al. (2021). SAKK 16/ 14: durvalumab in addition to neoadjuvant chemotherapy in patients with stage IIIA(N2) non-small-cell lung cancer-a multicenter single-arm phase II trial. J. Clin. Oncol. *39*, 2872–2880.

Sabatos, C.A., Doh, J., Chakravarti, S., Friedman, R.S., Pandurangi, P.G., Tooley, A.J., and Krummel, M.F. (2008). A synaptic basis for paracrine interleukin-2 signaling during homotypic T cell interaction. Immunity *29*, 238–248.

Sakaguchi, Y., Fujii, N., Shoji, T., Hayashi, T., Rakugi, H., and Isaka, Y. (2014). Hypomagnesemia is a significant predictor of cardiovascular and non-cardiovascular mortality in patients undergoing hemodialysis. Kidney Int *85*, 174–181.

Salas, A., Shimaoka, M., Kogan, A.N., Harwood, C., von Andrian, U.H., and Springer, T.A. (2004). Rolling adhesion through an extended conformation of integrin alphaLbeta2 and relation to alpha I and beta I-like domain interaction. Immunity *20*, 393–406.

San Sebastian, E.S., Mercero, J.M., Stote, R.H., Dejaegere, A., Cossío, F.P., and Lopez, X. (2006). On the affinity regulation of the metal-ion-dependent adhesion sites in integrins. J. Am. Chem. Soc. *128*, 3554–3563.

Santoro, S.P., Kim, S., Motz, G.T., Alatzoglou, D., Li, C., Irving, M., Powell, D.J., Jr., and Coukos, G. (2015). T cells bearing a chimeric antigen receptor against prostate-specific membrane antigen mediate vascular disruption and result in tumor regression. Cancer Immunol. Res. *3*, 68–84.

Saris, N.E., Mervaala, E., Karppanen, H., Khawaja, J.A., and Lewenstam, A. (2000). Magnesium. An update on physiological, clinical and analytical aspects. Clin. Chim. Acta *294*, 1–26.

Schaller, M.D., Hildebrand, J.D., Shannon, J.D., Fox, J.W., Vines, R.R., and Parsons, J.T. (1994). Autophosphorylation of the focal adhesion kinase, pp125FAK, directs SH2-dependent binding of pp60src. Mol. Cell. Biol. *14*, 1680–1688.

Schmid, D.A., Irving, M.B., Posevitz, V., Hebeisen, M., Posevitz-Fejfar, A., Sarria, J.C., Gomez-Eerland, R., Thome, M., Schumacher, T.N., Romero, P., et al. (2010). Evidence for a TCR affinity threshold delimiting maximal CD8 T cell function. J. Immunol. *184*, 4936–4946.

Schulze, M.B., Schulz, M., Heidemann, C., Schienkiewitz, A., Hoffmann, K., and Boeing, H. (2007). Fiber and magnesium intake and incidence of type 2 diabetes: a prospective study and meta-analysis. Arch. Intern. Med. *167*, 956–965.

Schürpf, T., and Springer, T.A. (2011). Regulation of integrin affinity on cell surfaces. EMBO J *30*, 4712–4727.

Semmrich, M., Smith, A., Feterowski, C., Beer, S., Engelhardt, B., Busch, D.H., Bartsch, B., Laschinger, M., Hogg, N., Pfeffer, K., and Holzmann, B. (2005). Importance of integrin LFA-1 deactivation for the generation of immune responses. J. Exp. Med. *201*, 1987–1998.

Sen, M., Koksal, A.C., Yuki, K., Wang, J., and Springer, T.A. (2018). Ligandand cation-induced structural alterations of the leukocyte integrin LFA-1. J. Biol. Chem. *293*, 6565–6577.

Shimaoka, M., Salas, A., Yang, W., Weitz-Schmidt, G., and Springer, T.A. (2003). Small molecule integrin antagonists that bind to the b2 subunit I-like domain and activate signals in one direction and block them in the other. Immunity *19*, 391–402.

Siddiqi, T., Soumerai, J.D., Dorritie, K.A., Stephens, D.M., Riedell, P.A., Arnason, J.E., Kipps, T.J., Gillenwater, H.H., Gong, L., and Dubovsky, J.A. (2019). Rapid undetectable MRD (uMRD) responses in patients with relapsed/refractory (R/R) chronic lymphocytic leukemia/small lymphocytic lymphoma (CLL/ SLL) treated with lisocabtagene maraleucel (liso-cel), a CD19-directed CAR T cell product: updated results from transcend CLL 004, a phase 1/2 study including patients with high-risk disease previously treated with ibrutinib. Blood *134*, 503.

Sojka, J.E., and Weaver, C.M. (1995). Magnesium supplementation and osteoporosis. Nutr. Rev. *53*, 71–74.

Thomas, R., Al-Khadairi, G., Roelands, J., Hendrickx, W., Dermime, S., Bedognetti, D., and Decock, J. (2018). NY-ESO-1 based immunotherapy of cancer: current perspectives. Front. Immunol. *9*, 947.

Topp, M.S., Gökbuget, N., Stein, A.S., Zugmaier, G., O'Brien, S., Bargou, R.C., Dombret, H., Fielding, A.K., Heffner, L., Larson, R.A., et al. (2015). Safety and activity of Blinatumomab for adult patients with relapsed or refractory B-precursor acute lymphoblastic leukaemia: A multicentre, single-arm, phase 2 study. Lancet Oncol *16*, 57–66.

Trebak, M., and Kinet, J.P. (2019). Calcium signalling in T cells. Nat. Rev. Immunol. *19*, 154–169.

Valdramidou, D., Humphries, M.J., and Mould, A.P. (2008). Distinct roles of beta1 metal ion-dependent adhesion site (MIDAS), adjacent to MIDAS (ADMIDAS), and ligand-associated metal-binding site (LIMBS) cation-binding sites in ligand recognition by integrin alpha2beta1. J. Biol. Chem. *283*, 32704–32714.

van Aalderen, M.C., van den Biggelaar, M., Remmerswaal, E.B.M., van Alphen, F.P.J., Meijer, A.B., Ten Berge, I.J.M., and van Lier, R.A.W. (2017). Label-free analysis of CD8+ T cell subset proteomes supports a progressive differentiation model of human-virus-specific T cells. Cell Rep *19*, 1068–1079.

Vorup-Jensen, T., Waldron, T.T., Astrof, N., Shimaoka, M., and Springer, T.A. (2007). The connection between metal ion affinity and ligand affinity in integrin I domains. Biochim. Biophys. Acta *1774*, 1148–1155.

Wang, Y., Li, D., Nurieva, R., Yang, J., Sen, M., Carreñ o, R., Lu, S., McIntyre, B.W., Molldrem, J.J., Legge, G.B., and Ma, Q. (2009). LFA-1 affinity regulation is necessary for the activation and proliferation of naive T cells. J. Biol. Chem. *284*, 12645–12653.

Zhan, Y., Chen, R., Zheng, W., Guo, C., Lu, L., Ji, X., Chi, Z., and Yu, J. (2014). Association between serum magnesium and anemia: China health and nutrition survey. Biol. Trace Elem. Res. *159*, 39–45.

Zhang, K., and Chen, J. (2012). The regulation of integrin function by divalent cations. Cell Adh. Migr. *6*, 20–29.

KEY RESOURCE TABLE

REAGENT or RESOURCE	SOURCE	IDENTIFIER
Antibodies		
Mouse Anti-Human CD3	BioLegend	Cat# 300333
Mouse Anti-Human CD28	BioLegend	Cat# 302943
Armenian Hamster Anti-Mouse CD3	BioLegend	Cat# 100359
Syrian Hamster Anti-Mouse CD28	BioLegend	Cat# 102121
Mouse Anti-Human CD11a/CD18 (LFA-1) (clone m24), unlabeled, AF488, PE	BioLegend	Cat# 363402 Cat# 363406 Cat# 363404
Mouse Anti-Human CD11a (clone TS2/4), unlabeled, FITC	BioLegend	Cat# 350602 Cat# 350604
Mouse Anti-Human CD18 (clone KIM127), unlabeled	M. Sperandio, LM University Munich and InVivo Biotech Services GmbH	custom
Mouse Anti-Human CD18 (clone CBR LFA-1/2)	BioLegend	custom
Mouse Anti-Human CD18 (clone TS1/18)	BioLegend	Cat# 302116
Mouse Anti-Human CD54 (ICAM-1)	ThermoFisher	Cat# 16-0549-82
Mouse Anti-Human CD102 (ICAM-2)	ThermoFisher	Cat# BMS109
Mouse Anti-Human CD50 (ICAM-3)	ThermoFisher	Cat# BMS111
Mouse IgG1 κ Isotype control	BioLegend	Cat# 400166
Mouse IgG1 κ Isotype control	ThermoFisher	Cat#16-4714-82
Mouse IgG2a κ Isotype control	ThermoFisher	Cat#16-4724-82
InVivoMab Anti-Mouse CD3ε F(ab')2 fragment	BioXCell	Cat# BE0001-1FAB
InVivoMab Anti-Mouse PD-1 (CD279)	BioXCell	Cat# BE0146
InVivoMAb Anti-Mouse CD16/CD32	BioXCell	Cat# BE0307
InVivoMab rat IgG2a isotype control	BioXCell	Cat# BE0089
Rabbit Anti-Human/Mouse phospho-FAK (Tyr397)	ThermoFisher	Cat# 700255
Phospho-Tyrosine (P-Tyr-1000) MultiMab Rabbit mAb mix	Cell Signaling Technology	Cat# 8954
Phospho-p44/42 MAPK (Erk1/2) (Thr202/Tyr204), Rabbit mAb	Cell Signaling Technology	Cat# 4370
Phospho-c-Jun (Ser73), Rabbit mAb	Cell Signaling Technology	Cat# 3270
p44/42 MAPK (Erk1/2), Rabbit mAb	Cell Signaling Technology	Cat# 137F5
c-Jun, Rabbit mAb	Cell Signaling Technology	Cat# 60A8
β-Actin, Mouse mAb	Cell Signaling Technology	Cat# 8H10D10
Recombinant Anti-gamma Tubulin	Abcam	Cat# ab179503
Purified Mouse Anti-Human Perforin	BD Biosciences	Cat# 556434
Goat anti-Mouse IgG (H+L) Highly Cross-Adsorbed Secondary Antibody, Alexa Fluor 568	ThermoFisher	Cat# A-11031
Goat anti-Rabbit IgG (H+L) Highly Cross-Adsorbed Secondary Antibody, Alexa Fluor 647	ThermoFisher	Cat# A-21245
Goat anti-Mouse IgG1 Cross-Adsorbed Secondary Antibody, Alexa Fluor 488	ThermoFisher	Cat# A-21121
Mouse anti-ERK1/2 Phospho (Thr202/Tyr204), AF647	BioLegend	Cat# 369504
Hamster Anti-Mouse CD3, BUV805	BD Biosciences	Cat# 749276
Rat anti-mouse CD4, BUV496	BD Biosciences	Cat# 612952
Hamster Anti-mouse CD8a, eFluor 450	eBioscience	Cat# 48-0081-82

Rat Anti-mouse CD11b, APC/Cyanine7	BioLegend	Cat# 101226
Armenian Hamster Anti-Mouse CD11c, FITC	BioLegend	Cat# 117306
Rat Anti-Mouse CD19 Antibody, BB515	BD Biosciences	Cat# 564509
Rat Anti-Mouse CD25 Antibody, PE-Cyanine5.5	eBioscience	Cat# 35-0251-82
Rat Anti-Mouse CD45, BUV395	BD Biosciences	Cat# 565967
Armenian Hamster Anti-Mouse CD80 Antibody, FITC	BioLegend	Cat# 104706
Hamster Anti-Mouse CD103, BV650	BD Biosciences	Cat# 748256
Armenian Hamster Anti-Mouse CD80, Brilliant Violet 605	BioLegend	Cat# 104729
Rat Anti-Mouse CD206, Brilliant Violet 711	BioLegend	Cat# 141727
Hamster Anti-Mouse CD183 (CXCR3), BUV737	BD Biosciences	Cat# 741895
Rat Anti-Mouse F4/80, Alexa Fluor 647	BioLegend	Cat# 123122
FOXP3, rat mAb, APC	eBioscience	Cat# 17-5773-82
Granzyme B, mouse mAb, PE-eFluor 610	Inivtrogen	Cat# 61-8898-82
Ki-67, rat mAb, Alexa Fluor 532	eBioscience	Cat# 58-5698-82
Rat Anti-mouse CD11a (LFA-1alpha), Super Bright 436	ThermoFisher	Cat# 62-0111-82
Rat Anti-Mouse Ly-6G, BUV563	BD Biosciences	Cat# 612921
Rat Anti-Mouse Ly-6c, PerCP	BioLegend	Cat# 128028
Rat Anti-Mouse I-A/I-E (MHCII), BV510	BioLegend	Cat# 107636
Rat Anti-Mouse CD335 (NKp46), BV563	BD Biosciences	Cat# 741435
Rat Anti-Mouse CD279 (PD-1), Brilliant Violet 785	BioLegend	Cat# 135225
Rat Anti-Mouse CD274 (PD-L1), Brilliant Violet 421	BioLegend	Cat# 124315
Rat Anti-Mouse TCF7/TCF1, Alexa fluor 700	R&D Systems	Cat# FAB8224N
Mouse Anti-Mouse CD366 (TIM-3), BB700	BD Biosciences	Cat# 747619
Rat Anti-Mouse CD8a, FITC	BioLegend	Cat# 100706
Rat Anti-Mouse CD11b, PE/Cyanine5	BioLegend	Cat# 101210
Armenian Hamster Anti-Mouse CD11c, PE/Cyanine5	BioLegend	Cat# 117316
Rat Anti-Mouse/Human CD45R/B220, PE/Cyanine5	BioLegend	Cat# 103210
Rat Anti-Mouse F4/80	BioLegend	Cat# 123112
Rat Anti-Mouse CD69, APC	BioLegend	Cat# 104514
Rat Anti-Mouse CD107a (LAMP-1)	BioLegend	Cat# 121620
Tetramer/PE - H-2 Kb OVA (SIINFEKL)	Tetramers core facility, University of Lausanne	N/A
Rat Anti-Mouse CD11a, FITC	BioLegend	Cat# 101106
Rat Anti-Mouse CD11a/CD18, Pacific Blue	BioLegend	Cat# 141014
Rat Anti-Mouse CD107a (LAMP-1), PE/Cyanine7	BioLegend	Cat# 121620
Rat Anti-Mouse CD4, R718	BD Biosciences	Cat# 566939
Rat Anti-Mouse CD8, BUV805	BD Biosciences	Cat# 612898
Rat Anti-Mouse CD45, APC-Cy7	BioLegend	Cat# 103115
Armenian Hamster Anti-Mouse CD69, Brilliant Violet 650	BioLegend	Cat# 104541
Armenian Hamster Anti-Mouse TCRβ, Brilliant Violet 711	BioLegend	Cat# 109243
Armenian Hamster Anti-Mouse CD11c, Brilliant Violet 650	BioLegend	Cat# 117339
Armenian Hamster Anti-Mouse CD69, PE/Cyanine5	BioLegend	Cat# 104510
Armenian Hamster Anti-Mouse CD80, FITC	BioLegend	Cat# 104706
Armenian Hamster Anti-Mouse TCR γ/δ Antibody, PE	BioLegend	Cat# 118108
Mouse Anti-Mouse NK-1.1, APC	BioLegend	Cat# 108710
Rat Anti-Mouse Anti-Mouse Ly-6G/Ly-6C (Gr-1), Brilliant Violet 510	BioLegend	Cat# 108457
Rat Anti-Mouse CD11a, PE/Cyanine7	BioLegend	Cat# 153108
Rat Anti-Mouse CD19, PE/Cyanine5	BioLegend	Cat# 115510
Rat Anti-Mouse CD62L, Pacific Blue	BioLegend	Cat# 104424

Rat Anti-Mouse CD8, PE	BioLegend	Cat# 100708
Rat Anti-Mouse CD4, Brilliant Violet 650	BioLegend	Cat# 100555
Rat Anti-Mouse F4/80, PE/Cyanine7	BioLegend	Cat# 123114
Rat Anti-Mouse Ly-6C, FITC	BioLegend	Cat# 128005
Rat Anti-Mouse/Human CD11b, PE	BioLegend	Cat# 101208
Rat Anti-Mouse/Human CD44, FITC	BioLegend	Cat# 103006
Mouse Anti-Human CD54 (ICAM-1), PE	BioLegend	Cat# 353106
Mouse Anti-Human CD102 (ICAM-2), PE	BioLegend	Cat# 328506
Mouse Anti-Human CD50 (ICAM-3), PE	BioLegend	Cat# 330005
Mouse Anti-Human CD25, APC	BD Biosciences	Cat# 340939
Mouse Anti-Human CD45RA, Pacific Blue	Beckmann	Cat# 2H4LDH11LDB9
Mouse Anti-Human CD62L, APC	ImmunoTools	Cat# 21279626
Mouse Anti-Human CD69, PerCP, FITC	BioLegend	Cat# 310928 Cat# 310904
Mouse Anti-Human CD71, PE	BioLegend	Cat# 334106
Mouse Anti-Human CD107a (LAMP-1), Alexa Fluor 647	BioLegend	Cat# 328612
Mouse Anti-Human CD98, FITC	BioLegend	Cat# 315603
Mouse Anti-Human TCR V β13.1, FITC, PE/Cyanine7	BioLegend	Cat# 362404 Cat# 362406
Mouse Anti-Human TNF, APC, PE	BioLegend	Cat# 502912 Cat# 502909
Blincyto (Blinatumomab)	Amgen	N/A
Bacterial and virus strains		
Listeria monocytogenes expressing chicken Ovalbumin (AA134–387)	E. Palmer, University of Basel	N/A
NY-ESO-1 TCR lentiviral vector, codon optimized, pairing optimized: pRRL 131 (WT) T2A 1xATG Cys	Provided to M. Trefny from M. Hebeisen and N. Rufer, University of Lausanne	N/A
Anti-CD19-CD28z-T2A-copGFP	Provided to M. Trefny from W. Schamel, University of Freiburg	N/A
Biological samples		
Human Peripheral Blood Buffy Coat	Blood Donation Center Basel and Lausanne, Switzerland	N/A
Human AB+ male serum	Blood Donation Center Basel, Switzerland	N/A
Chemicals, peptides, and recombinant proteins		
BIRT377		Tocris
XVA143	Roche	N/A
NY-ESO-1 peptide 9C: SLLMWITQC >95% purity	EZ Biolabs	custom
Ovalbumin EndoFit	InvivoGen	Cat# vac-pova-100
OVA (257-264) Peptide Fragment	Eurogentec	Cat# AS- 60193
OVA-G4 Peptide, SIIGFEKL, OVA (257-264) Variant	Eurogentec	Cat# AS-64384
OVA (257-264) Variant, SIIQFERL, Q4R7	Eurogentec	custom
OVA-Q4H7 Peptide, pQ4H7, SIIQFEHL, OVA (257-264) Variant	Eurogentec	Cat# AS-64402
DAPI	Sigma Aldrich	Cat# D9542
Phalloidin-iFluor 555 Reagent	ABCAM	Cat# ab176756
CellTrace Far Red Cell Proliferation Kit	ThermoFisher	Cat# C34564
CellTrace Violet Cell Proliferation Kit	ThermoFisher	Cat# C34557
CellTrace CFSE Cell Proliferation Kit	ThermoFisher	Cat# C34554

Mag-Fluo-4, AM, cell permeant	ThermoFisher	Cat# M14206
Fluo-4, AM, cell permeant	ThermoFisher	Cat# F14201
Fura Red, AM, cell permeant	ThermoFisher	Cat# F3021
Calbryte 520 AM	AAT Bioquest	Cat# 20653
BioTracker NucView 488 Green Caspase-3 Dye	Merck Millipore	Cat# SCT100
BioTracker NucView 405 Blue Caspase-3 Dye	Merck Millipore	Cat# SCT102
NucView 488 Caspase-3 Enzyme Substrate	Biotium	Cat# 10402
CellEvent Caspase-3/7 Green Detection Reagent	ThermoFisher	Cat# C10423
Incucyte Caspase-3/7 Dye for Apoptosis	Sartorius	Cat# 4440
2-NBDG	Abcam	Cat# ab235976
Proleukin (Aldesleukin, recombinant IL-2)	Novartis	N/A
Human IL-7	Mylteni Biotec	Cat# 130-095-363
Human IL-15	Mylteni Biotec	Cat# 310-095-765
Zombie UV Fixable Viability Kit	BioLegend	Cat# 423108
Zombie Aqua Fixable Viability Kit	BioLegend	Cat# 423102
Zombie Green Fixable Viability Kit	BioLegend	Cat# 423112
Zombie Red Fixable Viability Kit	BioLegend	Cat# 423110
LIVE/DEAD Fixable Blue Dead Cell Stain Kit	ThermoFisher	Cat# L34962
LIVE/DEAD Fixable Near-IR Stain Kit	ThermoFisher	Cat# 15519340
CD8 MicroBeads human	Mylteni Biotec	Cat# 130-045-201
CD8a (Ly-2) MicroBeads mouse	Mylteni Biotec	Cat# 130-117-044
LS Cloumns	Mylteni Biotec	Cat# 130-042-401
T cell stimulation and expansion kit	Mylteni Biotec	Cat# 130-091-441
Cas9	QB3 MacroLab, UC Berkeley	N/A
EasySep Mouse Naïve CD8+ T Cell Isolation Kit	Stem Cell Technologies	Cat# 19858
EasySep Mouse CD8+ T Cell Isolation Kit	Stem Cell Technologies	Cat# 19853
EasySep Mouse CD4+ T Cell Isolation Kit	Stem Cell Technologies	Cat# 19852
Critical commercial assays		
P4 Primary Cell 4D-Nucleofector X Kit L	Lonza	Cat# V4XP-4024
Cell Line Nucleofector Kit V	Lonza	Cat# VCA-1003
ELISA MAX Deluxe Set Human IFN-γ	BioLegend	Cat# 430104
LEGENDplex Human Th1 Panel (5-plex)	BioLegend	Cat# 741036
LEGENDplex Mouse Th1 Panel (5-plex)	BioLegend	Cat# 740025
ProQuantumMouse Granzyme B Immunoassay Kit	Inivtrogen	Cat# A44238
Mouse ANA (Anti-nuclear Antibody) ELISA Kit	Hoelzl Biotech	Cat# MBS7606315-96
Deposited data		
N/A		
Experimental models: Cell lines		
Jurkat, Clone E6-1	ATCC	RRID:CVCL_0367
HEK-293T	ATCC	RRID:CVCL_0063
T2	A. Zippelius, University of Basel	RRID:CVCL_2211
Ramos	A. Zippelius, University of Basel	RRID:CVCL:0597
LCL	G. Bantug, University of Basel	
EL4	A. Zippelius, University of Basel	RRID:CVCL_0255
PC3-PIP	Provided to M. Irving by A. Rosato, University of Padua	N/A

MC38-OVA	Provided to A. Marti from P. Romero, University of Lausanne	RRID_CVCL_XY96
Experimental models: Organisms/strains		
C57BL/6NRj	Animal Facility University of	N/A
C57BL/6NCrl	Animal Facility University of Basel, Charles River, Janvier	N/A
OT-I (B6.129S6-Rag2tm1Fwa Tg(TcraTcrb)1100Mjb)	Taconic, Animal Facility University of Basel	Cat# 2334
LFA-1 KO (B6.129S7-Itgaltm1Bll/J)	Jackson Laboratory, Animal Facility University of Basel	Cat# 005257
NSG (NOD.Cg-Prkdc<scid>Il2rg<tm1Wjl>SzJ)	Animal Facility University of Basel and University of Lausanne	N/A
Oligonucleotides		
Hs.Cas9.ITGAL.1.AA (TGCCCGACTGGCACTGATAG)	Integrated DNA Technologies IDT	N/A
Mm.Cas9.ITGAL.1.AB (CACATAGTTGATGGCACGAA)	Integrated DNA Technologies IDT	N/A
RISPR-Cas9 Negative Control crRNA #1	Integrated DNA Technologies IDT	Cat# 224163224
Alt-R CRISPR-Cas9 tracrRNA	Integrated DNA Technologies IDT	Cat# 222427350
Recombinant DNA		
N/A		
Software and algorithms		
FlowJo	BD Biosciences	https://www.flowjo.com/
GraphPad Prism	GraphPad Software Inc.	https://www.graphpad.com/scientific-software/prism/
ImageLab	Biorad	https://www.bio-rad.com/
FiJi	National Institute of Health	https://imagej.net/software/fiji/
Huygens - Huygens Remote Manager - Deconvolution	N/A	https://www.huygens-rm.org/wp/
OMERO - The Open Microscopy Environment	OME	https://www.openmicroscopy.org/
Imaris	Bitplane	https://imaris.oxinst.com/
BioRender	N/A	https://biorender.com/
Other		
AIN-76A Rodent Diet	Research Diets, Inc.	Cat# D1001
AIN-76A Rodent Diet Without Added Magnesium	Research Diets, Inc.	Cat# D16601

Lead contact

Further information and requests for resources and reagents should be directed to and will be fulfilled by the lead contact, Christoph Hess (ch818@cam.ac.uk, or chess@uhbs.ch).

Material availability

This study did not generate new unique reagents.

Data and code availability

This study did not generate or analyze unique datasets or code.

EXPERIMENTAL MODELS AND SUBJECT DETAILS

Cell Lines

Primary T cells were obtained from Buffy coats of healthy donors (Blood donor center, University Hospital Basel or Blood donor center Lausanne). Jurkat T cells (Clone E61, TIB-152) and HEK-293T were originally purchased from ATCC. T2, Ramos and EL4 cells were kindly provided by A. Zippelius (University of Basel). MC38-OVA cells were provided by P. Romero (University of Lausanne). PC3-PIP cell lines were provided by A. Rosato (University of Padua, Padova). Lymphoblastoid cell lines (LCLs) were provided by G. Bantug (University of Basel).

For the culture of primary human $CD8^+$ T cells, PHA-induced T cell blasts, Jurkat T cells, PC3-PIP, Ramos, LCL and T2 cells, RPMI-1640 medium (Invitrogen) was supplemented with heat-inactivated 10% fetal calf serum (HI FCS, Gibco), 50 U mL^{-1} penicillin (Invitrogen) and 50 µg mL^{-1} streptomycin (Invitrogen). Human REP T cells were expanded in AIM V medium (ThermoFisher) mixed 1:1 with RPMI-1640 (Invitrogen) supplemented with 10% human HI AB serum, 50 U mL^{-1} penicillin (Invitrogen) and 50 µg mL^{-1} streptomycin, 1 mM pyruvate (Gibco), 1% MEM Non-Essential Amino Acids (Gibco), 1% GlutaMAX (Gibco) and 3,000 U mL^{-1} human recombinant IL-2 (Proleukin, Novartis). Murine T cells und EL4 cells were kept in RPMI-1640 medium containing 10% HI FCS, 100 U mL^{-1} penicillin, 100 µg streptomycin, 0.29 mg mL^{-1} L-glutamine, 50 µM 2-Mercaptoethanol (Invitrogen). 293T human embryonic kidney (HEK-293T) were cultured in RPMI-1640 supplemented with 10% HI FCS, 2 mmol l-glutamine, 100 µg mL^{-1} penicillin and 100 U mL^{-1} streptomycin (all purchased from Invitrogen). MC38-OVA cells were maintained in RPMI-1640-Glutamax medium supplemented with 10% FCS, 50 U mL^{-1} penicillin and 50 µg mL^{-1} streptomycin, 1 mM sodium pyruvate, 50 µM 2-Mercaptoethanol and under geneticin selection (0.4 mg mL^{-1} G418). All reagents were purchased from Gibco. Magnesium-free medium was made in-house, using double distilled water supplemented according to manufacturer's instruction with RPMI-1640 amino acid solution (Sigma Aldrich), RPMI-1640 vitamin solution (Sigma Aldrich), 1% GlutaMAX (Gibco), 25 mM HEPES (Gibco), 2 g L^{-1} sodium bicarbonate (Sigma Aldrich), 2g L^{-1} glucose (Sigma Aldrich), 100 mg L^{-1} calcium nitrate (Sigma Aldrich), 400 mg L^{-1} potassium chloride (Sigma Aldrich), 6 g L^{-1} sodium chloride (Sigma Aldrich), 800 mg L^{-1} sodium phosphate dibasic (Sigma Aldrich), 1 mg L^{-1} Glutathion (Sigma Aldrich), 50 U m^{-1} penicillin and 50 µg mL^{-1} streptomycin and 10% HI dialyzed FCS (dFCS, Gibco). For functional readouts, the medium was either supplemented, as indicated, with 1.2 mM $MgCl_2$ or 0.05 mM $MnCl_2$ or left untreated (=0 mM Mg^{2+}). Cells of every condition were washed initially twice in magnesium-free medium prior to any functional read out. Low background Mg^{2+} values in *self-made* medium was verified by ICP-MS (data not shown).

Mice

Information on sex and age of the mice used in each experimental setting can be found in the corresponding section. C57BL/6NRj, C57BL/6NCrl and NOD.Cg-Prkdc<scid>Il2rg<tm1Wjl>SzJ (NSG) mice were bred and housed at specific pathogen free (SPF) conditions at the Universities of Basel or Lausanne. MHC class I-restricted OVA-specific T cell receptor (B6.129S6-Rag2tm1Fwa Tg(TcraTcrb)1100Mjb) (OT-I) transgenic, B6.129S7-Itgaltm1Bll/J

(LFA-1 KO) were originally purchased from Taconic (OT-I) or Jackson Laboratories (LFA-1 KO), and thereafter bred and housed at SPF conditions at the University of Basel. For some experiments, C57BL/6NCrl were purchased from Charles River as well as Janvier, and maintained at SPF conditions and acclimatized for 1 week prior to experiments at the animal facilities of the Universities of Geneva or Basel, respectively. Anti-CD19 CAR T cell experiments were conducted with NSG mice at the University of Basel. Anti-PSMA CAR T cell experiments were conducted with NSG mice which were bred and housed in a specific and opportunistic pathogen-free animal facility in the Oncology Department of the University of Lausanne. All experiments were conducted in accordance to the Swiss Federal Veterinary Office guidelines and were approved by the Cantonal Veterinary Office (Canton of Basel-Stadt, Vaud and Geneva). All cages provided free access to food and water. During experimentation, all animals were monitored at least every other day for signs of distress and, if required, body weight was measured three times a week. Mice were sacrificed at the endpoint by carbon dioxide overdose.

Human Data

The retrospective analysis of diffuse large B cell lymphoma (DLBCL) cohort treated with Axicabtagene ciloleucel (Axi-cel) was approved by the Institutional Review Board of MD Anderson Cancer Center and conducted in accordance with institutional guidelines and the principles of the Declaration of Helsinki. All included patients provided written informed consent. The SAKK16/14 trial (NCT02572843) was conducted in accordance with the principles of the Declaration of Helsinki. The protocol was approved by the ethics committee of each participating site. Written informed consent was obtained from all patients.

METHOD DETAILS

Chemicals

LFA-1 inhibitor studies were performed using BIRT377 (Tocris) and XVA143 (Roche). Both inhibitors were used at 10 µM. TCR independent activation of T cells were conducted with PMA (50 ng mL^{-1}; Sigma Aldrich) and ionomycin (1 µg mL^{-1}; Sigma Aldrich). All chemicals were aliquoted in DMSO and stored at -20°C until used.

aliquoted in DMSO and stored at -20°C until used.

Flow cytometry

Either a BD Fortessa LSR II (BD Bioscience), Cytek Aurora (Cytek Biosciences) or Cytoflex S (Beckmann) flow cytometer were used for flow cytometry. For analysis of surface markers, T cells were harvested at indicated time points after activation *in vitro*, washed once in cold PBS and, if required, stained with Fixable Viability Dyes for 15 min at 4°C. Surface markers were stained with appropriate antibodies for 20 min at 4°C. For stainings of cell suspension from murine organs, cells were additionally pre-incubated with anti-mouse Fc block 10 µg mL^{-1} (anti-CD16/CD32, BioXCell). For intracellular TNF staining, cells were activated for 4 h. During the final 2 h of activation, cells were treated either with brefeldin A solution (BioLegend) to block cytokine secretion. Cells were then washed and fixed for 20 min at RT (fixation/permeabilization solution, BD Biosciences) and washed with permeabilization buffer (BD Biosciences) prior to staining for 45 min and further washing before acquisition. For analysis of protein phosphorylation, T cells were stimulated as indicated and stained as previously described (Krutzik and Nolan, 2003). Briefly, for assessment of phosphorylation of ERK1/2, c-Jun and FAK, T cells were activated for 45 min either by CD3/28 Ab, antigen-pulsed target cells or PMA/Ionomycin. Cells were fixed by adding 8% Paraformaldehyde (PFA) (ThermoFisher) directly into the culture medium to obtain a final

concentration of 4% PFA. Cells were incubated for 15 min at RT, washed with FACS buffer, followed by permeabilization with ice cold methanol at 4°C for 5 min. After washing with FACS buffer, cells were stained at room temperature for 30 min, washed and acquired. For evaluation of activation-induced LFA-1 conformation, T cells were cultured in respective medium for 45 min ± activation (CD3/28 Ab or antigen-pulsed target cells). For probing of open headpiece anti-human CD11a/CD18 (clone m24) was directly added to the medium and incubated for 15 min at 37°C followed by incubation on ice for 20 min. Cells were then washed twice in FACS Buffer and fixed in 2% PFA, incubated at room temperature for 20 min and washed with FACS Buffer before acquisition. For assessment of LFA-1 extension, the anti-human CD18 (clone KIM127) was used. The cells were activated for 45 min, fixed directly in medium with PFA at a final concentration of 2%, washed and then incubated with KIM127. For 2-NBDG uptake assays, previously activated T cells were co-incubated for last 45 min of experiment directly with a final concentration of 20 µM 2-NBDG (Abcam). Cells were washed twice in FACS buffer before acquisition. The following antibodies were used:

Human in vitro activation: CD11a (FITC, BioLegend), CD18 (PE, BioLegend), CD25 (APC, BD Biosciences), CD45RA (Pacific Blue, Beckmann), CD62L (APC, Immuno Tools), CD69 (PerCP, FITC, BioLegend), CD71 (PE, BioLegend), CD107a (AF647 and PE-Cy7, both BioLegend), CD98 (FITC, BD Bioscience and BioLegend), ICAM-1 (PE, BioLegend), ICAM-2 (PE, BioLegend), ICAM-3 (PE, BioLegend), m24 epitope LFA-1 (PE, BioLegend), phospho-c-Jun (Ser_{73}, unlabeled, Cell Signaling Technology), phospho-ERK1/2 (Thr_{202}/Thr_{204}, AF647, BioLegend), phospho-FAK (Tyr_{397}, unlabeled, ThermoFisher), goat anti-rabbit IgG (AF488, ThermoFisher), goat anti-mouse IgG1 (AF488, ThermoFisher), TCR V β13.1 (FITC and PE-Cy7, BioLegend), TNF (PE, APC, BioLegend), Viability Dye (Aqua Zombie, BioLegend; Zombie Green, BioLegend).

Murine in vitro activation: CD11a (FITC, BioLegend), LFA-1 (BV421, BioLegend), CD8a (FITC, BioLegend), CD69 (APC, BioLegend), CD107a (PE-Cy7, BioLegend), phospho-ERK1/2 (Thr_{202}/Thr_{204}, AF647, BioLegend), phospho-FAK (Tyr_{397}, unlabeled, ThermoFisher), goat anti-rabbit IgG (AF488, ThermoFisher), Viability Dye (Aqua Zombie, BioLegend).

Murine immune cell subset characterization in vivo (comprising 3 individual stainings): CD4 (BV650, BioLegend), CD8 (PE, BioLegend), CD11a (PE/Cy7, BioLegend), CD11b (PE, BioLegend), CD11c (BV650, BioLegend), CD19 (PE/Cy5, BioLegend), CD44 (FITC, BioLegend), CD62L (PB, BioLegend), CD69 (PE/Cy5, BioLegend), CD80 (FITC, BioLegend), F4/80 (PE/Cy7, BioLegend), Gr-1 (BV510, BioLegend), Ly6-C (FITC, BioLegend), NK1.1 (APC, BioLegend), TCR γ/δ (PE, BioLegend), LIVE/DEAD Fixable Near-IR (ThermoFisher)

Polyclonal CD8 T cell activation in vivo with anti-CD3ε F(ab')2 fragment: CD4 (R718, BD Bioscience), CD8 (BUV805, BD Bioscience), CD45 (APC-Cy7, BioLegend), CD69 (BV650, BioLegend), TCRβ (BV711, BioLegend), LIVE/DEAD Fixable Blue Dead Cell Stain Kit (ThermoFisher).

Murine peritonitis model: CD8 (FITC, BioLegend), CD11b (PE-Cy5, BioLegend), CD11c (PE-Cy5, BioLegend), CD69 (APC, BioLegend), CD107a (PE/Cy7, BioLegend), B220 (PE-Cy5, BioLegend), F4/80 (PE-Cy5, BioLegend), Tetramer H-2 Kb OVA (PE, Tetramer core facility, University of Lausanne), Viability Dye (Zombie Red, BioLegend,).

MC38-OVA tumor model: CD3 (BUV805, BD Biosciences), CD4 (BUV496, BD Biosciences), CD8 (eFluor450, eBioscience), CD11b (APC-Cy7, BioLegend), CD11c (FITC, BioLegend), CD19 (BB515, BD Biosciences), CD25 (PE-Cy5.5, eBioscience), CD45 (BUV385, BD Biosciences), CD80 (BV605, BioLegend), CD103 (BV650, BD Biosciences),

CD206 (BV711, BioLegend), CXCR3 (BUV737, BD Biosciences), F4/80 (AF647, BioLegend), FoxP3 (APC, eBioscience), GzmB (PE-eFluor610, Inivtrogen), Ki67 (AF532, eBioscience), LFA-1 (SB436, ThermoFisher), Ly-6G (BUV563, BD Biosciences), Ly-6c (PerCP, BioLegend), MHCII (BV510, BioLegend), NKp46 (BUV563, BD Biosciences), PD-1 (BV785, BioLegend), PD-L1 (BV421, BioLegend), TCF-7 (AF700, R&D Systems), Tim-3 (BB700, BD Biosciences), Zombie UV Fixable Viability Kit (BioLegend).

Human naïve and memory T cell isolation

Blood samples were obtained from healthy male and female donors (18-65 years old) as buffy coats after written informed consent (Blood donor center, University Hospital Basel). Peripheral blood mononuclear cells (PBMCs) were isolated by standard density-gradient centrifugation protocols (Lymphoprep; Fresenis Kabi). MACS beads and LS columns (both Milteny Biotec) were used to sort $CD8^+$ positive T cells. The positively selected $CD8^+$ T cells were incubated with APC anti-CD62L mAb (ImmunoTools) and Pacific Blue anti-CD45RA (Beckman Coulter). Naïve and EM $CD8^+$ T cells were identified as $CD62L^+$ $CD45RA^+$ and $CD62L^-$ $CD45RA^-$ populations, respectively. Cell sorting was performed using a BD FACSAria III or BD influx cell sorter (BD Bioscience). Cells were rested for 24 h at 37°C prior to further experiments.

Metabolic assays

A Seahorse XF-96e extracellular flux analyzer (Seahorse Bioscience, Agilent) was used to determine the metabolic profile of cells. T cells were plated (2×10^5 cells/well) onto Celltak (Corning, USA) coated cell plates. Experiments were carried out in unbuffered, serum- and Mg^{2+}-free *self-made* medium. Medium was reconstituted with 1.2 mM $MgCl_2$ or 0.05 $MnCl_2$ as indicated in individual experiments. Reconstitution of cations was either present from beginning of experiment or applied onto plated cells via the instrument's multi-injection port. All following concentration represent final well concentrations of indicated substance. Human T cells were activated by injection anti-CD3 Ab (1 µg mL^{-1}) and anti-CD28 Ab (10 µg mL^{-1}). Murine T cells were activated by injection anti-CD3 Ab (5 µg mL^{-1}) and anti-CD28 Ab (2.5 µg mL^{-1}). Glycolytic activity was quantified by subtracting maximal ECAR from baseline ECAR-measurements. Mitochondrial perturbation experiments were carried out by sequential addition of oligomycin (1 µM, Sigma Aldrich), FCCP (2 µM, Carbonyl cyanide 4-(trifluoromethoxy) phenylhydrazone, Sigma Aldrich), and rotenone (1 µM, Sigma Aldrich). Glycolysis stress test was performed in medium as described above but devoid of glucose. Sequential injections of glucose (10 mM, Sigma Aldrich), oligomycin (1 µM) and 2-deoxy-glucose (50 mM, Sigma Aldrich). Oxygen consumption rates (OCR, pmol/min) and extracellular acidification rates (ECAR, mpH/min) were monitored in real time after injection of each compound.

Flow cytometry-based Mg^{2+} and Ca^{2+} flux assay

Naïve and EM $CD8^+$ T cells were washed and incubated in Mg^{2+} or Ca^{2+} free medium for 1 h, followed by loading with MagFluo4 (ThermoFisher) or Fluo4 (ThermoFisher) and FuraRed (ThermoFisher) at a final concentration of 2 µM, in Mg^{2+}- or Ca^{2+}-free Dulbecco's phosphate-buffered saline (DPBS, ThermoFisher) for 30 min at 37°C. The cells were washed twice in DPBS, and $0.5\text{-}1\times10^6$ cells were acquired using an AccuriC6 flow cytometer (Becton Dickinson). The buffer was reconstituted with 3 mM $MgCl_2$ or 3 mM $CaCl_2$ at the indicated time points.

Generation of human T cell blasts (PHA-blasts)

PBMCs were obtained as described above and activated with 10 μg mL^{-1} Phytohaemagglutinin (PHA, ThermoFisher) and 300 U mL^{-1} human recombinant IL-2 (Proleukin, Novartis). PHA-blasts were expanded by adding fresh IL-2 every 3-4 days.

***In vitro* activation primary human T cells and PHA-blasts**

Unless stated otherwise, human EM $CD8^+$ T cells and PHA-blasts were activated in presence of plate-bound anti-CD3 Ab (HIT3a, BioLegend) at 1 μg mL^{-1} and soluble anti-CD28 Ab (CD28.2, BioLegend) at 5 μg mL^{-1}. Naïve $CD8^+$ T cells were activated with in-house generated anti-CD3/anti-CD28 coated microbeads. Polybead microspheres (4.5 mm, Polyscience Eppenheim) were incubated with 1 μg anti-CD3 Ab and 10 μg anti-CD28 Ab. T cells were plated at 2×10^5 cells per well in flat bottom 96 well plates (Greiner Bio One) in self-made medium supplemented with 10% dFCS and indicated supplementation of cations or LFA-1 inhibitor. For analysis of surface markers, primary human T cells were activated for 24 h, PHA-blasts for 4 h. For phospho-flow and LFA-1 conformational states, T cells were activated for 45 min. When using inhibitory or activating antibodies or chemical LFA-1 inhibitors, T cells were pre-incubated with respective treatment for 20 min before activation.

Venn Diagram

Venn diagram visualizes the following gene lists: metal ion binding (GO:0046872), leukocyte cell-cell adhesion (GO:0007159), immunological synapse (GO:0001772) and differentially expressed protein between naïve and memory $CD8^+$ T cells (memory>naïve) (van Aalderen et al., 2017). Venn diagram was made with InteractiVenn online tool (Heberle et al., 2015).

ICAM blockade

PHA blasts were pre-incubated with respective anti-ICAM or isotype control antibody (anti-ICAM-1 *HA58*, anti-ICAM-2 *CBR-IC2/2*, anti-ICAM-3 *CBR-IC3/1* and matching isotype control, all from ThermoFisher) at a concentration of 10 μg mL^{-1} for 20 min at room temperature prior to activation.

NY-ESO Peptides

NY-ESO-9c peptide (SLLMWITQC) was purchased in >95% purity from EZ Biolabs. Lyophilized peptides were resuspended at 10 mM in sterile dimethyl sulfoxide (DMSO) and stored at -20°C until further use.

T Cell Receptor Construct for REP T cells

The lentiviral construct encoding for the codon-optimized WT LAU155 NY-ESO-1 T cell receptor α and β chains under an hPGK promotor separated by an IRES domain was kindly provided by M. Hebeisen and N. Rufer at the University of Lausanne (Hebeisen et al., 2013; Schmid et al., 2010). This TCR has a K_D=21.4 μM for its endogenous NY-ESO-1 SLLMWITQC peptide.

Generation of lentivirus for REP T cells

To generate lentivirus, 2.5×10^6 low passage HEK293T cells were cultured in DMEM medium (ThermoFisher) and seeded into a 15 cm tissue-culture treated dish. After 3 days, 2^{nd} generation LTR-containing donor plasmid, packaging plasmid pCMV-delta8.9 and the envelope plasmid VSV-G were mixed at a 4:2:1 ratio in non-supplemented Opti-MEM (ThermoFisher) and sterile filtered. This solution was then mixed with polyethyleneimine 25 kDa (Polysciences Inc.), also diluted in Opti-MEM at a DNA:PEI ratio of 1:3. 28 μg of DNA was transfected per 15 cm dish. After 2 days, supernatants were collected from cells (exchange medium) and filtered through a 0.45 μm PES filter. Supernatants were stored for 1 day at 4°C until the second batch of

supernatant was collected 24 h later. The supernatant containing lentiviral particles was concentrated by ultra-centrifugation at 40,000 x g for 2 h at 4°C, resuspended in 0.1% BSA in PBS, and frozen to -80°C until further use.

Transduction of human T Cells for REP T cell production

To generate NY-ESO-1 TCR specific T cells, human healthy donor PBMC were thawed and washed in PBS. $CD8^+$ T cells were then isolated using the $CD8^+$ microbeads (Miltenyi) according to the manufacturer's instructions on an AutoMACS (Myltenyi). Isolated cells were washed and resuspended in medium supplemented with 150 U mL^{-1} IL-2 and plated at 1.5 mio mL^{-1}. $CD8^+$ T cells were then activated at a 1:1 ratio with activation beads from T cell activation and expansion kit (Miltenyi) according to manufacturer's instructions. 24 h later, NY-ESO-1 TCR lentiviral particles, produced as described above, were added at a multiplicity of infection (MOI) of 2. Cells were then expanded every 2 days with fresh medium and replenishing 50 UmL^{-1} IL-2 for 5 days. NY-ESO-1 TCR positive T cells were sorted using a FACSAria III or FACS SorpAria (BD) and re-stimulated with NY-ESO-9c peptide. A cell density of 0.5–2×10^6 cells mL^{-1} was maintained for expansion and 3,000 U mL^{-1} IL-2 replaced ever third day. After 1 week of expansion, cells were either stored in liquid nitrogen or further expanded and subsequently used for functional read outs as described below.

REP T cells: activation *in vitro* and cytotoxicity assays

REP T cells were incubated with T2 target cells in flat bottom 96 well-plate at a 1:1 ratio (4-6×10^4 each). In order to distinguish the different cell populations, REP T cells were labeled with CTV and T2 target cells with carboxyfluorescein diacetate succinimydyl ester (CFSE, Invitrogen) or CFTR (Invitrogen). Prior to co-incubation, T2 target cells were pulsed with NY-ESO-9c peptide at 10^{-8} M for 30 min in magnesium-free medium before being washed and re-suspended with REP T cells in magnesium-free medium supplemented with 10% dFCS at indicated cation or LFA-1 inhibitor concentration. For all co-incubation experiments, cells were allowed to sediment without centrifugation. For analysis of protein phosphorylation, co-incubation was terminated after 25 min as described above. In these experiments, Mn^{2+} concentration was 0.5 mM instead of 0.05 mM as in all other experiments. For degranulation assays, an anti-CD107a-AF647 Ab was added directly into culture medium throughout the entire co-incubation. After 4 h, cells were harvested, washed in cold FACS Buffer and gently fixed with PFA 2% for 15 min at room temperature. Cytotoxicity was examined with NucView 488 fluorogenic caspase-3 substrate (Biotium). Fluorogenic caspase substrate was added to wells at the beginning of co-incubation at final concentration of 1 μM. After 45 min, cells were washed in FACS Buffer and gently fixed with PFA 2% for 15 min at room temperature.

Imaging of immune synapse with confocal microscopy

Pictures from immunofluorescence imaging were recorded on a Nikon Ti with a Yokogawa CSU-W2 spinning disk module on a Photometrics 95B (22 mm back-illuminated sCMOS) camera. A Nikon CFI Apo Lambda 60x objective or Nikon CFI Apo TIRF NA 1.49 100x objective was used with 1.515 oil mounted samples. Diode-pumped solid-state lasers at 405, 488, 561, and 647nm were used together with filters for DAPI (ET460/50nm), AF488 (ET525/50nm), AF555 (ET630/75nm) and AF647 (ET700/75nm) with a Quad BS Dichroic mirror. If required, raw nd2 format image stacks were deconvoluted using Huygens using a theoretical point spread function classical maximum likelihood estimation using 100 iterations and a quality stop criterion of 0.05.

Immunofluorescent staining of immune synapse components of REP T cell/T2 cell conjugates

REP T cells and T2 target cells were individually labeled with CTV or CFSE. T2 cells were loaded with 10^{-7} M NY-ESO-9c peptide for 30 min. T2 and REP T cells were washed three times in serum- and Mg^{2+}-free medium, mixed 1:1 and resuspended to a final concentration of 2.5×10^6 cells mL^{-1}. Cell suspension was incubated 5 min at RT, before aliquoting in 50 µl onto glass multi-well slides (ThermoFisher) and incubating for indicated time. Cell conjugates were fixed for 20 min at RT in 4% methanol-free PFA (Sigma Aldrich), permeabilized with 0.1% Triton-X100 (Sigma Aldrich) in PBS for 5 min and quenched with 50 mM Glycine (Sigma Aldrich) in PBS for 20 min. Fixation was followed by blocking in 1% bovine serum albumin (Sigma Aldrich) in PBS (blocking buffer) for 45 min at 4°C. Primary antibodies were then incubated in the same blocking buffer for 1 h at RT or overnight at 4°C. Samples were then washed four times with blocking buffer, followed by incubation with secondary antibodies in blocking buffer at room temperature for 1 h. Slides were then mounted with Prolong Diamond Antifade Mountant (ThermoFisher) and analyzed after 24 h of curing. Of note, for visualization of extended LFA-1, m24 antibody was added directly in multi-well slides during co-incubation and cells were fixed after 10 min. The following reagents and antibodies were used for staining: CD11a/CD18 (clone m24, BioLegend), gamma Tubulin (clone EPR16793, Abcam), perforin (clone δG9, BD Bioscience), phospho-tyrosine P-Tyr-1000 (#8954S, Cell Signaling Technology), secondary goat anti-mouse (AF568, ThermoFisher), secondary goat anti-rabbit (AF647, ThermoFisher) and DAPI (Sigma Aldrich)

Image analysis and quantitation of REP T cell-T2 target cell conjugates

For analysis of extended LFA-1 and pan phospho-tyrosine intensity in REP T cells, confocal *Z*-stacks were acquired and analyzed using Imaris software (Bitplane). REP T cell volumes were identified using the *surface*-tool: source channel 4 (DAPI=CTV), 5 µm diameter cut-off with 0.369 µm surface detail and > 1689 voxels. Fluorescent signal of source channel 3 (AF555=LFA-1 m24 staining) outside of REP T cell-surface was masked and extended LFA-1 was quantified with *surface*-tool: source channel 5 (masked AF555), 1.39 µm diameter cut-off with 0.369 µm surface detail and > 154 voxels. Number of LFA-1 m24-objects were normalized to REP T cell number per field of view. Pan phospho-tyrosine intensity was determined by plotting *median intensity* of source channel 2 (AF647) per REP T cell volume identified as described above. For analysis of perforin and centrosome polarization, position of REP T and T2 target cells in confocal *Z*-stacks were characterized with *spot*-tool: Source channel 1 (AF488=CFSE) with the following parameters 10 µm estimated diameter and spot classification with quality threshold > 27.4 was used to identify T2 target cells and source channel 4 (DAPI=CTV) with 8 µm estimated diameter and spot classification with quality threshold > 37.8, for REP T cells respectively. For detection of centrosome and perforin granules in REP T cells *surface*-tool was applied on source channel 4 (DAPI=CTV), 5 µm diameter cut-off of with 0.369 µm surface detail and > 2014 voxel cut-off. Fluorescent signal of source channel 1 (AF488=perforin) and source channel 2 (AF647=centrosome) outside of defined REP T cell surface was masked and positions of respective objects were identified with *spot*-tool: 0.8 µm estimated diameter and spot classification with quality threshold > 1365 for perforin and 1.84 µm estimated diameter and spot classification with quality threshold > 637 for centrosome. X, Y, Z values of each individual spot (cells, perforin granule and centrosome) were subjected to further analysis using script in R. For each spot we identified its parent T cell and for each T cell its nearest tumor cell using the RANN package. T cell-cancer cell interactions were considered if their centers were between 3 and 25 µm apart, which reduces distant non-interacting cells

and artefacts. Then the spot-to-cancer-cell distance was divided by the cell-to-cell distance to calculate the polarization ratio for each interaction pair. Median polarization ratios between conditions and field of views were compared in Graphpad Prism.

Immunoblot analysis

Activated memory T cells and PHA-blasts were lysed in RIPA buffer (ThermoFisher) containing protease- and phosphatase-inhibitors (Roche, #05 892 970 001 and #04 906 837 001), and protein concentrations determined with a BCA protein assay kit (ThermoFisher). Whole-cell lysates were denatured with 4x Laemmli buffer and separated by 4-20% SDS-PAGE and transferred to nitrocellulose or PVDF membranes (Biorad). Membranes were probed with the following primary antibodies: P-p44/42 MAPK (Erk1/2, Thr202/Tyr204, #D13.14.4E, Cell Signaling Technology), P-c-Jun (S73, #D47G9, Cell Signaling Technology), p44/42 MAPK (Erk1/2, #137F5, Cell Signaling Technology), c-Jun (#60A8, Cell Signaling Technology) and Actin (#8H10D10, Cell Signaling Technology). Blots were then stained with HRP-conjugated anti-rabbit or anti-mouse (both from Jackson ImmunoResearch Laboratories) secondary antibodies. SuperSignal West Pico PLUS Chemiluminescent Substrate (ThermoFisher) according to the manufacturer's instructions and ChemiDoc Imaging System (Biorad) were used for detection and FiJi software for quantification.

CRISPR-Cas9 editing of murine OT-I cells

Single cell suspensions were made from lymph nodes and spleens harvested from OT-I mice (male and female, 6-10 weeks, equal distribution of sex and age). 2×10^6 mL^{-1} OT-I lymphocytes were resuspended in medium containing 100 ng mL^{-1} $OVA_{257–264}$ peptide (Eurogentec) and 100 U mL^{-1} of IL-2 (Proleukin) and incubated for 48 h. OT-I cells were nucleofected with the P4 Primary Cell 4D-Nucleofector (Lonza) according to manufacturer's instructions using 4D-Nucleofector (Lonza). Briefly, 1×10^7 activated OT-I T cells were resuspended in 100 µl of Nucleofector Solution and combined with RNP solution. crRNAs were selected from predesigned CRISPR-Cas9 guide RNAs Tool from IDT. Product ID and sequences are listed in **Supplemental Table 1**. Per reaction, 900 pmol crRNA (IDT) or 900 pmol negative control crRNA #1 (IDT) were mixed with 900 pmol trRNA (IDT) in nuclease-free duplex buffer (IDT), annealed at 95°C for 5 min and added to 300 pmol µM Cas9 (QB3 MacroLab, UC Berkeley) followed by incubation at room temperature for at least 10 min. An appropriate nucleofector program was applied. OT-I lymphocytes were rested in Mouse T Cell Nucleofector Medium (Lonza) for 12 h and then washed and seeded in fresh medium at 10^6 mL^{-1} in round bottom 96 well-plates with 500 U mL^{-1} IL-2. Fresh IL-2 was added on a daily basis. Knock-out efficiency was validated by flow cytometry and purified by cell sorting.

CRISPR-Cas9 editing of human Jurkat T cells

Jurkat T cells were nucleofected using the AMAXA cell line V nucleofection kit (Lonza) according to manufacturer's instructions using 2b Nucleofector (Lonza). Briefly, 1×10^6 Jurkat T cells were resuspended in 100 µl of Nucleofector Solution and combined with RNP solution. crRNAs were selected from predesigned CRISPR-Cas9 guide RNAs Tool from IDT. Product ID and sequences are listed in **Supplemental Table 1**. crRNA (IDT) or negative control crRNA #1 (IDT) and trRNA (IDT) were mixed at a 1:1 ratio to a final concentration of 50 µM in nuclease-free duplex buffer (IDT), annealed at 95°C for 5 min and added to 40 µM Cas9 (QB3 MacroLab, UC Berkeley) followed by incubation at room temperature for at least 10 min. An appropriate nucleofector program

was applied. Knock-out efficiency was validated by flow cytometry and purified by cell sorting. Jurkat T cells were initially expanded for 1 week and then stored in liquid nitrogen until further use.

Plate reader-based Ca^{2+} flux assay

Murine OT-I CTLs were loaded with Calbryte 520 AM (AAT Bioquest) and Jurkat T cells were loaded with Fluo4 (ThermoFisher). Both calcium indicator dyes were used at a final concentration of 2 µM in Mg^{2+}-free self-made medium for 30 min at 37°C. Cells were washed twice and plated at 5×10^5 per well (OT-I CTLs) and 2×10^5 per well (Jurkat T cells) in a black flat bottom 96 well-plate (Greiner BIO-one) which had been precoated with Poly-D-Lysine (Gibco) in case of OT-I CTLs or collagen (ThermoFisher) for Jurkat T cell respectively. An additional incubation for 15 min at 37°C allowed cells to adhere and Fluo4 probe to de-esterified completely. OT-I CTLs were stimulated with 10 µM $OVA_{257–264}$ peptide (SIINFEKL, Eurogentec) and Jurkat T cells with 10 µg mL^{-1} anti-CD3. Fluorescence intensity over time was measure with a Tecan Spark M10 plate reader. The mean of fluorescent signal intensity was normalized to unstimulated baseline values.

Murine CTLs: differentiation and cultivation

Single cell suspensions were made from lymph nodes and spleens harvested from C57Bl/6 and LFA-1 KO mice (male and female, 6-10 weeks, equal distribution of sex and age). Naïve $CD8^+$ T cells were isolated using a magnetic bead-based negative selection kit following the manufacturer's recommendations (easySEP, Stem Cell Technologies). Naïve T cells (2×10^5 per well) were plated in presence of 5 µg anti-CD3 Ab (plate-bound) and 1µg anti-CD28 Ab (soluble; both from BioLegend) for 2 days in presence 100 U mL^{-1} of IL-2 (Proleukin). Cells were washed and seeded in fresh medium at 10^6 mL^{-1} in round bottom 96 well-plates with 500 U mL^{-1} IL-2. A cell density of 0.5–2 × 10^6 cells mL^{-1} was maintained for expansion and IL-2 was replaced on a daily basis. Functional read outs were carried out 7-19 days after initial activation and in the absence of IL-2.

Murine CTLs: *In vitro* activation and cytotoxicity assay

CTLs of WT or LFA-1 KO C57/Bl6 were activated for with plate-bound anti-CD3 Ab (145-2C11, BioLegend) at 0.05 µg mL^{-1} and soluble anti-CD28 Ab (37.51, BioLegend) at 1 µg mL^{-1} at 2×10^5 cells per well in a flat bottom 96 well plate. For stainings of surface activation markers, CTLs were activated for 8 h and for evaluation of 2-NBDG uptake, cells were activated for 6 h. For analysis of ERK1/2 phosphorylation, CTLs were stimulated with 5 µg mL^{-1} anti-CD3 Ab and 1 µg mL^{-1} anti-CD28 for 20 min prior to fixation and permeabilization. For cytotoxicity assays with WT or LFA-1 KO C57/Bl6 derived CTLs, cytotoxicity was evaluated with NucView 488 fluorogenic caspase-3 substrate (Biotium). Prior to co-incubation, CTLs were labeled with CellTrace Violet (CTV, Invitrogen) and EL4 target cells with CellTrace Far Red (CFTR, Invitrogen). Both cell population were then co-incubated at a CTL-target cell ratio of 3:1 (1.5×10^5 CTLs and 5×10^4 EL4 target cells) in presence of 10 µg mL^{-1} PHA for 4 h in a flat bottom 96 well plate. Caspase-3 substrate was added for final 45 min of incubation at final concentration of 1 µM. Cells were harvested, washed in FACS Buffer and fixed with PFA 2% for 15 min at RT prior to analysis by FACS. For cytotoxicity assays with OT-I derived CTLs were labeled with CTV, EL4 target cells were labeled with CFTR and pulsed with $OVA_{257–264}$ peptide (SIINFEKL, Eurogentec) or the altered peptide ligands R7 (SIIQFERL, Eurogentec), H7 (SIIQFEHL, Eurogentec) or G4 (SIIGFEKL, Eurogentec) at 1 µM for 30 min. EL4 target cells were washed 3 times prior to co-incubation at a CTL-target cell ratio of 3:1 (1.5×10^5 CTLs and 5×10^4 EL4 target cells)

in a flat bottom 96 well plate for 4h. Cytotoxicity was quantified with CellEvent Caspase-3/7 Green Detection Reagent (Invitrogen, ThermoFisher) as described above.

Immunofluorescent staining of immune synapse components in Jurkat T cells and PHA blasts

Cells were activated on species-appropriate anti-CD3-coated (1 µg mL^{-1} for human cells) glass-coverslips (ThermoFisher) for 2 min for phosphor-tyrosine analysist. Cell conjugates were fixed for 20 min at RT in 4% methanol-free PFA (Sigma Aldrich), permeabilized with 0.1% Triton-X100 (Sigma Aldrich) in PBS for 5 min and quenched with 50 mM Glycine (Sigma Aldrich) in PBS for 20 min. Fixation was followed by blocking in 1% bovine serum albumin (Sigma Aldrich) in PBS (blocking buffer) for 45 min at 4°C. Primary antibodies were then incubated in the same blocking buffer for 1 h at RT or overnight at 4°C. Samples were then washed four times with blocking buffer, followed by incubation with secondary antibodies in blocking buffer at room temperature for 1 h. Slides were then mounted with Prolong Diamond Antifade Mountant (ThermoFisher) and analyzed after 24 h of curing time at RT. The following reagents and antibodies were used for staining: phospho-tyrosine *P-Tyr-1000* (multiple monoclonal antibodies, unlabeled, Cell Signaling Technology), secondary goat anti-mouse (AF488, ThermoFisher), secondary goat anti-rabbit (AF647, ThermoFisher), Phalloidin-iFluor (AF555, Abcam) and DAPI (Sigma Aldrich).

Image analysis and quantitation of phospho-tyrosine signal intensity

For measurement of pan-phospho tyrosine signal intensity, FiJi software was used. Series of confocal Z-stacks were displayed as maximum intensity z-projections using *Z project*- tool. Individual cells were selected manually with *freehand selection*-tool according to cell boundaries indicated by phalloidin staining and fluorescent intensity was measured accordingly with *measure*-tool.

Magnesium-restricted diet

Magnesium-restricted diet and matching control diet, based on the purified ingredient rodent diet *AIN-76A*, were purchased at Research Diets Inc. (USA).

Sample collection of tissue interstitial fluid

Healthy C57BL/6NRj mice (male and female, 6-10 weeks, groups were sex and age adjusted) were kept on magnesium-restricted diet or corresponding control diet for 2 weeks. At day 14, liver, spleen and peripheral lymph nodes, muscle (musculus quadriceps femoris) and subcutaneous fat (flank) were aseptically removed. Organs were weighed, 50-300 ul PBS added (adjusted according to weight), and gently centrifuged at 300 x g for 8 min. Organ supernatants were recovered and stored at -80°C. Peritoneal fluid was harvested upon injection if 10 mL sterile PBS into peritoneal cavity; peritoneum was gently massaged and then aseptically opened by incision and lavage was collected. Tumor interstitial fluid of MC38-OVA tumors were collected 1 h after intratumoral injection of either 50 µl 3 mM $MgCl_2$ or 50 µl 3 mM NaCl. Tumors were aseptically excised, weighed and supernatant was recovered as described above. Tissue interstitial fluid of tumors from *in vivo* CAR T cell experiments were collected from UTD and saline control mice reaching ethically acceptable end point. Tumors were aseptically excised, weighed and supernatant was recovered as described above.

Magnesium measurements with ICP-MS

Samples of varying volumes (serum 5 µl; Muscle 10 µl; liver, lymph node, peritoneal fluid, subcutaneous fat and tumor 25 µl; spleen 50 µl) were added to 200 µl 67-69% HNO_3 (VWR Chemicals; NORMATOM® grade; LOT

1119100) and incubated at 95°C for 2 h. Digestates were filled up to 5 mL volume using ultra-pure H_2O (<18mΩ; Merckmillipore, 115333) and stored at 4°C. Samples were analyzed using triple quadrupole inductively coupled plasma mass spectrometry (qqq-ICP-MS) on an 8800 system (Agilent, Basel, Switzerland), using general-purpose operational settings. The system was operated in single quad mode using helium as collision gas and quantification done on $^{24}Mg^{+}$. To account for matrix effects, ^{103}Rh was used as the internal standard. Organ Mg^{2+} levels were normalized to tissue weight.

Blood count mice

Blood samples (70uL) were harvested in EDTA-coated tubes and diluted with 210uL NaCl 0.9%. Samples were run on the ADVIA 2120i hematology analyzer (Siemens) and analyzed by the multi-species program.

Polyclonal CD8 T cell activation *in vivo* with anti-CD3ε F(ab')2 fragment

Healthy C57BL/6NRj and LFA-1 KO mice (male and female, 6-10 weeks, groups were sex and age adjusted) were put on AIN76A magnesium-restricted or control diet for two weeks. On day 14, each mouse received 0.5 μg anti-CD3ε F(ab')2 fragment (BioXCell) per i.v. tail-vein injection. After 6 h, spleens were harvested splenocyte suspensions were analyzed by flow-cytometry.

***In vivo* killing assay**

C57BL/6NRj mice (male and female, 6-10 weeks, groups were sex and age adjusted) were immunized against OVA at day -19. In a first experiment, mice were immunized s.c. with 100 μg OVA protein (Invivogen) and 50 μg of CpG-B (Invivogen). In a second experiment, mice were immunized i.v. with 5×10^3 CFU LmOVA. On day 0, mice were put on magnesium-restricted or control diet for two weeks. On day 14, target splenocytes were harvested from naïve, syngeneic mice and either loaded with $OVA_{257–264}$ peptide (Eurogentec) or left untreated. Unloaded control splenocytes were labeled brightly with 2.50 μM CTV (CTV^{bright}) and $OVA_{257-264}$-loaded splenocytes dimly with 0.25 μM CTV (CTV^{dim}). Cells were then counted, mixed at 1:1 ratio in PBS, and $2\text{-}4\times10^6$ total target splenocytes were injected i.v. into pre-immunized and naive control mice. Additionally, 200 μl of 3 mM $MgCl_2$ and 200 μl of 3 mM NaCl were administered i.p., respectively. After 12 h, spleens were harvested and splenocyte suspensions were analyzed by flow-cytometry. Percentages of specific *in vivo* killing were calculated as [1-(% CTV^{dim} naive / % CTV^{bright} naive) / (% CTV^{dim} immunized / % CTV^{bright} immunized)]×100.

Listeria peritonitis model

C57BL/6NRj mice (male and female, 6-10 weeks, groups were sex and age adjusted) were immunized i.p. with 5×10^4 CFU Listeria monocytogenes expressing the OVA-peptide (*Listeria monocytogenes* expressing chicken Ovalbumin (AA134–387) originally gifted from Prof. Ed Palmer, University of Basel). After 19 days, mice were put on Mg^{2+}-restricted or matching control diet for 2 weeks. Mice were then re-infected i.p. with 5×10^5 CFU LmOVA. Bacterial inoculum was either spiked with 3 mM $MgCl_2$ or 3 mM NaCl diluted in 200 μl ddH_2O. Mice were sacrificed 12 h post infection and peritoneal fluid was harvested. Peritoneal fluid was harvested upon injection if 10 mL sterile PBS into peritoneal cavity; peritoneum was gently massaged and then aseptically opened by incision and lavage was collected. Peritoneal fluid was then plated on BHI agar-plates and colonies counted upon 24 h of incubation. Remaining peritoneal fluid were centrifuged at 300 x g for 10 min and supernatant recovered. Peritoneal fluid and sera were frozen at -80°C prior to further analysis. For flow cytometric analysis of memory $CD8^+$ T cell compartment, mice were scarified 20 h post infection, and peritoneal

fluid was harvested. MACS beads and LS columns (both Milteny Biotec) were used to enrich cell suspension for $CD8^+$ T cells. Cells were stained as described above and analyzed by FACS.

Cytometric bead array

Cytokine concentrations in cell culture supernatants, peritoneal fluids and serum were determined using the LegendPlex cytrometric bead array (CBA) Th1-Pannel (human and mouse, both from Biolegend) according to manufacturer's instructions.

Perforin quantification

Perforin concentrations in peritoneal fluids were determined using ProQuantumMouse Granzyme B Immunoassay Kit (Inivtrogen) according to manufacturer's instructions.

Murine MC38-OVA tumor model – set up

Unless stated otherwise, C57BL/6NCrl (female, 6 to 12 weeks old) were used for experiments. In assays with pre-immunized mice, mice were immunized 19 days before tumor implantation by subcutaneous injection of 100 µg of OVA protein (Invivogen) and 50 µg of CpG-B ODN 1826 (Eurogentec), resuspended in 100 µL of PBS. For tumor implantation, mice were inoculated subcutaneously onto the flanks with 0.5×10^6 MC38-OVA cells, resuspended in 100 µL of PBS. In bilateral tumor experiments, mice received 50 µL intra-tumoral injections of either 3 mM NaCl or 3 mM $MgCl_2$ (both diluted in ddH_2O). Injections of NaCl solution was applied in left flank tumor, whereas $MgCl_2$ solution was injected in contralateral tumor. I.t. injections were initiated once tumors were palpable, usually between day 5 and 10 after tumor injection. Injections were repeated every third day. Tumor size was quantified using a caliper and tumor volume was calculated using a rational ellipse formula ($\alpha^2 \times \beta \times \pi/6$, α being the shorter axis and β the longer axis). In all survival experiments, mice were withdrawn from the study after any tumor dimension had reached a length greater than 15 mm.

Murine MC38-OVA tumor model – with NSG mice

On day 0, 0.25×10^6 MC38-OVA cells were implanted subcutaneously onto the flank of NSG mice (female mice, 6-8 weeks old). On day 9, 2.5×10^6 LFA-$1^{-/-}$ or WT OT-I CTLs were transferred by tail-vein injection. CRISPR-Cas9 gene editing was carried out as described above. From day 9 onwards, intratumoral 3 mM NaCl or 3 mM $MgCl_2$ injections were initiated and repeated every second to third day.

Murine MC38-OVA tumor model – *in vivo* $CD8^+$ T cell depletion

For CD8 depletion experiment, mice were immunized with OVA, as described above, and inoculated with 0.5×10^6 MC38-OVA cells unilaterally on the flank. Intratumoral injections of either 3 mM NaCl or 3 mM $MgCl_2$ were initiated, and repeated every third day as tumors became palpable. CD8 T cells were depleted by administering anti-CD8a Ab (53-6.72, BioXCell) at 10mg kg^{-1} i.p. once per week.

Murine MC38-OVA tumor model – *in vivo* PD-1 blockade

For PD-1 blockade experiments, mice were immunized with OVA, as described above, and inoculated with 0.5×10^6 MC38-OVA cells unilaterally on the flank. As tumors became palpable - at day 5 - intratumoral injections of either 3 mM NaCl or 3 mM $MgCl_2$ were initiated, and repeated every third day for 8 cycles. Mice were additionally injected i.p. with isotype control (IgG2a) or anti-PD-1 Ab on day 9, 12, and 15 post-tumor implantations, at a dose of 200 µg per mouse diluted in 100 µL of pH-matched PBS (according to manufacturer's

recommendations). The antibodies used were: anti-PD-1 IgG2a Ab (clone RMP1-14) or IgG2a isotype control Ab (clone 2A3, both purchased from BioXCell).

Murine MC38-OVA tumor model – flow cytometry analysis of tumor-infiltrating immune cells

Tumor tissue was isolated from mice, weighed and minced using razor blades. Tissue was then digested using accutase (PAA), collagenase IV (Worthington), hyaluronidase (Sigma), and DNAse type IV (Sigma) for 60 min at 37 °C with constant shaking. The cell suspensions were filtered using a cell strainer (70 µm). Precision Counting beads (Biolegend) were added before staining to quantify the number of cells per gram of tumor. Single cell suspensions were blocked with rat anti-mouse FcγIII/II receptor (CD16/CD32) blocking antibodies ('Fc-block') and stained with live/dead cell-exclusion dye. Cells were then incubated with fluorophore-conjugated antibodies directed against cell surface antigens, washed and resuspended in FACS buffer (PBS+2% FBS). For intracellular/intranuclear antigens, cells stained with cell surface antibodies were fixed and permeabilized using Foxp3/transcription factor staining buffer (eBioscience) prior to incubation with antibodies directed against intracellular antigens.

Murine MC38-OVA tumor model – liposome and immunoliposome application

Liposomes were prepared using the thin film-hydration method (Huwyler et al., 1997). The lipid composition consisted of DSPC (1,2-distearoyl-sn-glycero-3-phosphocholine, Avanti Polar Lipids, Alabaster, AL), Cholesterol (3β-Hydroxy-5-cholestene, 5-Cholesten-3β-ol, Sigma Aldrich, Schaffhausen, Switzerland), DSPE-PEG2000 (1,2-distearoyl-sn-glycero-3-phosphoethanolamine-N-[methoxy(polyethylene glycol)-2000], Avanti Polar Lipids, Alabaster, AL), DSPE-PEG2000-Mal (1,2-distearoyl-sn-glycero-3-phosphoethanolamine-N-[maleimide(polyethyleneglycol)-2000], Avanti Polar Lipids, Alabaster, AL), and DiI (DiIC18(3), Sigma Aldrich, Schaffhausen, Switzerland) at a molar ratio of 69:27:2.5:0.5:1. Lipids were mixed in ethanol and a homogenous thin film was prepared using a Rotavapor A-134 (Büchi, Switzerland). Dried lipid films were stored under vacuum overnight and rehydrated with either 150 mM NaCl or 100 mM $MgCl_2$ at 70°C with constant stirring. Liposomes were extruded 13x through polycarbonate filters with an average pore diameter of 100 nm (Nucleopore, Whatman, North Bend, OH). Amicon Ultra-4 centrifugal filter units (MWCO 10 kDa) were used to concentrate the liposomes and to exchange the buffer to PBS pH 7.2. The liposomes were used within 4 h for anti-PD-1 conjugation via SATA-maleimide conjugation chemistry. Briefly, anti-PD-1 antibodies (clone RMP1-14, BioXCell) were functionalized with 10x molar excess of SATA (N-succinimidyl-S-acetylthioacetate, Fisher Scientific, Reinach, Switzerland) to introduce sulfhydryl groups according to the supplier's recommendations. The reactive sulfhydryl group on the antibody was then conjugated to the maleimide moieties on the liposome for 2 h at RT (ratio SH: maleimide = 1:4). Free maleimide groups were blocked by incubating with a 10x molar excess L-Cysteine for 30 min at RT. The anti-PD-1-conjugated liposomes were purified by gel filtration chromatography (Sepharose CL4B, elution buffer PBS pH 7.2). Fractions containing liposomes were pooled and concentrated using Amicon Ultra-4 centrifugal filter units (MWCO 10 kDa, Merck Millipore Ltd., Tullagreen, Carrigtwhohill, Co Cork IRL). Average size, size distribution and particle concentration were determined by dynamic light scattering using a Zetasizer Ultra (Malvern Panalytical, Volketswil, Switzerland). For intratumoral liposome injection, 4×10^{12} of $MgCl_2$-loaded liposomes and 2.6×10^{12} of NaCl-loaded liposomes were used. For immunoliposome

experiments, 100 µg of anti-PD-1 Ab coupled to $MgCl_2$- or NaCl-loaded liposomes were injected i.p. at indicated time points.

Anti-nuclear antibody (ANA) quantification

ANA concentrations were determined in murine serum 25 days after the start of i.t. NaCl or $MgCl_2$ injection as well in age- and sex-matched untreated control mice, using the mouse anti-nuclear antibody ELISA kit (Hoelzl Biotech) according to manufacturer's instructions.

Co-culture assay with *Blinatumomab*

Blinatumomab (Amgen) was derived from the leftover of infusions. Human PHA-blasts were incubated with Ramos or LCL target cells in flat bottom 96 well-plate at a 0.5:1 ratio (6.5×10^4 PHA blasts and 1.3×10^5 target cells) at indicated Blinatumomab concentrations. In order to distinguish the different cell populations, PHA-blasts were labeled with CTV and target cells with CFTR Invitrogen. Anti-CD18 antibodies, CBR-LFA-1/2 (unlabeled, Ultra-LEAF, BioLegend), TS1/18 (unlabeled, Ultra-LEAF, BioLegend) as well Mouse IgG1 κ Isotype control (unlabeled, Ultra-LEAF, BioLegend) were used at a final concentration of 10 µg mL^{-1}. For all co-incubation experiments, cells were allowed to sediment without centrifugation. For analysis of protein phosphorylation, co-incubation was terminated after 60 min with fixation of of 4% PFA and methanol as described in more detail above. For assessing LFA-1 headpiece opening, m24 antibody was directly added to the cell culture medium and stained for 30 min on ice before washing and subsequent fixation with 2% PFA. Cytotoxicity was quantified after 3.5 h with CellEvent Caspase-3/7 Green Detection Reagent (Invitrogen, ThermoFisher) as described above. Caspase substrate was added for final 45 min of incubation at final concentration of 2 µM. Cells were harvested, washed in FACS Buffer and fixed with PFA 2% for 15 min at RT prior to analysis by FACS.

Production of anti-CD19 CAR T cells for *in vitro* experiments

24 h before transfection, HEK-293T cells were seeded (3.8×10^6 cells 10 mL^{-1} media). All plasmid DNA was purified using the Endotoxin-free Plasmid Maxiprep Kit (Sigma). HEK-293T cells were transfected with 1.3 pmol psPAX2 (lentiviral packaging plasmid) and 0.72 pmol pMD2G (VSV-G envelope expressing plasmid) and 1.64 pmol of pCAR-CD19CAR-p2a-EGFP (Creative Biogene) using Lipofectamine 2000 (Invitrogen) and Optimem medium (Invitrogen, Life Technologies). The viral supernatant was collected 48 h after transduction. Viral particles were concentrated using PEG precipitation and stored at -80°C. Blood samples (Blood donor center, University Hospital Basel) were obtained from healthy donors after written informed consent. PBMCs were isolated by standard density-gradient centrifugation protocols (Lymphoprep; Fresenius Kabi). $CD4^+$ and $CD8^+$ T cells were positively selected using magnetic $CD4^+$ and $CD8^+$ beads (Miltenyi Biotec). Purified $CD4^+$ and $CD8^+$ T cells were cultured in R10AB. $CD4^+$ and $CD8^+$ T cells were plated into a 24-well cell culture plate and stimulated with anti-CD3 and anti-CD28 mAb-coated beads (Miltenyj, T cell activation & expansion kit) in a ratio of 1:1 in medium containing IL-2 (150 U mL^{-1}). T cells were transduced with lentiviral particles at 18-22 h after activation in media containing Polybrene (6 µg mL^{-1}, Millipore). Every second day medium was replaced with fresh IL-2 (150 U mL^{-1}). Five days after transduction GFP^+ cells were sorted enrich CD19-CAR^+ cells and magnetic beads were removed from non-transduced cells. Cells were further expanded for 3 days in medium containing IL-2 (150 U mL^{-1}) before the target cell killing assay.

Cytotoxicity assay with anti-CD19 CAR T cells

$CD8^+$ anti-CD19 CAR T-cells were incubated with Ramos target cells at a 0.1-0.33:1 ratio ($0.5\text{-}1.5\times10^4$ CAR T cells and 5×10^4 Ramos Target cells). Ramos cells had been labeled with CFTR prior to co-incubation. Cells were allowed to sediment without centrifugation in flat bottom 96 well-plate and incubated for 3 h. Cytotoxicity was quantified by flow cytometry using BioTracker NucView 405 Blue Caspase-3 Dye (Sigma-Aldrich).

Primary human T cell transduction for anti-CD19 CAR T cell generation used in *in vivo* experiments

To generate human CD8+ CAR-T cells, we isolated $CD8^+$ T cells from heathy donor PBMCs using the CD8 human microbead MACS kit according to manufacturer's instruction. Cells were then cultured in RPMI-1640 (Sigma) with 10% heat inactivated human male AB^+ serum with 1mM Sodium Pyruvate (Sigma), 2mM Glutamine (contained in RPMI formulation), 10 mM HEPES (Gibco), 5mM beta-mercapto-Ethanol (Gibco), 1% PenicilinStreptomycin (Sigma). Cells were stimulated on the same day with 1:1 ratio of CD3/CD28 beads (Human T cell Activation and Expansion kit, Miltenyi) and 150 U mL^{-1} rh-IL-2 (Proleukin). The next day, cells were collected into a falcon tube and 4 μg mL^{-1} Polybrene (Sigma) was added together with VSV-g pseudotyped lentivirus encoding an anti-human-CD19-FMC63vH chimeric antigen receptor with a CD28 transmembrane domain and a CD28 and CD3ζ signaling domain with a c-terminal T2A self-cleaving copGFP protein (anti-CD19-CD28z-T2A-copGFP). The cell and lentiviral mixture was centrifuged for 90 min at 1000 g (spinfection) and the resuspended and plated for 24 h at 37°C. Then cells were expanded 1:2 every 2 days for 2 iterations with fresh medium and 50 U/mL rh-IL-2. GFP^+ $CD8^+$ (CD8-APC SK1 clone, Biolegend) live (DAPI, Sigma) cells were then sorted using a BD FACS Melody, washed in medium and the plated at 1.5 Mio mL^{-1} in fresh medium and 50 U mL^{-1} rh-IL-2 for another 24h. Cells were then counted, washed by centrifugation at 500g 3 min in PBS and transferred in PBS intravenously to female NSG mice (6-8 weeks old) subcutaneously injected 5 days before with 0.5 Mio Raji (ATCC) in 50% Matrigel (Corning, standard formulation). Intratumoral injections of either 3 mM NaCl or 3 mM $MgCl_2$ were initiated 7 days after tumor implantation, and repeated every second to third day.

Recombinant lentivirus production for anti-PSMA CAR T cells

High-titer replication-defective lentivirus was produced and concentrated by ultracentrifugation for primary T cell transduction. Briefly, 24 h before transfection, HEK-293 cells were seeded at 10×10^6 in 30 mL of medium in a T-150 tissue culture flask. All plasmid DNA was purified using the Endo-free Maxiprep kit (Invitrogen, Life Technologies). HEK-293T cells were transfected with 7 μg pVSV-G (VSV glycoprotein expression plasmid), 18 μg of R874 (Rev and Gag/Pol expression plasmid) and 15 μg of pELNS transgene plasmid, using a mix of Turbofect (ThermoFisher) and Optimem medium (Invitrogen, Life Technologies, 180 μl of Turbofect for 3 mL of Optimem). The viral supernatant was collected 48 h after transfection. Viral particles were concentrated by ultracentrifugation for 2 h at 24,000 x g and resuspended in 400 μl medium, followed by immediate snap freezing on dry ice.

Primary human T cell transduction for anti-PSMA CAR T cell generation

Primary human T cells were isolated from the peripheral blood mononuclear cells of healthy donors (HDs; prepared as buffycoats or apheresis filters). All blood samples were collected with informed consent of the healthy donors, and genetically engineered with ethics approval from the Canton of Vaud, Switzerland. PBMC were obtained via Lymphoprep (Axonlab) separation solution, using a standard protocol of centrifugation. CD4 and $CD8^+$ T cells were isolated using a magnetic bead-based negative selection kit following the manufacturer's

recommendations (easySEP, Stem Cell technology). Purified CD4 and $CD8^+$ T cells were cultured at a 1:1 ratio and stimulated with anti-CD3 and anti-CD28 Ab coated beads (Invitrogen, Life Technologies) at a ratio of 1:2 T cells to beads. T cells were transduced with lentivirus particles at 18-22 h after activation. Human recombinant IL-2 (h-IL-2; Glaxo) was replenished every other day for a concentration of 50 IU mL^{-1} until 5 days after stimulation (day + 5). At day + 5, magnetic beads were removed, and h-IL-7 and h-IL-15 (Miltenyi Biotec) were added to the cultures at 10 ng mL^{-1} replacing h-IL-2. A cell density of 0.5-1 × 10^6 cells mL^{-1} was maintained for expansion. Rested engineered T cells were adjusted for equivalent transgene expression before all functional assays.

Cytotoxicity assay with anti-PSMA CAR T cells

Cytotoxicity assays were performed using the IncuCyte Instrument (Essen Bioscience). Briefly, 1.25×10^4 PC3-PIP target cells were seeded in flat bottom 96-well plates (Costar, Vitaris). Four hours later, rested T cells (no cytokine addition for 48 h) were washed and seeded at 2.5 × 10^4 per well, at a 2:1 effector to target ratio in self-made medium supplemented with 10% dFCS and ±0.6 mM $MgCl_2$. No exogenous cytokines were added during the co-culture period. IncuCyte Caspase-3/7 (Essen Bioscience) was added at a final concentration of 5 µM in a total volume of 200 µl. Internal experimental negative controls were included in all assays, including co-incubation of untransduced (UTD)-T cells and tumor cells in the presence of IncuCyte Caspase-3/7 reagent to monitor spontaneous cell death over time. As a positive control, tumor cells alone were treated with 1% triton solution to evaluate maximal killing in the assay. Images of total green area per well were collected every 2 h of the co-culture. The total green area per well was obtained by using the same analysis protocol on the IncuCyte ZOOM software provided by Essen Bioscience. Cytotoxicity is reported as total area under the curve of the fluorescence driven by incorporation of cytotoxic green reagent in dead target cells (green area per μm^2). All data were normalized by subtracting the background fluorescence observed at time zero (before any cell killing by CAR T cells) from all further time points.

Cytokine release assay of anti-PSMA CAR T cells

Cytokine release assays were performed by co-culture of 5×10^4 T cells with 5×10^4 target cells per well in 96-well round-bottom plates, in duplicate, in a final volume of 200 µl of self-made medium supplemented with 10% dFCS and 0.6 mM $MgCl_2$ or without Mg^{2+} supplementation. After 24 h, the co-culture supernatants were collected and tested for the presence of IFN-γ by commercial enzyme-linked immunosorbent assay kits according to the manufacturer's protocol (BioLegend).

Anti-PSMA CAR T cell *in vivo* experiment

Male NSG mice of 10-12 weeks were put on Mg^{2+}-restricted or matching control diet 5 days prior to tumor injection and kept on respective diet throughout the experiment. 5×10^6 PC3-PIP tumor cells were injected subcutaneously. After 5 days, intravenous injection of saline solution or 2×10^6 T cells (UTD or CAR T cells) were adoptively transferred intravenously. Tumor volume was monitored twice per week. The animals were monitored daily and the tumors were calipered every other day. Tumor volumes were calculated using the formula V=1/2(length × $width^2$), where length is the greatest longitudinal diameter and width is the greatest transverse diameter determined via caliper measurement.

Quantification and statistical analysis

Statistical significance was tested for using Prism 9.0 (GraphPad Software, USA). P values of less than 0.05 were considered statistically significant.

Graphical Illustrations

All graphical illustrations were created with BioRender.com.

SUPPLEMENTARY FIGURES

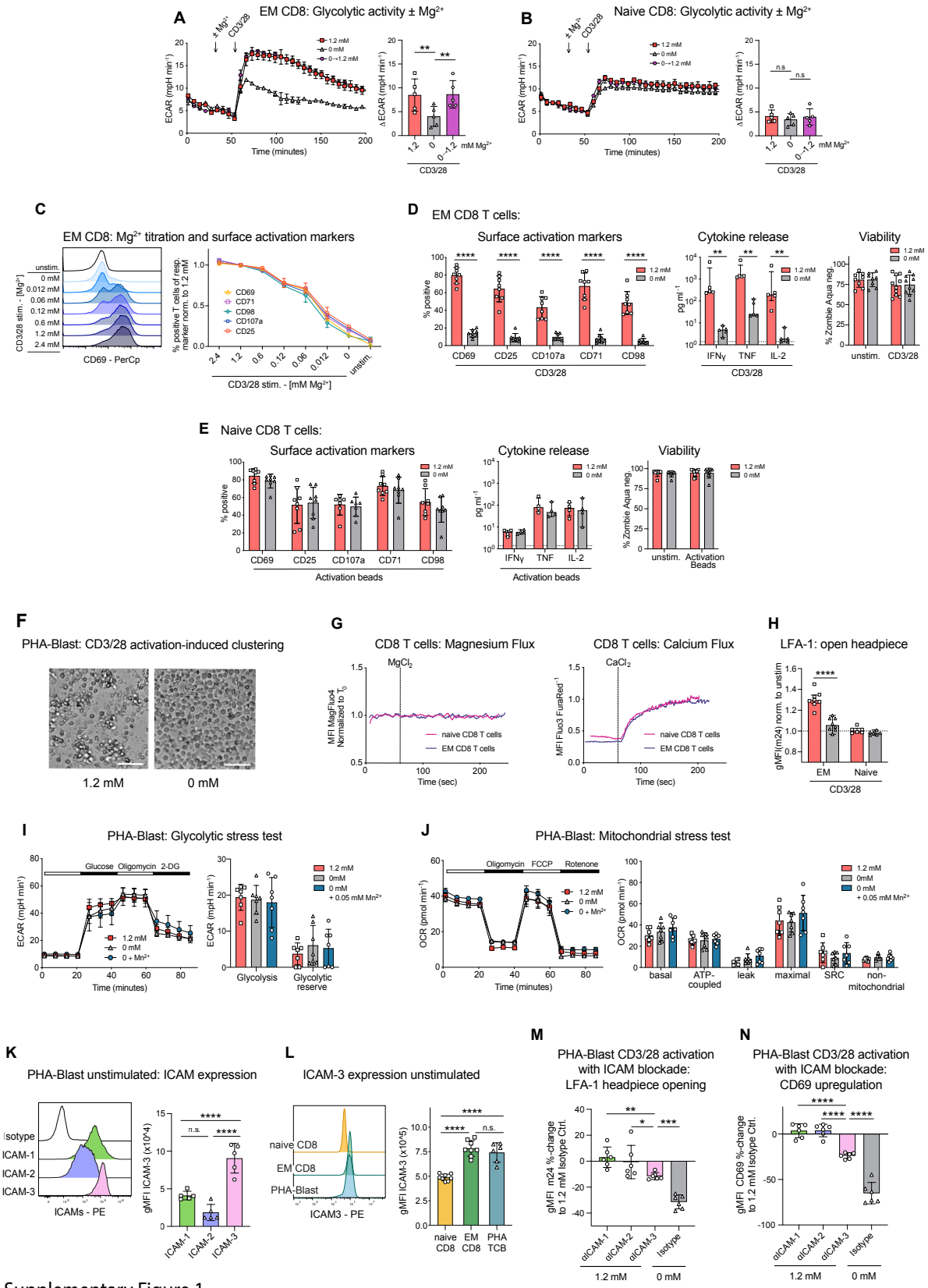

Supplementary Figure 1

Figure S1. Extracellular Mg^{2+} promotes activation of memory T cells, related to Figure 1

(A and B) Glycolytic activity of human $CD8^+$ T cell subsets upon injection of anti-CD3 and anti-CD28 antibody in medium containing 1.2 mM Mg^{2+}, 0 mM Mg^{2+}, or medium which was reconstituted from 0 mM to 1.2 mM Mg^{2+} just prior to activation (0 / 1.2 mM Mg^{2+}). (A) Results for human effector memory (EM), and (B) for human naive $CD8^+$ T cells. Traces of a representative metabolic flux experiment (*left panels*), and pooled data of n = 5 independent experiments (*right panels*). (C) Flow cytometric analysis of the indicated surface activation markers on human EM $CD8^+$ T cells activated at indicated Mg^{2+} concentrations for 24 h. Representative flow histogram of CD69 expression (*left panel*), and pooled data from two healthy donors (*right panel*).

(D) Surface activation markers on EM CD8+ T cells after activation for 24 h. Pooled data from n = 5 independent experiments (*left panel*). Abundance of inflammatory cytokines in corresponding cell culture supernatants. The dashed line indicates detection limit (*middle panel*). Viability of EM $CD8^+$ T cells (*right panel*). (E) Surface marker expression on activated naive $CD8^+$ T cells after 24 h. Pooled data from n = 4 independent experiments (*left panel*). Abundance of inflammatory cytokines in corresponding cell culture supernatants. The dashed line indicates detection limit (*middle panel*). Viability of naive $CD8^+$ T cells (*right panel*).

(F) Representative brightfield images of activation-induced clustering of PHA blasts after 6 h. Scale bars indicate 50 mm.

(G) Flow cytometric analysis of Mg^{2+} influx (*left panel*) and Ca^{2+} influx (*right panel*) into naive and EM $CD8^+$ T cells, using fluorescent probes.

(H) Flow cytometry-based assessment of TCR activation-induced LFA-1 headpiece opening (as detected by mAb m24 binding) on human EM and naive $CD8^+$ T cells. Pooled data of n = 4 independent experiments using cells from 1 to 2 individual healthy donors

(I) Assessment of glycolysis and glycolytic reserve of human PHA blasts. One representative experiment (*left panel*) and pooled data from two independent experiments (*right panel*) are shown. (J) Mitochondrial perturbation assay of human PHA blasts. *Left panel* depicting a representative experiment, summary bar graph in the *right panel*, representing calculated basal respiration, ATP-coupled respiration, leak respiration, maximal respiration, and spare respiratory capacity (SRC), as well nonmitochondrial respiration (pooled from two independent experiments).

(K) Representative ICAM1-3 expression profile on PHA blasts as determined by flow cytometry (*left panel*) and summary bar graph (*right panel*).

(L) Representative ICAM-3 expression profile on human naive and EM $CD8^+$ T cells as well human PHA blasts, as determined by flow cytometry (*left panel*) and summary bar graph (*right panel*).

(M and N) Flow cytometric assessment of LFA-1 headpiece opening (M), and expression of CD69 (N) on PHA blasts activated in presence of ICAM blocking mAb, as indicated (not normalized for ICAM expression). Each symbol represents an individual healthy donor. Data are presented as mean ± SD in (H, M, and N), in the *right panel* of (A–C and I–L) and the *left* as well as *right panels* of (D and E) or median ± IQR *middle panel* of (D and E). In representative metabolic flux analyses symbols indicate mean ± SEM in the *left panel* of (A, B, I, and J). Traces of Mg^{2+} or Ca^{2+} flux experiments indicate mean of respective fluorescent intensity (G). Statistical significance was assessed by repeated-measures one-way ANOVA with Sidak's multiple comparison test *right panel* of (A, B, and I–L) as well as (M and N), unpaired two-tailed Student's t test with Holm-Sidak corrected multiple comparison test *left panel* and *right panel* of (D and E) and (H), and Mann-Whitney test *middle panel* of (D and E). * $p < 0.05$, ** $p < 0.01$,*** $p < 0.001$, **** $p < 0.0001$, n.s. = nonsignificant.

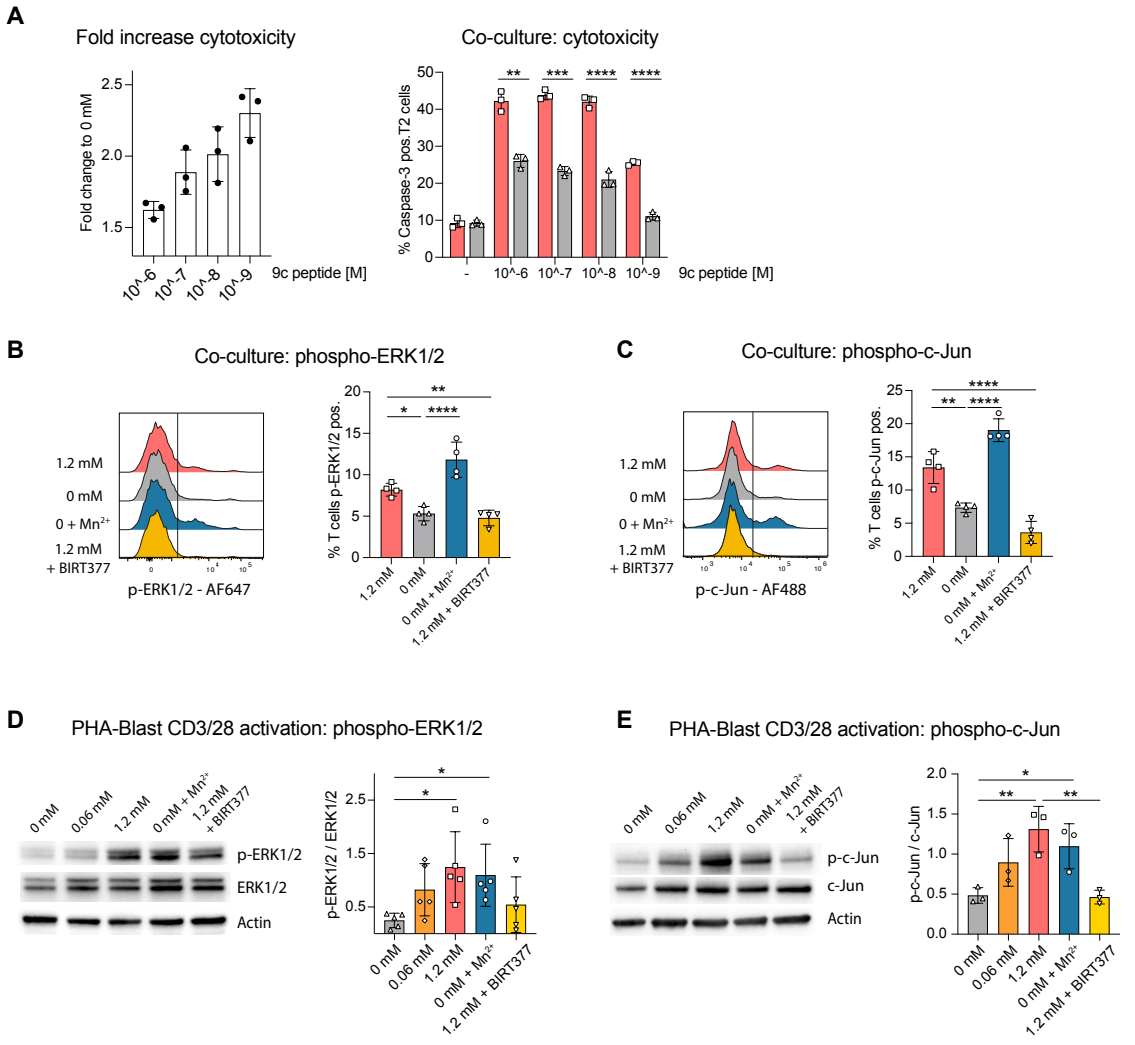

Supplementary Figure 2

Figure S2. The Mg^{2+}-LFA-1 axis regulates cytotoxicity and phosphorylation of ERK1/2 and c-Jun, related to Figure 2

(A) Caspase-3 activity in T2 target cells after co-incubation with NY-ESO-1-specific REP T cells. *Left panel* depicts fold increase of caspase-3 positive T2 cells in 1.2 mM Mg^{2+}, the *right panel* illustrates the corresponding percentage of caspase-3 positive T2 cells.

(B and C) Representative histograms (*left panels*), quantified results of n = 1 healthy donor with 4 technical replicates (*right panels*). Phosphorylation of ERK1/2 (B), and c-Jun (C) in human REP T cells after incubating with cognate-peptide pulsed T2 target cells

(D and E) Immunoblot analyses of ERK1/2 phosphorylation (D) and c-Jun phosphorylation (E) in activated human PHA blasts. *Left panel* depicting immunoblots that were probed for the indicated phosphorylated and total proteins, as well as actin. *Right panel* depicting summarized quantitation with 3–5 healthy donors. (F) Representative immunoblots of primary human EM $CD8^+$ T cells. Immunoblots were probed for phosphorylated ERK1/2 and c-Jun, as well actin.

Each symbol represents an individual healthy donor. Bars indicate mean ± SD (A–E), and statistical significance was assessed with unpaired two-tailed Student's t test with Holm-Sidak corrected multiple comparison test *right panel* of (A), one-way ANOVA with Sidak's multiple comparison test *right panel* of (B–E). *$p < 0.05$, **$p < 0.01$, ***$p < 0.001$, ****$p < 0.0001$.

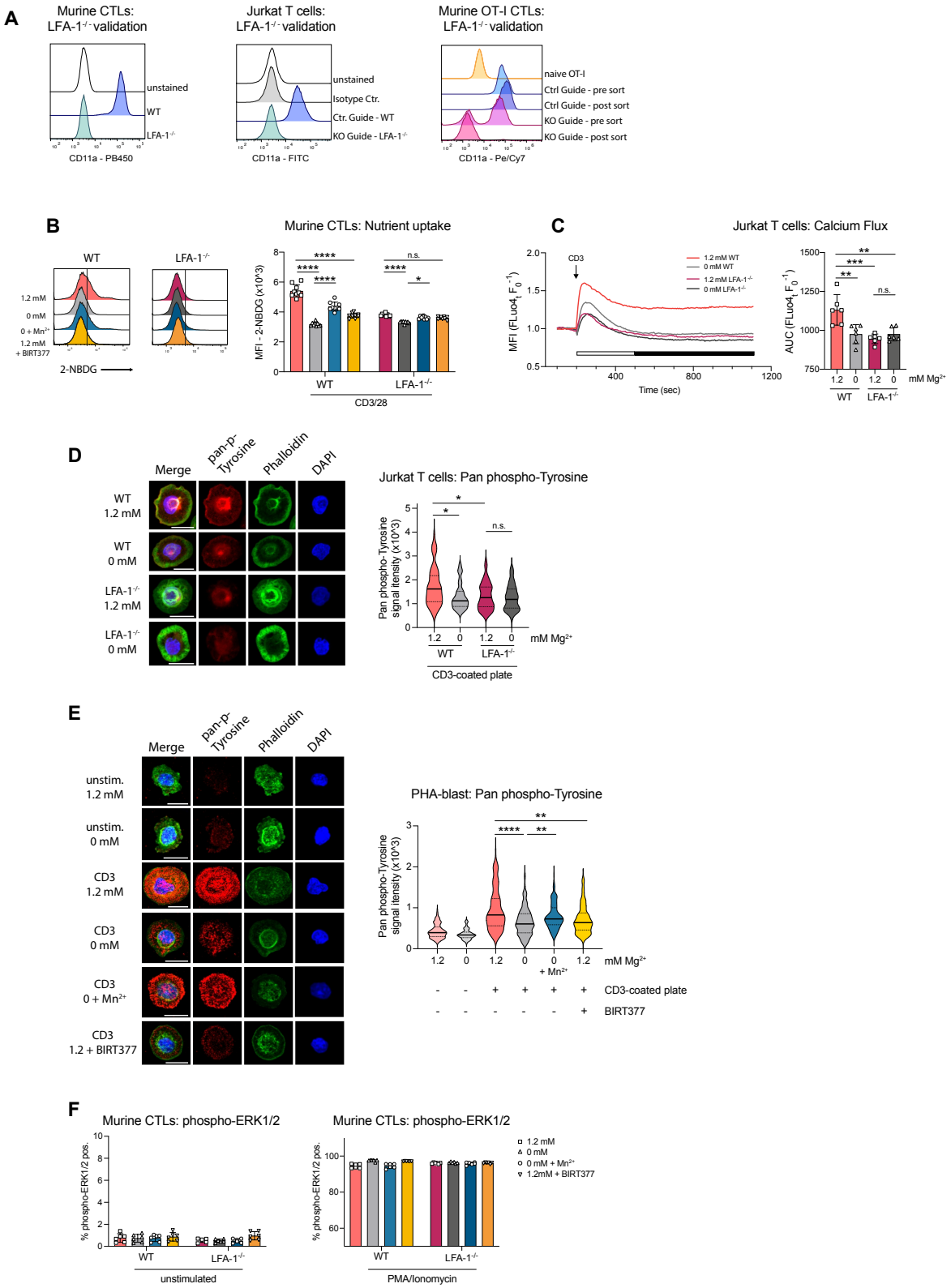

Supplementary Figure 3

Figure S3. Extracellular Mg^{2+} regulates Ca^{2+} flux and immune synapse formation through LFA-1, related to Figure 3

(A) Representative histogram comparing CD11a surface expression on CTLs derived from murine WT and LFA-$1^{-/-}$ CTLs (*left panel*), WT (treated with negative control guide RNA) and LFA-$1^{-/-}$ Jurkat T cells (*middle panel*), as well naive OT-I cells and CRISPR-Cas9-edited OT-I CTLs before and after purification by cell sorting (*right panel*).

(B) Glucose uptake by activated murine WT and LFA-$1^{-/-}$ CTLs. Representative flow histogram profile (*left panel*) and summary graph from n = 3 mice with three technical replicates each (*right panel*).

(C) TCR stimulation induced calcium flux in WT and LFA-$1^{-/-}$ Jurkat T cells. Representative trace (*left panel*), and quantification of area under the curve (AUC) of three independent experiments in duplicates (*right panel*).

(D) *Left panel*, representative immunofluorescence images of WT and LFA-$1^{-/-}$ Jurkat T cells stimulated on anti-CD3 Ab-coated coverslip. Images are displayed as confocal projections of 3D stacks. Scale bars indicate 10 mm. *Right panel*, quantitative analysis of fluorescent signal intensity (n = 62–71 cells/condition, pooled from two different fields of view).

(E) *Left panel*, representative immunofluorescent images of PHA blasts stimulated on ±anti-CD3-coated coverslip. Cells were stained for pan-tyrosine phosphorylation, actin, and nuclei. Images are displayed as confocal projections of 3D stacks. Scale bars indicate 10 mm. Right panel, quantitative analysis of fluorescent signal intensity (n = 91–146 cells/condition, pooled from 2 to 4 different field of views).

(F) Flow cytometric analysis of ERK1/2 phosphorylation in murine WT and LFA-$1^{-/-}$ CTLs. Left panel shows unstimulated baseline ERK1/2 phosphorylation, and *right panel* depicts phosphorylation status upon PMA and ionomycin treatment. Quantified results of n = 3 mice in duplicates each. Data are presented as mean ± SD right panel of (B and C) and *both panels* (F), median ± IQR *right panel* of (D and E). Traces of representative calcium flux, left panel of (C), indicate mean of duplicate wells. Statistical significance was assessed by one-way ANOVA with Sidak's multiple comparison test *right panel* of (B and C) and *both panels* (F), Kruskal-Wallis test with Dunn's multiple comparisons test was applied for (D and E). *p < 0.05, **p <0.01, ***p <0.001, ****p < 0.0001, n.s., nonsignificant.

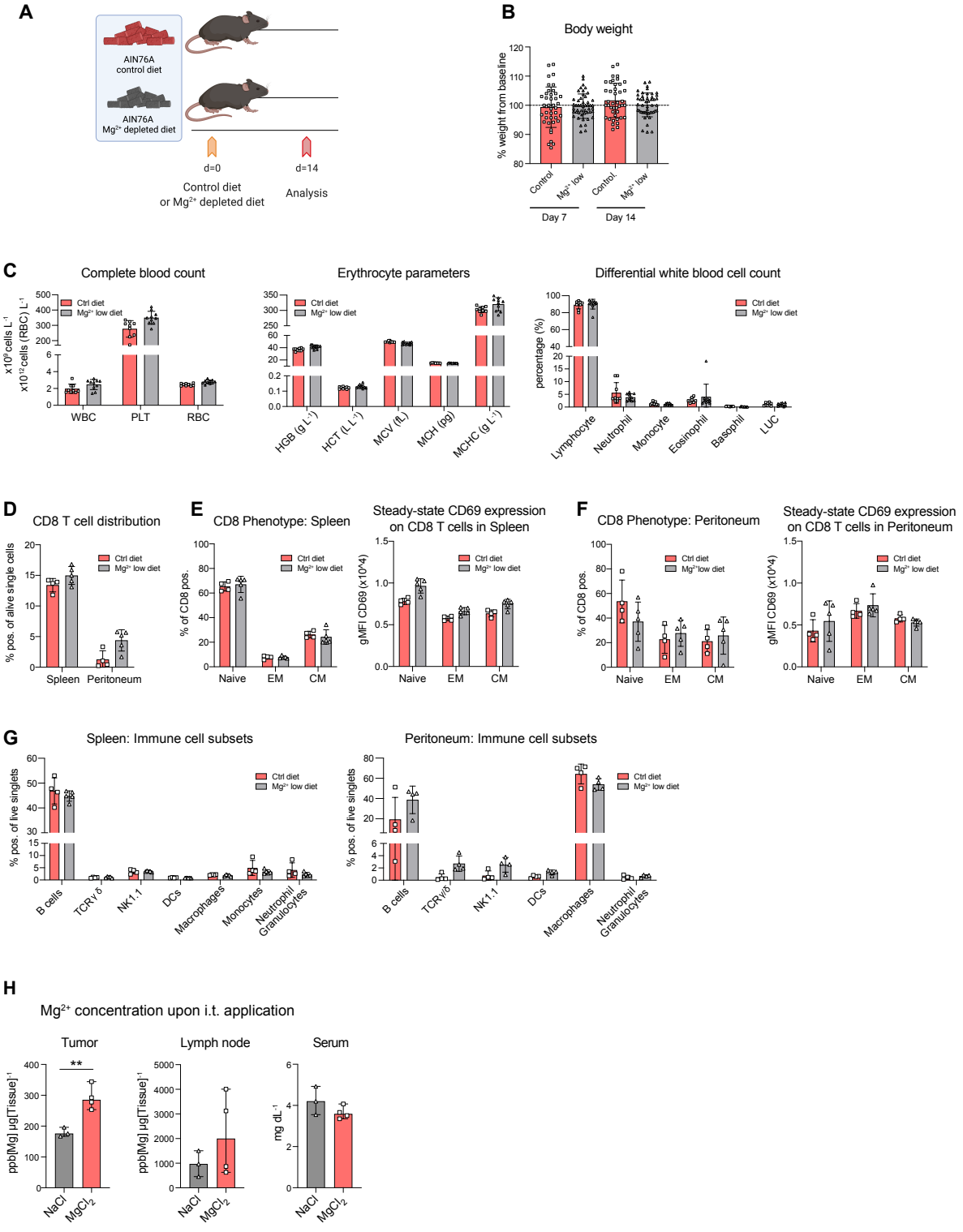

Supplementary Figure 4

Figure S4. Immune phenotype of short-term organismal Mg^{2+} depletion in uninfected mice, related to Figure 4

(A) Schematic of experimental design.

(B–G) Heathy Bl/6 mice were placed on Mg^{2+} low and matching control diet for 2 weeks without further intervention.

(B) Percentage weight change compared with individual baseline value after 7 and 14 days. Pooled data from n = 5 independent experiments.

(C) *Left panel*, complete blood count representing absolute numbers of white blood cells (WBC), platelets (PLT), and red blood cells (RBCs). *Middle panel*, quantitation of red blood cell parameters: Hemoglobin (HGB), hematocrit (HCT), mean cell volume (MCV), mean cell hemoglobin (MCH), mean cell hemoglobin concentration (MCHC). *Right panel*, white blood cell subsets in peripheral blood are shown as percentage distribution. Pooled data from n = 2 independent experiments.

(D) Abundance of $CD8^+$ T cells in spleen and peritoneal cavity.

(E and F) Flow cytometric characterization of $CD8^+$ T cell subsets: naive, effector memory (EM) and central-memory (CM). Composition of $CD8^+$ T cell subsets in spleen (E, *left panel*) and peritoneal cavity (F, *left panel*). Quantification of CD69 expression on $CD8^+$ T cell subsets in spleen (E, *right panel*) and peritoneal cavity (F, *right panel*).

(G) Analysis of relative abundance of immune cell subpopulations in spleen (*left panel*) and peritoneal cavity (*right panel*).

(H) Magnesium levels in interstitial fluid of tumor (*left panel*), draining lymph node (*middle panel*) and serum (*right panel*) after intratumoral application of NaCl or $MgCl_2$. Each symbol represents an individual mouse. Data is presented as mean ± SD (B–G) and median ± 95% Cl (H). Statistical significance was assessed with unpaired two-tailed Student's t test (H). ** $p < 0.01$.

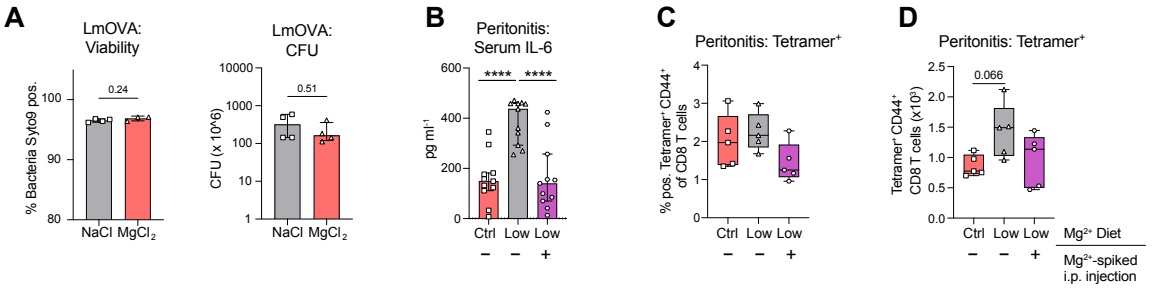

Supplementary Figure 5

Figure S5. Dietary restriction of Mg^{2+} impairs memory $CD8^+$ T cell-mediated control of bacterial infection, related to Figure 5

(A) Viability of LmOVA in 3 mM NaCl or 3 mM $MgCl_2$ inoculum solution used for *in vivo* infection studies (*left panel*), and number of colony forming units (CFUs) after plating the respective bacterial solution on BHI plates (*right panel*). (B–D) LmOVA infection experiments. Each symbol represents an individual mouse. (B) Bar graph representing serum IL-6 concentrations. Relative abundance (C) and absolute cell numbers (D) of OVA-tetramer specific memory CD8+ T cells retrieved from the peritoneal cavity. Data are presented as mean ± SD left panel of (A). Median ± IQR is shown in right panel of (A) and (B–D). Statistical significance was assessed with unpaired two-tailed Student's t test *left panel* of (A), Mann-Whitney test *right panel* of (A) and one-way ANOVA with Sidak corrected multiple comparison test (B–D). **** $p < 0.0001$.

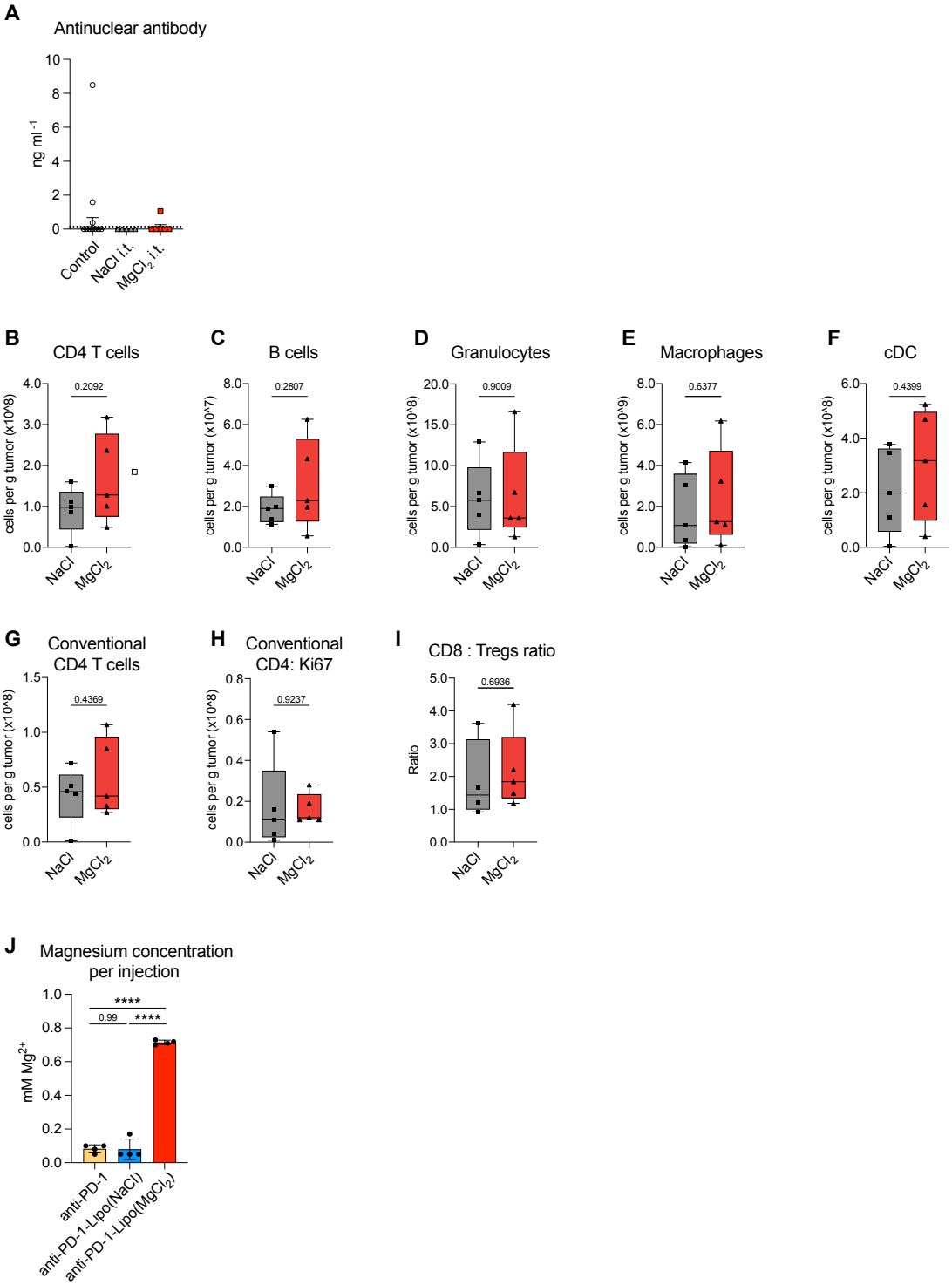

Supplementary Figure 6

Figure S6. Effect of Mg^{2+} on ANA production and intratumoral immune phenotype, related to Figure 6

(A) Concentration of anti-nuclear antibodies (ANAs). Each symbol represents an individual mouse, n = 5–10 per group.

(B–I) Cell number of tumor-infiltrating $CD4^+$ T cells (B), B cells (C), granulocytes (D), macrophages (E), conventional dendritic cells (F), conventional $CD4^+$ T cells (G), $Ki67^+$ conventional $CD4^+$ T cells (H), as well the CD8:T_{Reg} ratio (I). Each symbol represents an individual mouse, n = 5 per group (B–I).

(J) Magnesium concentration per injection of respective treatment modality. Data are presented as median ± IQR (A–I) and mean ± SD (J); dashed line in (A) indicates detection limit. Statistical significance was assessed by unpaired two-tailed Student's t test (B–I) and one-way ANOVA with Sidak corrected multiple comparison test (J). **** $p < 0.0001$.

Figure S7. Association of Mg^{2+} abundance and efficacy of immune therapeutic modalities in vitro and in vivo, related to Figure 7

(A and B) Flow cytometry-based assessment of activation-induced LFA-1 headpiece opening on PHA blasts (A), as well FAK phosphorylation in PHA blasts (B), after co-culture with Ramos cells at a Blinatumomab concentration of 300 pg mL^{1} (n = 5 healthy donors)

(C) Activation-induced glycolytic activity of human CAR T cells. Representative experiment (*left panel*), quantification of summarized data (*right panel*) from n = 3 healthy donors

(D) *Left panel*, representative histograms of surface activation markers on CAR T cells. *Right panel* shows quantitation of respective staining from n = 3 healthy donors

(E and F) Magnesium abundance determined by ICP-MS in serum from mice in CAR T cell tumor-rejection experiment after 14 days on respective diet (E). Magnesium abundance in interstitial fluid of tumors from UTD and saline control mice reaching ethically acceptable end point (F)

(G) Diet consumption of mice in CAR T cell tumor-rejection experiment

(H) Body weight after 24 days of respective diet relative to individual starting value

(E–H) Each symbol represents one mouse

(I) Study diagram and patient exclusion criteria

(J) Table summarizing baseline characteristics. DLBCL, diffuse large B cell lymphoma; PMCL, primary mediastinal large B cell lymphoma; TFL, transformed follicular lymphoma.

(K) Comparison of patients stratified according to mean serum magnesium levels between day 5 and day +3 of treatment in normal Mg^{2+} group (>1.7 mg dl^{1}) and low Mg^{2+} group (<1.7 mg dl^{1}), n = 5 measurements per patient. Each symbol represents individual patient

(L) Progression-free survival

(M) Study diagram and patient exclusion criteria

(N) Table summarizing baseline characteristics

(O and P) Comparison of radiographic response (O), and event-free survival (P) in normoversus hypomagnesemic patients with NSCLC. Data are presented as mean ± SD in (A, B, E, G, H, and K) as well *right panels* of (C and D), median ± IQR (F) and in representative metabolic flux analyses symbols indicate mean ± SEM in the *left panel* of (C). Statistical significance was determined with unpaired Student's t test (A, B, E–G, and K), one-way ANOVA with Sidak's multiple comparison test (C), unpaired two-tailed Student's t test with Holm-Sidak corrected multiple comparison test (D and H) and log-rank Mantel-Cox test (L and P). * $p < 0.05$, ** $p < 0.01$,***$p < 0.001$, **** $p < 0.0001$.